

 Open access • Journal Article • DOI:10.1088/1361-6633/AA8372

## Emerging optical properties from the combination of simple optical effects

— [Source link](#) 

Grant T. England, Joanna Aizenberg, Joanna Aizenberg

**Institutions:** Harvard University, Wyss Institute for Biologically Inspired Engineering

**Published on:** 01 Jan 2018 - Reports on Progress in Physics (IOP Publishing)

Related papers:

- [Bioinspired Photonic Pigments from Colloidal Self-Assembly.](#)
- [Bioinspired structural materials](#)
- [N-dimensional optics with natural materials](#)
- [Bioinspired Hierarchical Composites](#)
- [A colloidoscope of colloid-based porous materials and their uses](#)

Share this paper:    

View more about this paper here: <https://typeset.io/papers/emerging-optical-properties-from-the-combination-of-simple-3lqwvsy2jc>

HARVARD UNIVERSITY  
Graduate School of Arts and Sciences



DISSERTATION ACCEPTANCE CERTIFICATE

The undersigned, appointed by the

Harvard John A. Paulson School of Engineering and Applied Sciences

have examined a dissertation entitled:


“Emerging Optical Properties from the Combination of Simple Optical Effects”

presented by: Grant Tyler England


candidate for the degree of Doctor of Philosophy and here by  
certify that it is worthy of acceptance.

Signature \_\_\_\_\_ 

Typed name: Professor J. Aizenberg

Signature \_\_\_\_\_ 

Typed name: Professor M. Loncar

Signature \_\_\_\_\_ 

Typed name: Professor R. Westervelt

Signature \_\_\_\_\_ 

Typed name: Professor M. Kolle

Date: October 25, 2016



# Emerging Optical Properties from the Combination of Simple Optical Effects

A thesis presented

by

Grant Tyler England

to

The School of Engineering and Applied Sciences

in partial fulfillment of the requirements

for the degree of

Doctor of Philosophy

in the subject of

Applied Physics

Harvard University

Cambridge, Massachusetts

October 2016

©2016 - Grant Tyler England

All rights reserved.

Thesis advisor  
**Joanna Aizenberg**

Author  
**Grant Tyler England**

## **Emerging Optical Properties from the Combination of Simple Optical Effects**

### **Abstract**

This thesis explores the intersection of materials science and optics that is colored materials. Traditionally, this field has been limited to structurally colored materials; however, with the advent of plasmonic nanoparticles with designed absorptivities and metamaterials, there has been an increase in the number of fabrication methodologies for colored materials which has also led to the discovery of new types of colored materials that would not typically be considered to be structurally colored. With this expansion, researchers in the field of structural color are creating hybrid materials that rely on both the nanoscale morphology of structurally colored materials and the addition of absorption to these materials which causes a host of different effects.

This thesis will first give an overview of a type of classical structural color research that is still very active—self assembled structurally colored materials. Chapter 1 presents a brief review of the field, focusing on colloidal structures and the optical properties obtainable by utilizing different materials, geometries, and additives with colloidal self-assembly. Chapters 2 and 3 present specific examples of these types of structurally colored materials. Chapter two focuses on photonic balls made of spherically assembled colloidal particles. Chapter 3 presents a lithographic method for adding hierarchy to a surface-assembled colloidal photonic crystal. This hierarchy hints at the ability to create novel, combination optical effects by superposing two structural color geometries.

Chapter 4 expands on this idea of combining optical effects with a review on the recent trend in the field of colored materials with the combination of hierarchical structures, the addition of absorption into structurally colored materials, and the addition of plasmonic materials into these structures to create many new types of

---

materials and color effects. Chapter 5 gives an example of the former type of material, wherein two structural color geometries (in this case, a diffraction grating and an orthogonally oriented diffraction grating) are superposed to give a composite optical effect. Chapter 6 gives an example of the addition of absorption into a structurally colored material to generate something more complicated than just the combination of different geometries, wherein the complex refractive index of the material changes the boundary conditions for the accumulated phase in the structure.

# Contents

Title Page . . . . .	i
Abstract . . . . .	iii
Table of Contents . . . . .	v
Citations to previously published work . . . . .	viii
Acknowledgments . . . . .	ix
Dedication . . . . .	xi
<b>1 Optical Applications of Colloidal Photonic Crystals</b>	<b>2</b>
1.1 Overview . . . . .	2
1.2 Factors affecting optical applications . . . . .	6
1.2.1 Composition and additives . . . . .	6
1.2.2 Disorder . . . . .	9
1.2.3 Monolayers . . . . .	9
1.2.4 Superparticles . . . . .	10
1.2.5 Hierarchy/patterning . . . . .	12
1.3 Perspective . . . . .	15
<b>2 Color from hierarchy: Diverse optical properties of micron-sized spherical colloidal assemblies</b>	<b>16</b>
2.1 Overview . . . . .	16
2.1.1 Significance . . . . .	16
2.1.2 Abstract . . . . .	17
2.2 Introduction . . . . .	18
2.3 Results and Discussion . . . . .	20
2.3.1 Synthesis and Internal Morphology of Photonic Balls . . . . .	20
2.3.2 Coloration Arising from Bragg Diffraction . . . . .	23
2.3.3 Mitigating Scattering by Incorporation of Spectrally Selective Absorbers . . . . .	29
2.3.4 Coloration Arising from Grating Diffraction . . . . .	32
2.4 Conclusion . . . . .	39
2.5 Materials and Methods . . . . .	40
2.5.1 Microfluidic Fabrication of Photonic Balls . . . . .	42



2.5.2	Optical Characterization . . . . .	43
2.5.3	Computer Simulations and Theoretical Models . . . . .	43
<b>3</b>	<b>Combining Bottom-Up Self-Assembly with Top-Down Microfabri- cation to Create Hierarchical Inverse Opals with High Structural Order</b>	<b>46</b>
3.1	Overview . . . . .	47
3.1.1	Abstract . . . . .	47
3.2	Introduction . . . . .	47
3.3	Results and Discussion . . . . .	49
3.4	Conclusions . . . . .	57
3.5	Methods . . . . .	58
3.5.1	Preparation of Inverse Opals . . . . .	58
3.5.2	Photolithography on Inverse Opal Film . . . . .	58
3.5.3	Reactive Ion Etching . . . . .	59
3.5.4	Imaging and Characterization . . . . .	59
<b>4</b>	<b>Emerging Optical Properties from the Combination of Simple Opti- cal Effects</b>	<b>60</b>
4.1	Introduction . . . . .	60
4.2	Hierarchy . . . . .	62
4.3	Absorption . . . . .	65
4.4	Plasmonics . . . . .	71
4.5	Conclusions . . . . .	76
<b>5</b>	<b>Bio-inspired micro-grating arrays: Mimicking the reverse color diffrac- tion elements evolved by the butterfly <i>Pierella luna</i></b>	<b>78</b>
5.1	Overview . . . . .	78
5.1.1	Abstract . . . . .	79
5.2	Introduction . . . . .	79
5.3	Mimicking <i>P. Luna</i> . . . . .	82
5.4	Analysis . . . . .	84
5.5	Conclusions and Discussion . . . . .	91
5.6	Materials and Methods . . . . .	92
5.6.1	Manufacture of artificial diffraction structures . . . . .	92
5.6.2	Structural and optical analysis . . . . .	93
5.6.3	Optical modeling . . . . .	94
<b>6</b>	<b>The Optical Janus Effect: Asymmetric Structural Color Reflection Materials</b>	<b>96</b>
6.1	Overview . . . . .	96
6.2	Janus Thin Films . . . . .	98

6.3	Theory . . . . .	99
6.4	Multilayer Janus Stacks . . . . .	103
6.5	Patterning of Janus Films . . . . .	103
6.6	Methods . . . . .	107
6.6.1	Nanoparticle Synthesis . . . . .	107
6.6.2	Nanoparticle Binding . . . . .	108
6.6.3	Bragg Stack Formation . . . . .	109
6.6.4	Nanoparticle Functionalization / Patterning . . . . .	109
6.6.5	Optical Characterization . . . . .	110
6.7	Derivation of First Order Approximations . . . . .	113
6.7.1	Thin Film . . . . .	113
6.7.2	Absorbing layer between the dielectric and the substrate . . .	114
6.7.3	Choosing a different "cavity" . . . . .	115
6.7.4	Summary of Approximations . . . . .	116
6.7.5	Discussion of Approximations . . . . .	117
6.8	Additional Experiments . . . . .	117
6.9	Conclusions . . . . .	119
	<b>Bibliography</b>	<b>121</b>

# Citations to previously published work

Parts of this dissertation cover research reported in the following articles:

1. England, Grant, et al. "Bioinspired micrograting arrays mimicking the reverse color diffraction elements denise levolved by the butterfly Pierella luna." *Proceedings of the National Academy of Sciences* 111.44 (2014): 15630-15634.
2. Philips, Katherine R; England, Grant T, et al. "A Colloidoscope of Colloid-Based Porous Materials and Their Uses." *Chemical Society Reviews* 45.2 (2016): 281-322.
3. Schaffner, Manuel; England, Grant, et al. "Combining Bottom-Up Self-Assembly with Top-Down Microfabrication to Create Hierarchical Inverse Opals with High Structural Order." *Small* 11.34 (2015): 4334-4340.
4. Vogel, Nicolas; Utech, Stefanie; England, Grant T; et al. "Color from Hierarchy: Diverse Optical Properties of Micron-Sized Spherical Colloidal Assemblies." *Proceedings of the National Academy of Sciences* 112.35 (2015): 10845-10850.
5. Grant England and Joanna Aizenberg. "Emerging Optical Properties from the Combination of Simple Optical Effects" *Manuscript in preparation*.
6. England, Grant; Russell, Calving; Shirman, Elijah; Kay, Thersa; Vogel, Nicolas; Aizenberg, Joanna. "The Optical Janus Effect: Asymmetric Structural Color Reflection Materials" *Manuscript in preparation*.

# Acknowledgments

This thesis is largely an answer to a question I frequently ask myself: "Where did all the time go?" What follows is a copy-paste journey through my life for the past 6 years.

First, I want to thank my advisor Prof. Joanna Aizenberg. When I didn't have a group to join or a clear direction to navigate through grad school, she allowed me to join her group and gave me that direction. The group she fostered at Harvard allowed me to have many meaningful and educational collaborations both within and external to the ever-changing group. During every group meeting presentation I gave, she always had helpful advice for which research directions I should focus on and how to know when to stop working on a project and start writing.

Nearly as importantly, I need to thank Prof. Mathias Kolle. When I joined the Aizenberg group, he was a post-doc that took me, as an inchoate grad student, and began the process of molding me into an independent researcher. Mathias was as much an advisor to me as Joanna, and without his guidance during my first few years, I could have easily gotten lost in such a large group.

Next, I need to thank Prof. Niki Vogel. After Mathias left for MIT, he filled the void left behind, providing me with answers to anything I needed to know about colloids or designing experiments or writing and publishing results. Without his invitation to work in his group in Germany, I would likely have never visited Europe and gained a more global perspective on how research is done. I should also thank the students and post-docs in his group who provided me with both cultural and scientific support during my visit, especially Steffi Vogel, Karina Bley, Marcel Rey, and Denise Niederkorn.

For keeping me publishing and sane throughout my PhD, I need to thank many members of the Aizenberg group: Dr. Katherine Phillips, who collaborated with me whenever possible on colloid-based structurally colored materials in her research, and kept my spirits up even when experiments were not going well; Drs. Elijah and Tanya Shirman who provided me with answers to any fabrication or nanoparticle questions I might have; Theresa Kay, for allowing me to constantly steal her bench space in lab and always being willing to help me out with a fabrication procedure—even when she was overworked; Calvin Russell, who forced me to become a mentor by

simply deciding (independent of my will) that I would be his mentor; and Dr. Alison Grinthal, who provided me and the entire lab support for how to convert a multi-year research project into a coherent story to be published.

I should also thank many members of the Mazur group for providing support and optics expertise when I needed outside help. Especially, I would like to thank Phil Camayd-Munoz and Orad Reshef for enduring the hardships of a PhD alongside me.

Finally, I should thank my family for supporting me throughout my PhD and pushing me to complete my degree rather than remain a perpetual graduate student.

### **Acknowledgements of Financial Support**

Parts of this work was supported by the US Air Force Office of Scientific Research Multidisciplinary University Research Initiative under Award FA9550-09-1-0669-DOD35CAP. Parts of this work was supported by the National Science Foundation (NSF) Materials Research Science and Engineering Centers (MRSEC) at Harvard University under Award No. DMR 14-20570 and by the Badische Anilin und Sodafabrik's North American Center for Research on Advanced Materials.

*To my family*

Page intentionally left blank

# Chapter 1

## Optical Applications of Colloidal Photonic Crystals

This chapter covers a brief overview of self-assembled, structurally colored materials created using monodisperse colloids. The focus here is on how changes in the constituent materials and assembly parameters can affect the properties of the final structurally colored materials. Applications of these types of three-dimensional photonic crystals are highlighted throughout.

### 1.1 Overview

In nature, colloidal particles have been used to change the visual appearance of various organisms in several ways, including by providing additional scattering, [1] allowing for angle-independent structural color, [2] or providing bright, ordered structural color. [3] Colloids are useful in natural and biomimetic structural color applications because they have sizes on the same length scale as the wavelength of visible light, such that one can tune the optical properties of materials created from colloids by varying the size of the colloidal building blocks or the dielectric constant of the material. Multi-step, hierarchical fabrication methods further enable additional optical properties occurring at larger dimensions such as grating effects and angular reflection properties. Structurally colored materials are increasingly sought for



a wide range of applications, including high reflectivity mirrors, anti-reflective coatings, and optical fibers, as well as color elements for paint, cosmetics, decoration, or display technologies, and colloids are often used to template the photonic materials that enable these technologies due to their ease of fabrication and versatility. In particular, colloids can be assembled into structures with periodicity in all three spatial dimensions on the same order as the wavelength of visible light, forming 3D photonic crystals. By changing the material composition of these 3D photonic crystals-whether by using absorbing additives, responsive materials, or flexible materials-a variety of optical effects can be created. Fig. 1.1 schematically illustrates examples of different material parameters that can be tuned to modify the photonic properties of CBPM, with the resulting reflection spectra shown as insets. It should be noted that, although direct opals are shown in the schematics, the optical effects apply in the same way to inverse (templated) structures.

In addition to tailoring the properties of the individual colloids to tune the optical properties of CBPM, the assembly of colloidal particles can also be varied in several ways to alter the angle-dependence of the structural color (Fig. 1.2). Patterning the CBPM can enable more complicated security printing or display applications by allowing for more complex optical materials to be created, such as diffraction gratings (Fig. 1.2B). Changing the degree of order of the structure can drastically reduce the angle dependence of a structurally colored material, allowing for a much more angle-independent structural color (Fig. 1.2C). Assembling the opal structures further into dispersible particles either by top-down (i.e. grinding) or bottom-up (i.e. microfluidics) methods is an alternate method of changing the angle-dependent properties (Fig. 1.2D and E).

There are several parameters that can be used to tune the optical properties of colloidal crystals and derivatives thereof. The location of the Bragg peak in a photonic structure can be tuned in several ways as can be seen in the well-known Bragg-Snell equation (assuming a close-packed 111 lattice):

$$\lambda = \sqrt{\frac{8}{3}}D\sqrt{(\phi_1n_1 + \phi_2n_2)^2 - \sin^2\theta} \quad (1.1)$$

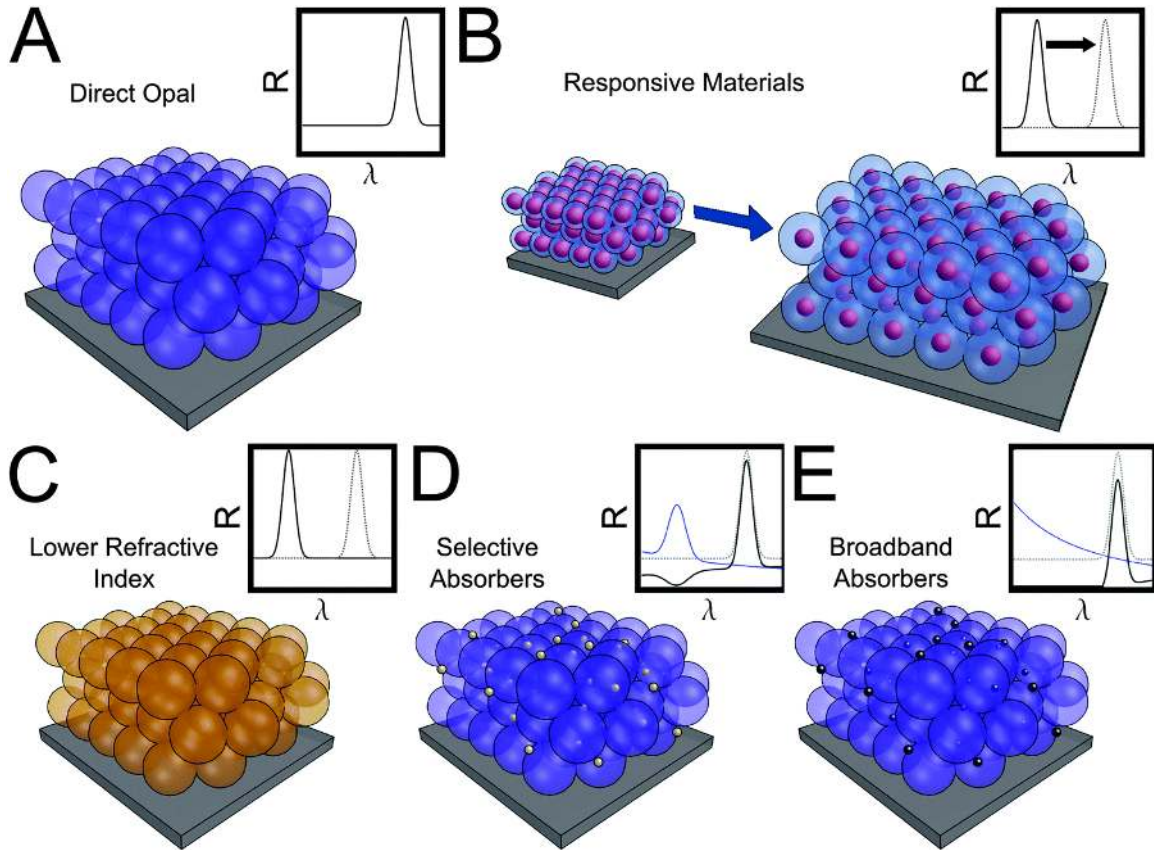


Figure 1.1: Schematic of the influence of materials properties on the photonic peak of an opal. (A) A direct opal. (B and C) Direct opals formed from different types of colloids: (B) core-shell colloids, which can change size (and color) in response to a stimulus, and (C) colloids made of a material with a lower refractive index than in (A), resulting in a blue shifted spectrum. (D and E) Direct opals with (D) selective and (E) broadband absorbers. Insets show schematics of the reflected Bragg peak of the structure (black line, A-E), the reflected Bragg peak of the reference structure shown in part A (gray line, B-E), and the absorption spectra of the absorbers added to the material (blue line, D and E).

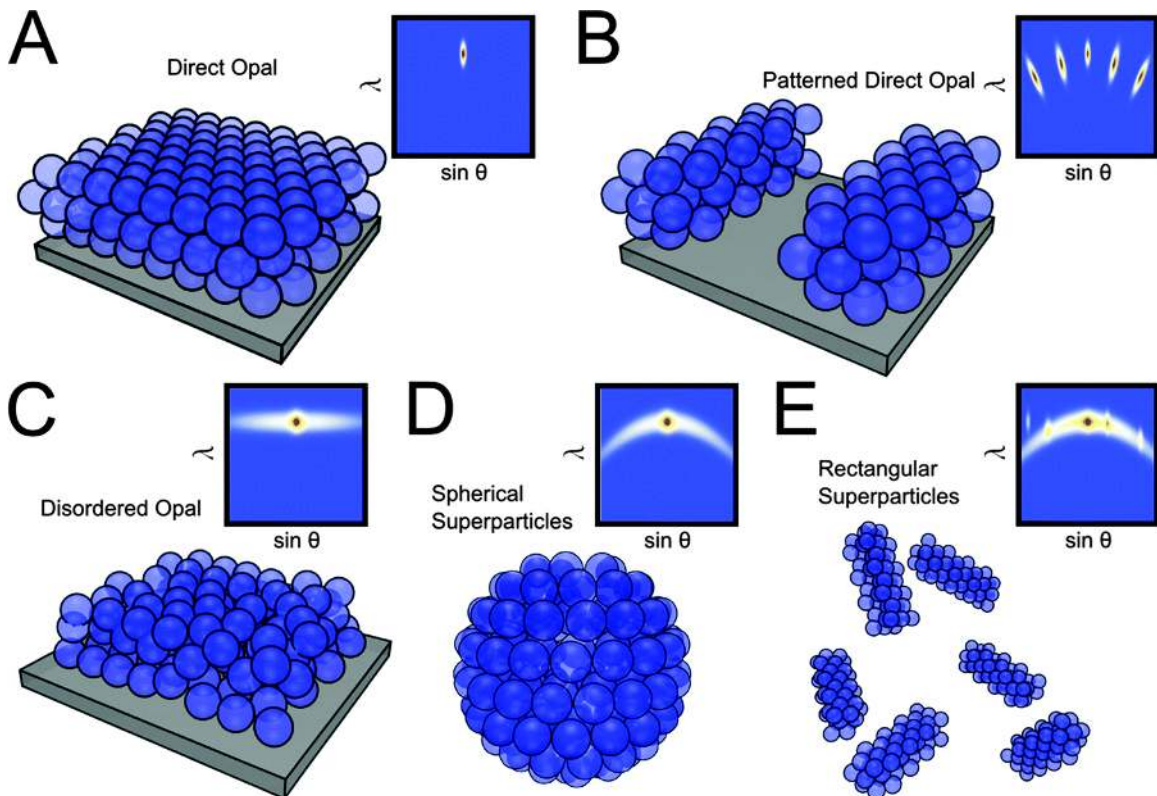


Figure 1.2: Schematic of various methods for changing the angular dispersion of structural color in CBPM. (A) A direct opal. (B-E) Direct opals in various geometries: (B) patterned, (C) disordered, and (D and E) assembled in confinement—both (D) spherical and (E) rectangular. Insets show schematics of the reflected spectra for various detection angles, assuming normal incidence illumination.

where  $\lambda$  is the location of the Bragg peak of the structure,  $D$  is the diameter of the colloids used in the HCP structure,  $\phi_{1,2}$  and  $n_{1,2}$  are the volume filling fractions and refractive indices of the constituent materials (colloids and air for direct opals or voids and matrix for indirect opals), and  $\theta$  is the incidence angle measured from the surface normal. Note that while the parameters in eqn (1.1) can be used to modify the photonic stopband, the location of the photonic peak of the structure is not the only parameter that affects the appearance of the material. The bandwidth of the peak, the presence of additional orders, and the amount of scattering in the structure can also strongly influence the macroscopic appearance of the material. It should also be noted that this equation ignores the effects of color saturation that can be modified by changing the number of layers in the structure or adding in absorptive elements. Additionally, this equation assumes a close-packed, ordered lattice; changing either of these properties also affects the optical properties of the material. Overall, several parameters of the CBPM can be varied combinatorially to tune the optical appearance of hierarchical porous colloidal materials. The position of the Bragg peak can be controlled by the periodicity of the structure, the refractive index of the constituent materials, the presence or absence of absorption in the material, and the number of periods of the structure. Other properties of the material can affect the angular dispersion of the structural color, such as the degree of order of the structure or the inclusion of hierarchical geometries in the structure (Fig. 1.2). Below, we discuss in detail how these multifaceted approaches can lead to a diversity of advanced optical behaviors across a broad range of applications.

## **1.2 Factors affecting optical applications**

### **1.2.1 Composition and additives**

Structural colors are not susceptible to photobleaching, so there is a large drive in the field to generate rich and varied colors for use as photonic pigments for paints and cosmetics. Historically, many different types of thin films of opals, inverse opals, and other colloid-derived materials have been used for their photonic properties. [4,

5] Since scattering can greatly reduce the saturation of a photonic color, adding absorbing elements to the matrix can enhance the color of the structure. Fig. 1.3A shows examples of different structural colors that can be created from powderized inverse opal films.

More recently, core-shell colloids (typically silica core with polymeric shell) have been used to generate films of opal or inverse opal photonic crystals on different substrates [9, 10] using organic shell components that can be annealed to enhance adhesion to the substrate or increase the mechanical durability of the film. Currently, the production of imperfect structures leads to non-negligible scattering that desaturates any structural color produced. Through the incorporation of broad spectrum absorbers [6, 11, 12] or plasmonic absorbers, [13–16] this scattering can be reduced, although in the case of the broad spectrum absorbers the photonic peak intensity is also reduced. For example, Steller’s jays have blue feathers due to melanin coupled with disordered colloidal particles. [17] These additives purify the color and enable pigment and coating applications to access a broader color space than would otherwise be possible.

By using responsive materials as the matrix, reversibly tunable colors can be achieved. The color shift of such materials is caused by a change in either the periodicity of the structure or the refractive index of its constituent materials. For security materials, optical switches, or dynamic display applications, it is important to be able to reversibly switch the structural color of CBPM either in an on/off configuration or by a measurable shift in the photonic stopband location. These responsive CBPM can also be used as sensors, as discussed in more detail below. There are several mechanisms that can be used to enable this switching, including the incorporation of magnetic particles to switch between ordered and disordered structures, [18–21] the use of elastomeric materials to allow change in the periodicity of the structure upon application of strain, [7, 22–24] the inclusion of light-responsive moieties to change the average refractive index in the material, [25, 26] and the implementation of redox-sensitive materials [27] and thermo-responsive materials [24, 25, 28, 29] to change the lattice parameter typically by swelling and deswelling. An example of an elastomeric stretch-tunable structural color can be seen in Fig. 1.3B, where the peri-

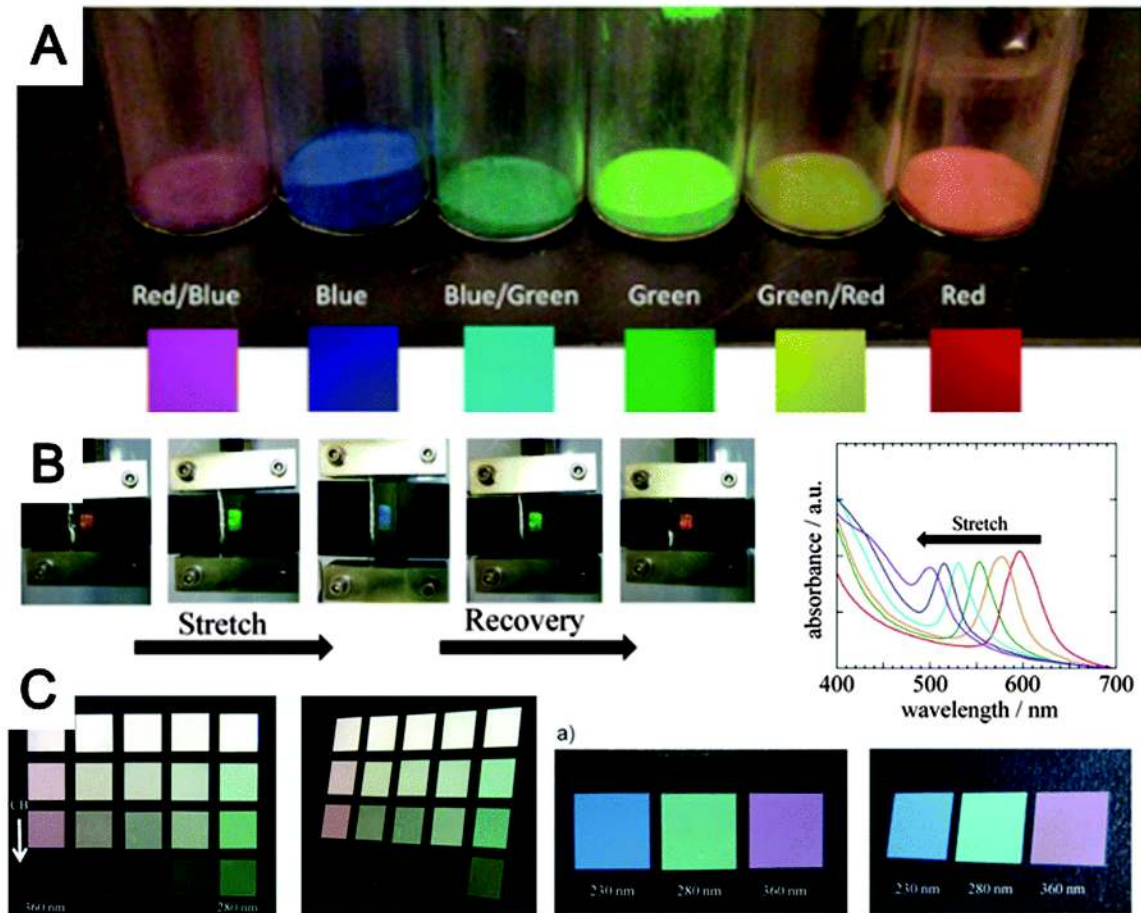


Figure 1.3: Structural color created from colloidal photonic crystals. (A) Silica inverse opal powders with various pore sizes (red, 360 nm; green, 336 nm; blue 288 nm; other colors are 1:1 mixes of these) with mixed RGB reference images. [6] Reproduced with permission from John Wiley and Sons, copyright 2014. (B) Images of a stretched colloidal crystal elastomer and absorbance spectra showing the position of the Bragg peak for different strain values. [7] Reproduced with permission from the American Chemical Society, copyright 2013. (C) Disordered opal structure generated by spray coating, showing: left, color change by adding different amounts of carbon black to mixtures of two different colloid sizes; right, different colors for different sizes of colloids. [8] Reproduced with permission from John Wiley and Sons, copyright 2013.

odicity changes upon stretching due to the Poisson ratio of the elastomeric material, causing a reversible blue-shift in the photonic peak of the opal structure. Photonic crystals like these can also be used as the gain media for colloidal crystal lasers as discussed in detail in a recent review. [30]

### **1.2.2 Disorder**

While typically order is necessary for photonic structures, disordered colloidal structures-which still exhibit structural coloration-have also been studied. [2, 4, 8, 31, 32] For many color applications, the iridescent structural color of photonic crystal materials is undesirable. Nature has solved this problem by incorporating disorder into its photonic structures in order to increase their angular visibility, for example in the feather shown in Fig. 1A(i and ii) [17, 33, 34] Similarly, disorder introduced into CBPM can lead to angle-independent structural colors. [8, 31, 32, 35–37] An example of such angle independence can be seen in Fig. 1.3C. It should be noted that there is a blue tinge to the colors that can be produced using this method. This additional blue coloration is caused by the wavelength-dependent scattering from the photonic materials and may be undesirable for the creation of longer wavelength colors. In order to create high-saturation structural colors, this scattering must be reduced either by incorporating selective absorbers as mentioned above or by creating defect-free materials. [31]

### **1.2.3 Monolayers**

In addition to 3D photonic crystals, 2D colloidal monolayers can also be tuned to create many different optical materials and properties. For example, the monolayer can be used for shadow deposition to generate different shapes of deposited materials, [38–41] used as an etch mask to generate high aspect ratio structures with high order, [16, 42, 43] inverted/textured to create antireflective coatings for reducing the amount of reflected light from a substrate surface, [44] or deformed to generate structurally colored patterns on a substrate. [45] Interesting coupling effects can be observed between the photonic modes of an opal and the plasmonic modes of thin metals

deposited on top of the crystal. [41, 46–49] Colloids can also be used for antireflective coating applications. [50] In particular, colloidal monolayers have been used to create porous, graded-index materials with low reflectivity by, for example, plasma etching of colloidal monolayers, [51] inverting the monolayer, [44] or using the monolayer as an etching mask to generate pillars. [16, 42, 52] To reduce the reflection from the top surface of solar cells, many methods are used to generate porous materials with the proper optical thickness and effective index for optimal transmission. A recent perspective discusses many of these methods. [53] Specifically, colloidal materials can generate high porosity, creating the ability to reach the  $\sqrt{n}$  effective refractive index required for perfect transmission at the desired wavelength. [54] There are several ways to generate the graded effective refractive index profile that causes the antireflective effect of these coatings. Very small colloids (<30 nm), such as organically modified silica (ORMOSIL) particles, can be used to generate uniform antireflective coatings, but typically require the addition of stabilizing elements to make robust films. [55–57] Larger colloids can be used, with or without other materials, to generate hierarchically structured materials with very high transmission values. [43, 58, 59] Fig. 1.4 shows an example of such a structure created by using a monolayer of colloids as an etch mask to make a grating structure on which a disordered array of gold nanoparticles is created. This array of nanoparticles is then etched to create a hierarchical structure with better antireflective properties than the original structure. The transmittance was found to increase after the surface treatment (Fig. 1.4C).

Colloidal monolayers can even generate structural color if surface diffraction modes are used as the source of the structural color. [45] This type of material has a much more angle-dependent structural color as compared to fully three-dimensional photonic crystals due to the nature of the surface diffraction.

### **1.2.4 Superparticles**

Another way to create angle-independent structural color is via modification of the local geometry. By using spherical or hemispherical assemblies of colloids, all viewing directions are normal to some portion of the superparticles. Such assemblies



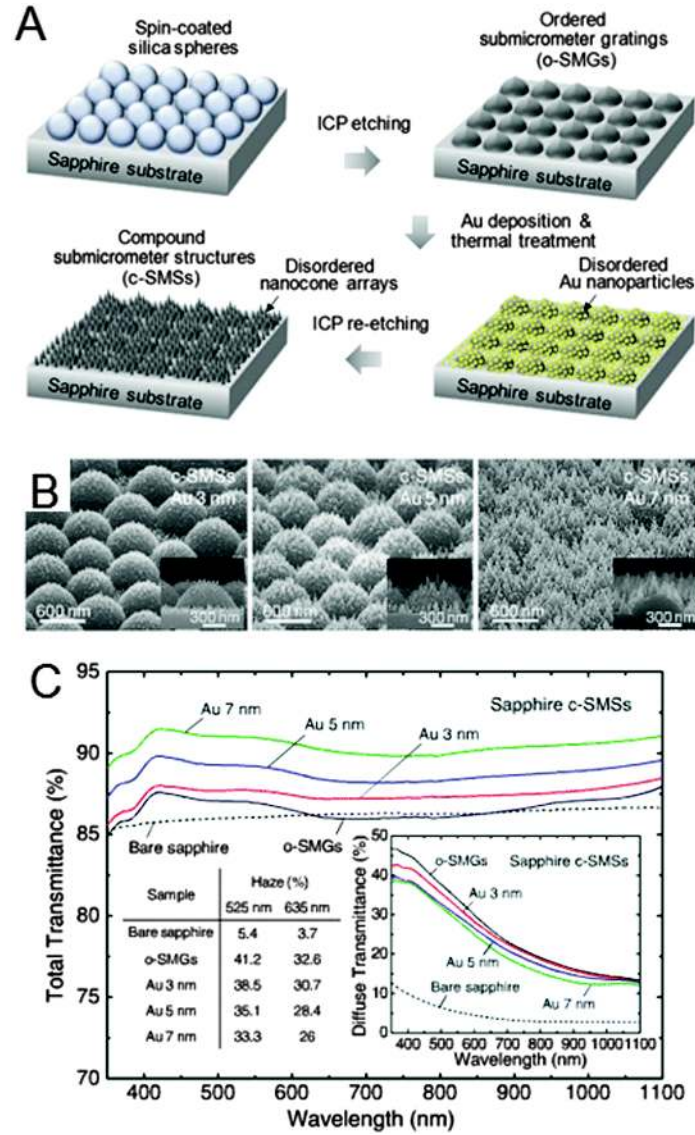


Figure 1.4: Antireflective coating based on hierarchical colloidal lithography. (A) Schematic representation of the fabrication of compound submicrometer structures (c-SMSs) and ordered submicrometer gratings (o-SMGs) for use as antireflective coatings. A layer of colloids is first etched to create o-SMG, which is coated with gold and thermally treated to generate nanoparticles on the surface, which is then etched again to generate a c-SMS. (B) Tilted-angle and side-view (inset) SEM images of hierarchical nanostructure antireflective coatings using Au film thicknesses of 3, 5, and 7 nm. (C) Transmittance spectra for the structures shown in A along with the transmittance spectrum for the bare structure (without the additional gold etching step, black line, o-SMGs). Inset shows the diffuse transmittance spectra and haze ratio values for two different wavelengths for all samples. [43] Reproduced with permission from OSA publishing, copyright 2013.

are typically created via evaporation of a solvent from a droplet containing colloids. These droplets can be created via microfluidics [15, 60] or ink-jet printing. [61, 62] For more information, a recent review covers many of the aspects of these types of photonic crystals. [63] Fig. 1.5 shows inkjet-printed photonic hemispheres (Fig. 1.5A-C) and arrays of buckled-sphere photonic superparticles embedded in a flexible material (Fig. 1.5D), both of which show angle-independent color. It should be noted that the structural color of these photonic superparticles is only independent of viewing angle in a diffusely lit environment due to the near-normal incidence peaks being brighter than the blue-shifted, higher incidence angle peaks. When viewing the structures in transmission or at an oblique angle to a strong lighting source, different photonic or scattering colors can be seen. [15] The creation of disordered superparticles can also strongly reduce angular-dependence of the reflection color, similar to thin films of disordered colloids. [8, 37] Also, when larger colloids are used, diffractive colors become dominant over the Bragg reflectance peak, leading to a much larger variation in color with viewing angle. [15, 64]

Another geometry of dispersible photonic particles is created using fragments of inverse opal films, which can be grown directly into sacrificial channels [14] or ground from larger inverse opal samples [6, 12] to create structural color "pigments" which can be dispersed in paint bases. Structures created in this way have a different visual appearance compared to dense layers of spherical photonic superparticles due to the obvious angle-dependence of the structural color. Since the particles are typically larger, individual domains can be seen by eye, creating a sparkle effect when changing the viewing and illumination conditions. [14]

### **1.2.5 Hierarchy/patterning**

For display applications, the patterning of photonic materials of different stop-bands into pixelated arrays is of great interest. Such patterning has historically been achieved via top-down processes such as photolithography [65–67] or microimprinting, [68] leading to static "pixels" of photonic crystals such as those shown in Fig. 1.6A. Such pixelation can be used to create near arbitrary patterns (images) from

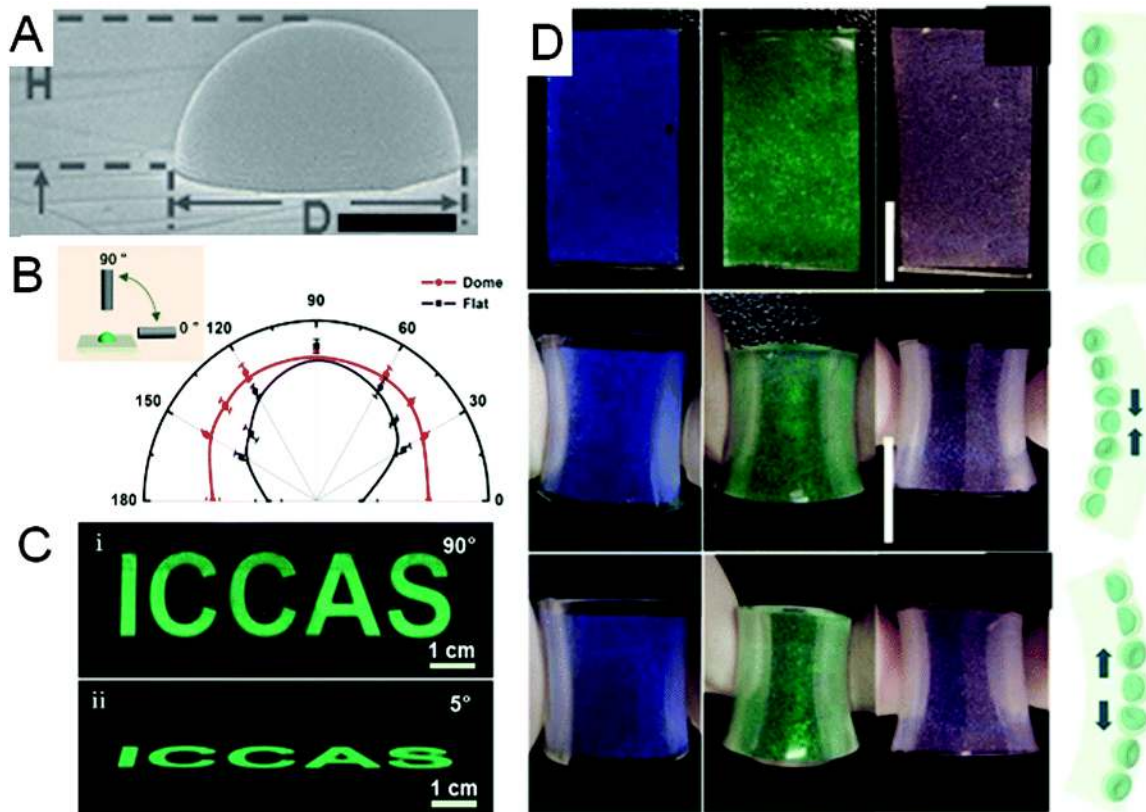


Figure 1.5: Colloidal crystal superparticles with little angle-dependence of color. (A-C) Ink-jet printed hemispherical colloidal superparticles. (A) SEM image of a dome (scale bar: 5  $\mu$ m). (B) Normalized fluorescent intensity of domes (red) and dots (black) for different detection angles. (C) Top and side view images of a pattern of domes showing a wide angular visibility of the color. Reproduced with permission from John Wiley and Sons, copyright 2014. (D) 2.8 cm  $\times$  1.5 cm flexible buckled-sphere colloidal superparticle films showing lack of angle dependence of the structural color upon compression and stretching. Colloid sizes: 170 nm (blue), 200 nm (green), 250 nm (red). [61] Reproduced with permission from the Royal Society of Chemistry, copyright 2015.

structural color materials, provided the desired colors can be generated. An example of an RGB pixelated array can be seen in Fig. 1.6B and C. If magnetic materials are used, architectures closer to an actual display are created [21] in which the color of each pixel can be reversibly changed in an on/off state. The pixels, in this case, consist of magnetic Janus superparticles with colloids comprising half of the sphere to generate a photonic peak that is visible only when the superparticles are in the correct orientation. Since the particles are magnetic, the orientation of each "pixel" can be reversibly switched allowing for images to be created.

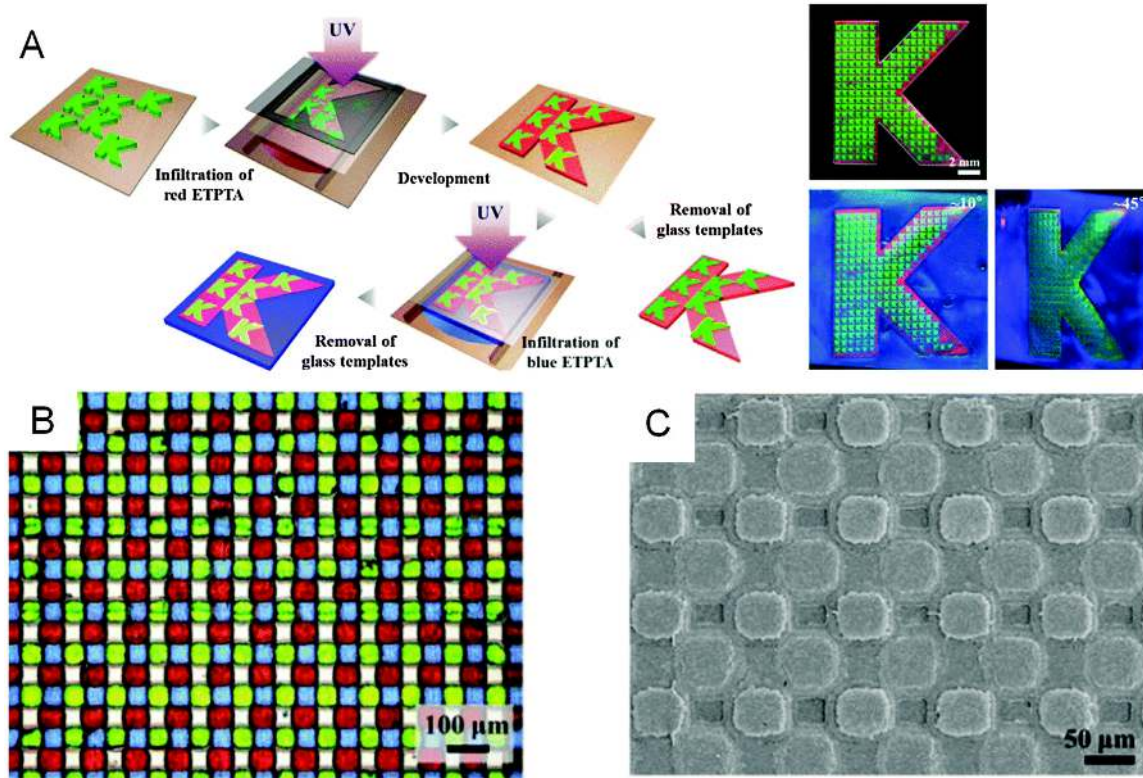


Figure 1.6: Lithographic patterning of colloidal photonic crystals. (A) Left, schematic illustration of patterning method used to make multi-colored colloidal crystals. Right, optical images of films with two and three colors under different viewing angles.144 Reproduced with permission from the American Chemical Society, copyright 2013. (B and C) Hierarchical "pixelated" inverse opal arrays made from SU-8: (B) optical microscopic image of the hierarchical inverse opal, and (C) SEM of the structure. [67] Reproduced with permission from John Wiley and Sons, copyright 2014.

## 1.3 Perspective

CBPM provide a platform for the development of photonic crystal materials due to their relative ease of fabrication, controlled order, and the wide variety of materials from which they can be made. For macroscopic (i.e. wafer-scale or larger) 3D photonic crystals, competing methods such as electron beam lithography and two-photon lithography methods are limited to small sizes, and they require long processing times to create the desired photonic structures due to their serial nature. 1D Bragg stacks and 2D nanowire forest photonic crystals have applications that compete with opal and inverse opal photonic crystals, but they typically lack the benefits of self-assembled systems such as low cost and facile fabrication. Still, crystal lattice defects lead to scattering that greatly weakens the signal-to-noise ratio of the optical response in self-assembled CBPM; it remains a great challenge to increase the order of such materials or to allow for controlled disorder to generate high-chromaticity angle-dependent or angle-independent structural colors.

Additionally, the ability of hierarchical CBPM to be made via top-down lithographic methods or assembly in confinement allows a greater variety of optical properties to be achieved. Research is still needed into creating CBPM with better long-range order and using colloids with higher refractive index materials in order to achieve a full photonic bandgap. [69] Longer-range order and higher refractive indices will generate stronger photonic peaks with less scattering noise, reducing the need to integrate absorption into the material. Increases in the sophistication of CBPM with regard to the dynamic coloration via shifting the photonic stopband or moving the photonic crystal out of view could lead to electronic ink displays with full color displays in the future and advanced security features in anti-counterfeit applications.

## Chapter 2

# Color from hierarchy: Diverse optical properties of micron-sized spherical colloidal assemblies

This chapter covers a specific example of the types of structurally colored materials introduced in Chapter 1. Here, we discuss powder-sized photonic crystals created by droplet-based self-assembly. Both the structural and the optical properties of these "photonic balls" are discussed in detail. Additionally, modeling and simulations for these types of photonic crystals are introduced and corrections to misunderstood optical properties of photonic balls are made.

### 2.1 Overview

#### 2.1.1 Significance

Controlling the internal structure over multiple length scales can produce materials with superior properties. This hierarchical design is ubiquitous in nature where materials have evolved to show maximum functionality from a limited choice of available building blocks. Mimicking the emergence of functionality from simple building blocks is a key challenge for man-made materials. Here, we show how a simple con-

finer self-assembly of colloidal particles leads to a complex geometry that displays a surprising variety of optical effects. These effects are a result of the intricate interaction of light with the structural features at different length scales, and the geometry of the self-assembled structure. The results underline the importance of controlling assembly processes over multiple length scales to tailor properties and maximize performance.

### **2.1.2 Abstract**

Materials in nature are characterized by structural order over multiple length scales have evolved for maximum performance and multifunctionality, and are often produced by self-assembly processes. A striking example of this design principle is structural coloration, where interference, diffraction, and absorption effects result in vivid colors. Mimicking this emergence of complex effects from simple building blocks is a key challenge for man-made materials. Here, we show that a simple confined self-assembly process leads to a complex hierarchical geometry that displays a variety of optical effects. Colloidal crystallization in an emulsion droplet creates micron-sized superstructures, termed photonic balls. The curvature imposed by the emulsion droplet leads to frustrated crystallization. We observe spherical colloidal crystals with ordered, crystalline layers and a disordered core. This geometry produces multiple optical effects. The ordered layers give rise to structural color from Bragg diffraction with limited angular dependence and unusual transmission due to the curved nature of the individual crystals. The disordered core contributes nonresonant scattering that induces a macroscopically whitish appearance, which we mitigate by incorporating absorbing gold nanoparticles that suppress scattering and macroscopically purify the color. With increasing size of the constituent colloidal particles, grating diffraction effects dominate, which result from order along the crystal's curved surface and induce a vivid polychromatic appearance. The control of multiple optical effects induced by the hierarchical morphology in photonic balls paves the way to use them as building blocks for complex optical assemblies-potentially as more efficient mimics of structural color as it occurs in nature.

## 2.2 Introduction

Hierarchical design principles, i.e., the structuration of material over multiple length scales, are ubiquitously used in nature to maximize functionality from a limited choice of available components. Hierarchically structured materials often provide better performance than their unstructured counterparts and novel properties can arise solely from the multiscale structural arrangement. Examples can be found in the extreme water repellency of the lotus leaf [70]; the outstanding mechanical stability and toughness of sea creatures such as sea sponges [71] and abalone shells [72]; and the bright coloration found in beetles, birds, and butterflies [73, 74].

To achieve the strongest visual effects, many organisms combine optical effects arising from light interacting with structured matter at different length scales [75]. Structural periodicity on the scale of visible light wavelengths can result in regular optical density variations that give rise to bright, iridescent colors due to pronounced interference effects [73]. At the micron scale, regular structural features act as diffraction gratings that produce vivid, rainbow coloration [76] and are used to control scattering [77] and to direct the emission of light by mirror-like reflections [78]. At the molecular level, broadband absorption, for example by melanin, can be used to reduce unwanted scattering due to structural imperfections, which, if not eliminated, can lead to a whitish appearance [17].

Several advantages of structural coloration compared with pigmentation hues have led to a strong interest in mimicking nature's photonic design principles in technology [79, 80]. These advantages include increased color longevity by the absence of photobleaching; the ability to use benign and nontoxic materials; broad variation in colors arising from simple changes in geometry of the same material; and the presence of vivid optical effects such as sparkle, luster, and iridescence, not achievable by conventional pigments. However, structural color requires a high degree of control over the nano- and microscale geometry of the colored material. Self-assembly processes involving colloidal particles have been identified as an attractive route to create ordered structures at the nanoscale without the need for expensive and serial nanofabrication methods [4, 5, 81]. Colloidal particles are attractive building blocks for



mimicking nature’s structural coloration strategies because they can be conveniently synthesized in a range of sizes comparable to those of visible light wavelengths. Colloids self-assemble into highly ordered, close-packed crystals on flat surfaces, giving rise to structural color by constructive interference of light reflected at the individual lattice planes [4, 5].

Structural hierarchy, i.e., the organization of colloidal crystals into ordered superstructures, can be achieved by imposing a confining element on the crystallization process. A simple yet interesting confinement for the crystallization process is an emulsion droplet that creates colloidal assemblies known as photonic balls [63, 82–84]. Curvature imposed by the spherical confinement is a unique structural element of photonic balls. It is known that curvature induces different types of defect structures in 2D [85, 86] and 3D assemblies [87], which can affect the resulting optical properties. Photonic balls have recently gained attention in various optical applications, including pigments [21, 88–90], sensors [91], magnetically switchable colorants [21, 92], and color-coded substrates for biomaterials evaluation [93, 94].

Here, we provide a detailed physical understanding of the different optical phenomena occurring in photonic balls and trace the origin of these properties to structural details, especially curvature. We use focused ion beam-assisted cross-sectioning to visualize the effect of confinement on the internal morphology and find ordered, layered crystal planes near the interface and a more disordered region toward the center. Tailoring the degree of confinement allows us to control the crystallinity and thus, the resulting color arising from Bragg diffraction. Disorder and defects, caused by frustrated crystallization in the curved confinement, contributes to unwanted broadband scattering of light, which compromises the macroscopic color. We introduce gold nanoparticles as subwavelength, spectrally selective absorbers into the photonic balls to suppress light scattering in spectrally unwanted regions. This synergistic combination of plasmonic absorption with Bragg diffraction leads to a macroscopically purer coloration, if the photonic crystal stop band and gold nanoparticle absorption are appropriately adjusted. Finally, we observe more complex optical signatures in the reflection of light from photonic balls assembled from larger colloidal particles ( $d > 400$  nm) that result from grating diffraction caused by a regular arrangement of

colloids at the surface of the photonic balls.

Our theoretical experimental examination of the influence of curvature and confinement on the different optical phenomena enables us to create a complete picture of the rich optical properties of these simple, hierarchical self-assembled structures.

## 2.3 Results and Discussion

### 2.3.1 Synthesis and Internal Morphology of Photonic Balls

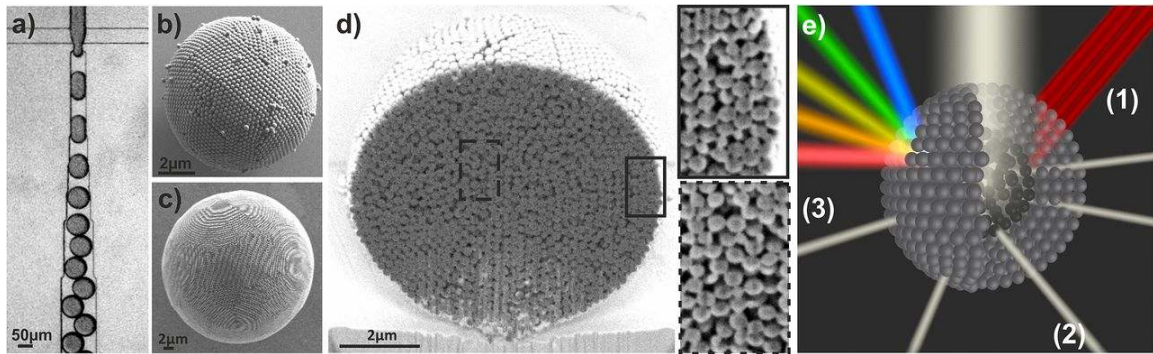


Figure 2.1: Photonic balls are prepared by self-assembly of colloids in the spherical confinement of emulsion droplets. (A) Optical micrograph of the cross-junction microfluidic device used to emulsify a colloidal dispersion into monodisperse droplets. (B and C) SEM micrographs of photonic balls formed by assembly of 250-nm colloids in the confinement of an emulsion droplet (d<sub>ball</sub> = 8 μm in B and 30 μm in C). Moiré patterns visible in C indicate high order. (D) Exemplary cross section of a photonic ball obtained by FIB cutting indicates a layered internal morphology with ordered structure around the interface (Top Inset) and increasing disorder toward the center (Bottom Inset). See Fig. 2.3 for further examples. (E) Schematic illustration of multiple optical effects originating from the hierarchical self-assembly (1): Crystalline order results in Bragg reflection of light with a wavelength defined by the colloid size (2); disorder in the assembly gives rise to unselective scattering of incident light (3); periodic assemblies at the ball's surface lead to grating diffraction effects, separating white light into its spectral components (for colloid sizes >400 nm).

We use droplet-based microfluidics to emulsify an aqueous dispersion of polystyrene colloids in a continuous fluorocarbon oil phase [95]. The cross-junction devices are

conveniently prepared from poly(dimethylsiloxane) (PDMS) by soft lithography and enable us to create stable emulsions with narrow size distributions in a continuous-flow process as illustrated in Fig. 2.1A [96]. After emulsification, the water is removed from the generated droplets at 45 °C, resulting in shrinkage of the emulsion droplets and self-assembly of the colloids in their spherical confinement. We control the diameter of the produced photonic balls from below 10  $\mu\text{m}$  to above 100  $\mu\text{m}$  by tuning the concentration of colloids in the aqueous dispersion and the size of the emulsion droplet generated in the microfluidic device (Fig. 2.2). The surface of the balls, visible in Fig. 2.1 B and C, shows colloids ordered in a polycrystalline, close-packed lattice, previously assigned as the (111) lattice plane of the 3D crystal formed in the spherical confinement [88, 89]. However, the curvature in the confinement impedes the formation of a perfectly ordered crystal, resulting in characteristic defects and assembly structures [85, 86]. A focused ion beam (FIB) was used to cross-section photonic balls and uncover their internal crystal structure, which we show in Fig. 2.1D and Fig. 2.3. The cross-sections reproducibly indicate the presence of a layered morphology of the colloidal crystal toward the interface, consisting of several close-packed [i.e., (111)] planes stacked into a curved 3D crystal. Towards the center of the ball, the assembly appears increasingly disordered, presumably as a consequence of increasing frustration. The higher the level of confinement is (i.e., the smaller the ratio of the diameters of ball and colloid,  $d_{ball}/d_{coll}$ ), the fewer ordered layers exist (Fig. 2.3). It is worth noting that the structures we observe seem less faceted and appear to follow the curvature of the confinement more than would be expected from thermodynamic considerations [87], indicating that kinetic effects may play a significant role in our system.

This curved crystal structure relates to multiple optical properties observed in photonic balls, as schematically illustrated and labeled in Fig. 2.1E. We estimate the amount of order present in photonic balls of a given size based on the intensity of structural coloration that we observe from Bragg diffraction at the ordered lattice planes "(1)". We show that broadband scattering of light, caused by the photonic ball dimensions and the internal disorder, induces a whitish macroscopic appearance "(2)", which can be mitigated by incorporating gold nanoparticles. Finally, we identify the

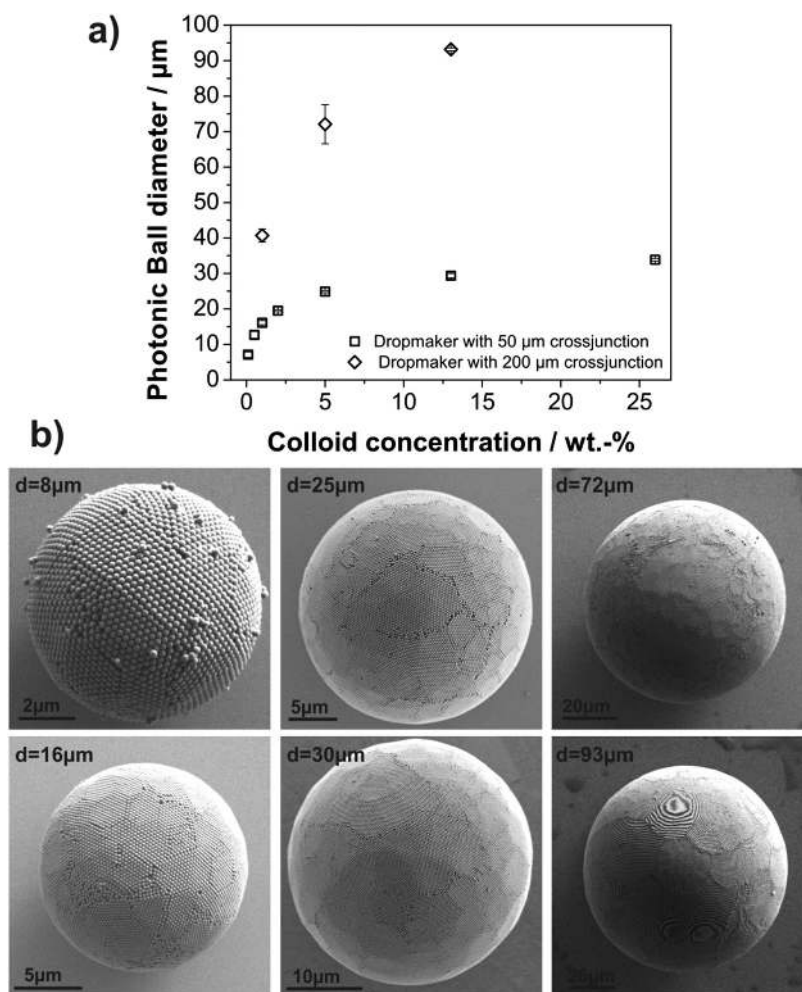


Figure 2.2: (A) Control of the diameter of photonic balls by changing concentration of the aqueous dispersion and the dimension of the cross-junction in the microfluidic synthesis. (B) Representative images of photonic balls with diameters between 8  $\mu\text{m}$  and 93  $\mu\text{m}$ .

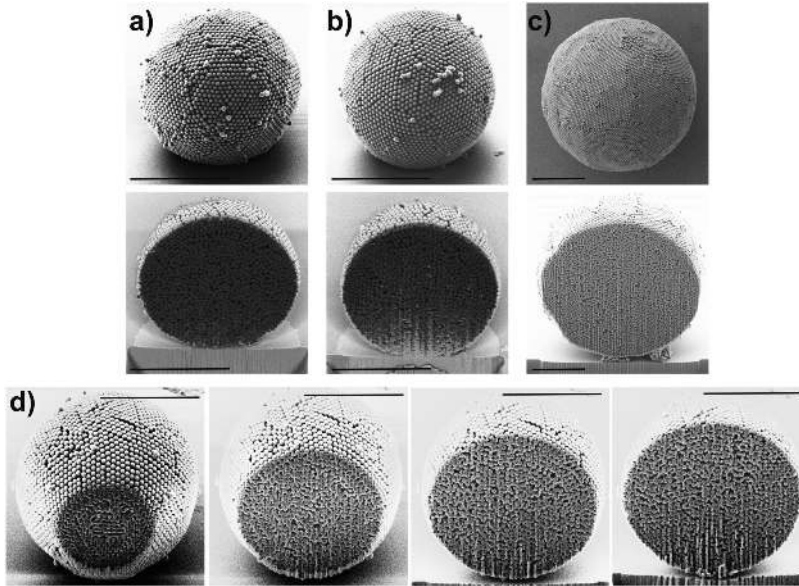


Figure 2.3: (A-C) Additional focused ion beam-assisted cross sections of photonic balls with different diameters: (A and B) 8  $\mu\text{m}$  and (C) 15  $\mu\text{m}$ . A layered crystal structure seems to be present in all cuts. (Scale bars, 5  $\mu\text{m}$ .) (D) Sequence of a FIB cut through a ball, showing the internal structure at various positions within the ball.

ordered arrangement of colloids at the surface of the photonic ball as the origin of color from grating diffraction "(3)".

### 2.3.2 Coloration Arising from Bragg Diffraction

We investigate the color of individual photonic balls, using a fiber-optic cable to collect and spectrally analyze reflected light of individual photonic balls through a microscope objective lens. Fig. 2.4A shows optical images and corresponding measured reflection spectra (solid lines) of individual balls ( $d_{ball} = 30 \mu\text{m}$ ) consisting of colloids with sizes of 180 nm, 225 nm, and 250 nm that display blue, green, and red structural color, respectively. This color has been previously assigned to Bragg diffraction, i.e., constructive interference of light reflected at individual lattice planes in the curved colloidal crystal [88]. The FIB cross sections (Fig. 2.1D and Fig. 2.3) confirm the presence of such layers in our system. A consequence of the spherical nature of the photonic balls is the lack of angular dependence under illumination

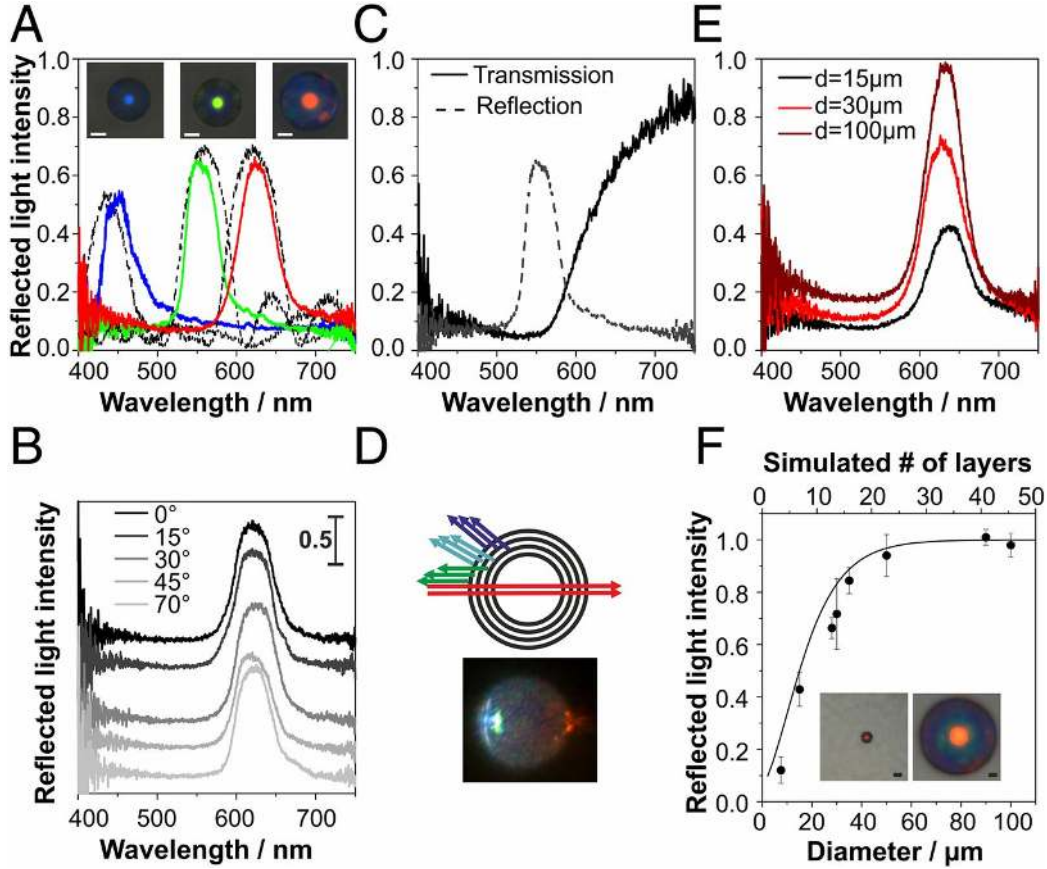


Figure 2.4: Optical properties arising from Bragg diffraction of light at ordered crystal layers. (A) Structural color can be tuned throughout the visible spectrum (solid lines: blue,  $d_{coll} = 180$  nm; green,  $d_{coll} = 225$  nm; red,  $d_{coll} = 250$  nm; photonic ball diameter is  $30 \mu\text{m}$  in all cases) and correlates with 1D simulations (dotted lines) of light reflection at stacked (111) planes within the ball. (B) Reflected light intensity and wavelengths are spectrally independent of the angle of incidence with respect to the substrate surface. (C and D) The transmission spectra of a photonic ball (250-nm colloids) resembles a long-pass filter, which can be explained by the curved nature of the ball and directly visualized by illumination from the side (D). (E and F) The reflected light intensity depends on the size of the photonic balls and reaches saturation for balls with a diameter of  $50 \mu\text{m}$  and larger. The intensity correlates with an increase in the number of ordered layers obtained from simulations (solid line) (F). (All scale bars,  $10 \mu\text{m}$ .) F, Insets show photonic balls with a diameter of  $8 \mu\text{m}$  (Left) and  $100 \mu\text{m}$  (Right).

conditions in a microscope as shown in Fig. 2.4B.

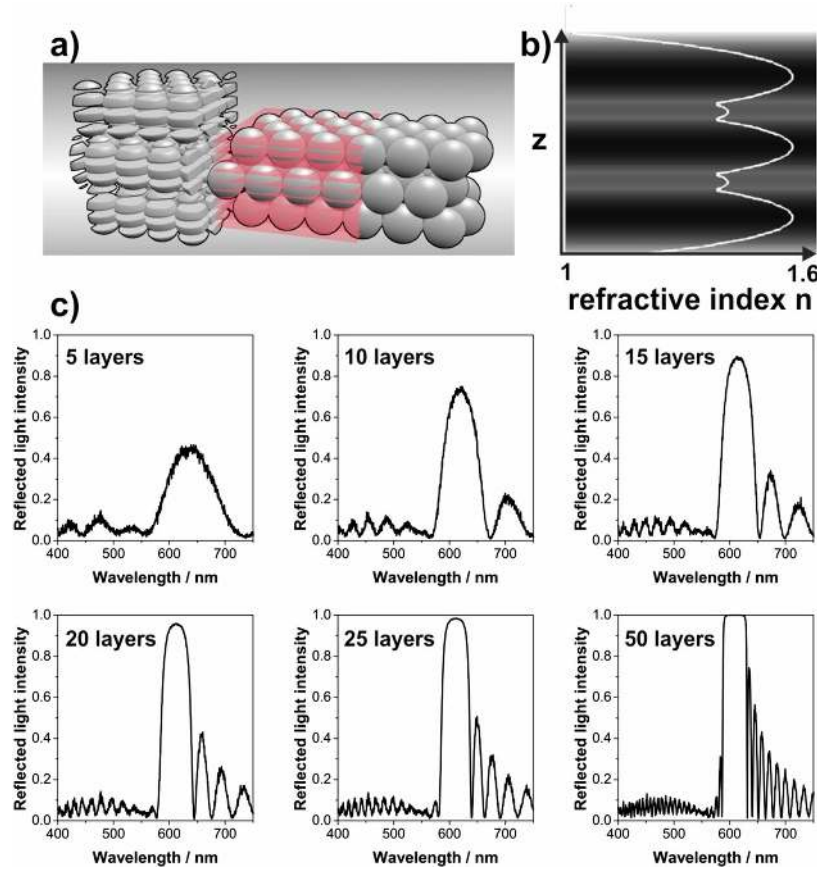


Figure 2.5: Explanation of one-dimensional (1D) transfer matrix calculation of reflectance spectra for photonic balls. The multilayer structure of the ball is simulated as a noncurved thin film; the disorder in the ball’s interior is approximated by a random refractive index material underneath the multilayer structure. (A) Schematic showing the division of the film into discretized layers for averaging to generate an analog 1D multilayer structure. (B) Color plot with line plot overlay showing the refractive index variation along the normal direction of a three-layer polystyrene opal film (darker colors indicate higher refractive indexes). The refractive index was calculated by laterally averaging the permittivity of the opal for each slice. Additional numbers of layers are easily included by repeating the refractive index profile as desired. (C) Calculated reflectance spectra, exemplarily shown for opal films with a colloid size of 250 nm and different numbers of layers. The additional peaks around the main Bragg reflection peak are caused by thin-film interference effects.

We model the photonic balls as a multilayer structure in a 1D transfer matrix

simulation with a refractive index profile corresponding to a stacked, close-packed colloidal crystal (details in Fig. 2.5). The simulated spectra, shown as dotted lines in Fig. 2.4A, match the experiments, corroborating that multilayer interference at stacked (111) planes can cause the observed color. To match the peak intensity, simulations were performed assuming seven (180-nm colloids) and nine (225-nm and 250-nm colloids) perfectly ordered layers of colloidal crystal.

Objective lens	5×	10×	20×	50×
N.A.	0.13	0.25	0.40	0.50
Collection angle	7°	14°	24°	30°
Photonic balls				
$d_{spot}/d_{sphere}$	0.1	0.2	0.24	0.3
Calculated collection angle	10°	15°	27°	33°

Table 2.1: Comparison of the range of angles picked up by microscope lenses with different numerical apertures (N.A.) and the colored area observed in a photonic ball. The angular range calculated from the colored area coincides with the angular range calculated from the N.A. [ $\alpha = \sin^{-1}(N.A.)$  for objectives used in air].

The most prominent feature of the optical microscope images throughout Fig. 2.4 is an area with intense, uniform color in the center of the ball surrounded by a pale, almost colorless rim. We attribute this color pattern to the spherical nature of the hierarchical assembly: Only the center of the photonic ball reflects light that can be detected in the microscope objective (Fig. 2.6A). Larger angles of incident and reflected light—causing a blue shift of color—are not picked up by the microscope objective (Fig. 2.6A), creating the observed uniform coloration. The colorful area of the ball corresponds to the angular range of back-reflected light the objective can collect, which we confirmed by imaging an individual photonic ball with objectives of different numerical aperture and found quantitative agreement between the accessible angles calculated from the numerical aperture of the lens and from the ratio of the colored area to the ball diameter (Figs. 2.6B and 2.7 and Table 2.1). However, this model does not account for colored patches visible at the outer rims of some photonic



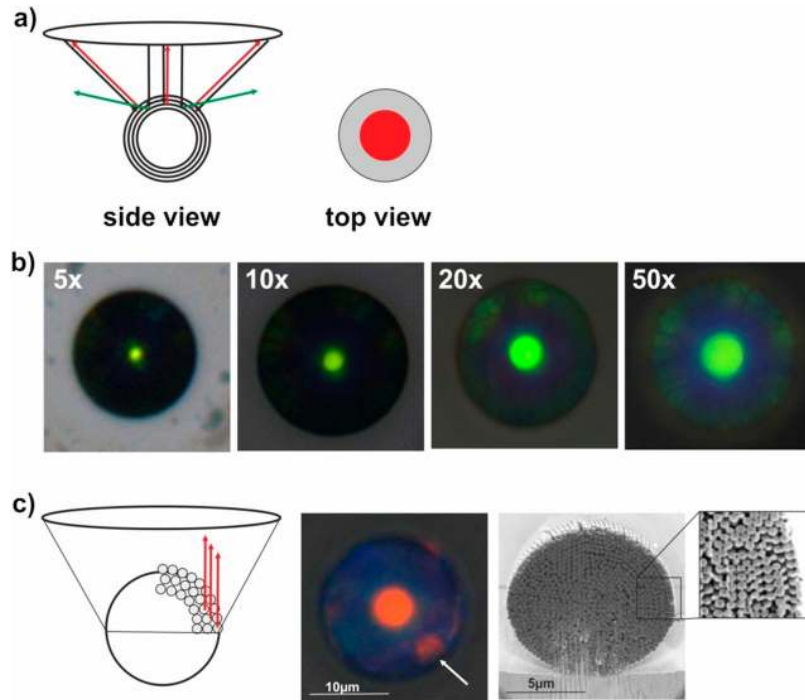


Figure 2.6: Optical details of photonic balls imaged in a microscope. (A) The uniform appearance of color in a central area of the ball with dark outer regions is caused by the curved nature of the photonic ball and the limited range of angles the microscope lens can collect: Only light back reflected normal to the surface is collected by the lens (red arrows); light reflected under higher angles, leading to a blue shift in constructively interfering wavelengths (green arrows), is not reflected within the collection angles. (B) The numerical aperture of the objective defines the colored area of the ball. Higher-magnification lenses, corresponding to larger numerical aperture, enable the collection of light that is back-reflected from a wider range of angles; this larger collection angle leads to an increased diameter of the colored area (see Table S1 for quantification). (C) The colorful patches visible on the edges of some particles (white arrow) may arise from ordered areas normal to the stacked (111) layers. Such periodicities (exemplarily shown in the FIB cross section) allow light to be back reflected into the objective lens even at the edge of the photonic ball.

balls, e.g., in the red-colored ball in Fig. 2.4A. These spots may be caused by light reflected back into the objective at ordered planes perpendicular to the stacked (111) planes, visible in cross-sectional images (Fig. 2.6C).

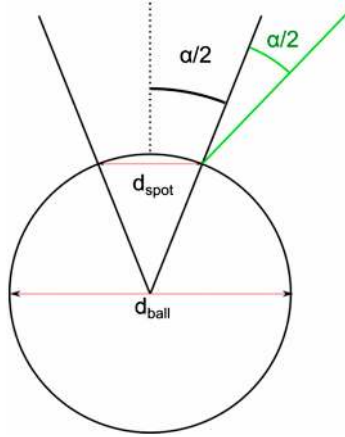


Figure 2.7: Schematic showing how the expected numerical aperture was calculated from the ratio of the diameter of the spot size to the diameter of the ball.  $\alpha$  can be calculated by  $\tan(d_{spot}/d_{ball}) = \alpha/2$ . This formula applies because the maximum incidence angle of light in the setup that should be seen as a bright spot on the photonic ball should be the angle for which the specular reflection is along the microscope axis; the half angle of the numerical aperture ( $\alpha$ ) satisfies this condition.

Unlike typical thin film photonic crystals, photonic balls exhibit transmission spectra that are not the inverse of the reflection; instead, only light above a critical threshold wavelength is transmitted, whereas light with energies higher than the observed reflection peak seems unable to pass the structure (Fig. 2.4C). Again, we attribute this unexpected behavior to the curved nature of the crystal, as schematically illustrated in Fig. 2.4D. Even though only light reflected normal to the ball's surface is picked up in the reflection spectrum (resulting in a green reflection peak in the illustration), reflections also occur at different angles (although they are not picked up by the microscope as described above). Such reflections will have a larger angle between incident and reflected light, which translates to constructive interference occurring at lower wavelengths (i.e., cyan and blue light in the illustration) [97]. Therefore, only light with wavelengths higher than the threshold defined by the constructive interference at normal incidence is transmitted, leading to the transmission

characteristics shown in Fig. 2.4C. This phenomenon can be observed directly, if a photonic ball is illuminated from the (Fig. 2.4D).

The size of the photonic balls, and thus the confinement of the colloids, can easily be controlled synthetically. Fig. 2.4E exemplarily shows reflection spectra of photonic balls prepared from 250-nm colloids with a size of 15  $\mu\text{m}$ , 30  $\mu\text{m}$ , and 100  $\mu\text{m}$  (to-scale microscope images are shown in Fig. 2.4F, Insets). With increasing size of the photonic ball, the intensity of the Bragg reflection peak increases and reaches values close to saturation for balls with a size of 50  $\mu\text{m}$  (Fig. 2.4F). This indicates an increase in crystallinity as a result of a less severe confinement with increasing ball size. We then compare the measured reflected light intensity for different ball diameters with simulated values of multilayer reflection with increasing numbers of crystalline layers (Fig. 2.4F). The measured reflectivities closely follow the simulated values, indicating that the amount of order is directly correlated to the degree of confinement. Consequently, we can use optical information to indirectly assess the degree of internal order of individual photonic balls by comparing the measured and simulated intensity of reflected light.

### **2.3.3 Mitigating Scattering by Incorporation of Spectrally Selective Absorbers**

The spherical confinement of the photonic balls inherently induces disorder in the colloidal arrangement, leading to a whitish appearance due to scattering. To create structural color with high chromatic values, the nonresonant scattering needs to be controlled. The addition of broadband absorbers (for example, carbon black) can suppress scattering, increasing the contrast between spectral background and Bragg diffraction peak [11, 98]. However, the Bragg peak itself can be decreased as well due to the unselective nature of absorption. In contrast, light absorption of noble metal nanoparticles at their plasmon resonance frequency occurs over a rather narrow part of the visible spectrum and can be tuned by changing size and shape of the metal nanoparticle [99]. Such nanoparticles can serve as spectrally selective absorbers that absorb scattered light at undesired wavelengths [14]. Most importantly, their absorp-

tion frequency can be tailored to minimize interference with the Bragg diffraction peak of the photonic crystal. This leads to a purification of the optical spectrum by suppression of the intensity of scattered light from undesired parts of the spectrum with minor effects on the intensity of the Bragg peak.

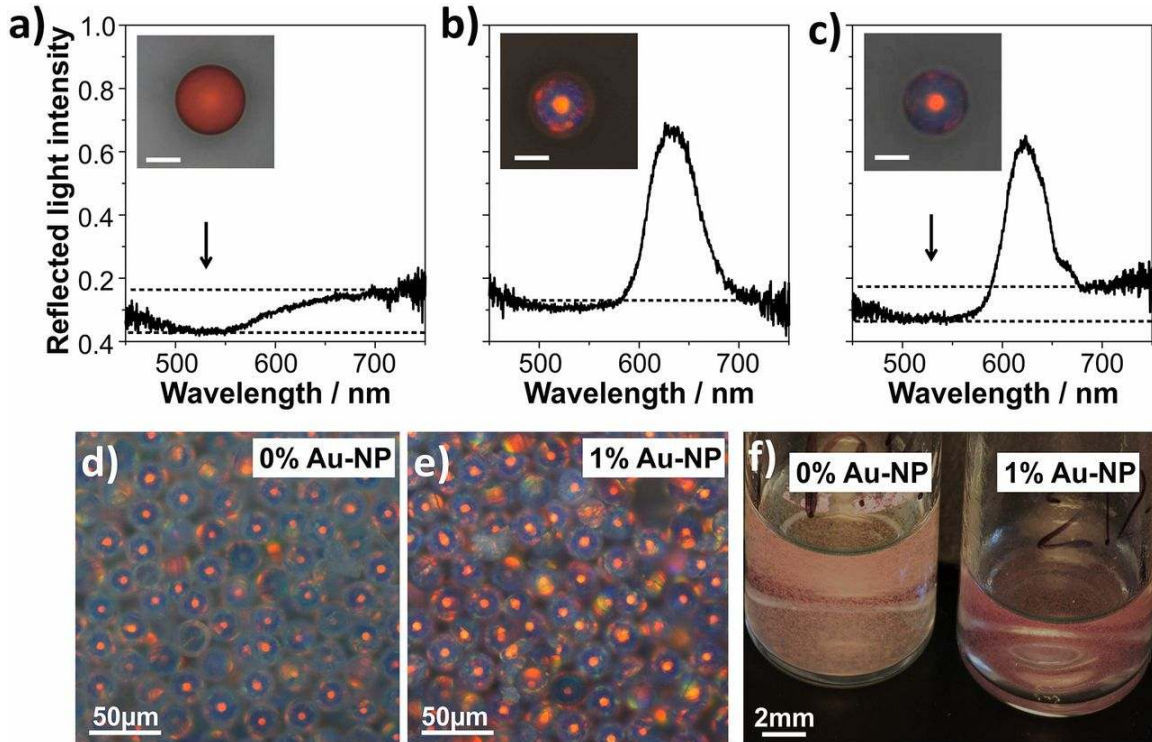


Figure 2.8: Color purification by incorporation of spectrally selective absorbers. (A) Reflection spectra of a disordered photonic ball (binary mixture of colloids with  $d = 200$  nm and 250 nm) with 12-nm Au nanoparticles (NPs). The absorption of the Au NPs lowers the reflection of light in the blue/green part of the spectrum (arrow), giving the ball a dull, red appearance (A, Inset). (B) An ordered photonic ball ( $d_{\text{colloids}} = 250$  nm) shows a Bragg reflection peak at 620 nm, leading to a bright, red color (Inset). (C) An ordered photonic ball with gold nanoparticles shows lowered reflection at the blue/green part of the spectrum without affecting the Bragg reflection peak. (D-F) Control of scattering properties by addition of Au NPs in ensembles of photonic balls. Microscopic images (D and E, taken with identical exposure times) and macroscopic images (F) reveal an increased contrast.

Here, we use 12-nm gold nanoparticles (details in SI Materials and Methods) to mitigate the whitish appearance caused by the presence of disorder, producing a more

crisp red coloration as demonstrated in Fig. 2.8. Due to their small size, the gold nanoparticles do not interfere with the assembly of the colloidal particles, enabling the creation of hybrid photonic-plasmonic balls [64]. Fig. 2.8 A-C shows single-particle spectra of three different types of such hybrid balls. A disordered ball containing gold nanoparticles, prepared by mixing two populations of colloidal particles with diameters of 200 nm and 250 nm chosen to induce disorder by lattice mismatch, does not show a Bragg reflection peak (Fig. 2.8A). The plasmon resonance of the gold nanoparticles leads to a dip in the reflection spectrum at 520 nm, indicated by an arrow in Fig. 2.8A, resulting in a dull, reddish appearance. An ordered photonic ball, consisting of 250-nm colloids without gold nanoparticles, is shown in Fig. 2.8B, with a red color stemming from the Bragg diffraction peak at 600 nm. Figure 2.8B shows a photonic ball without gold nanoparticles that shows a Bragg diffraction peak at 620 nm. The addition of gold nanoparticles to an ordered photonic ball (Fig. 2.8C) combines the two spectral features: A dip in reflection, caused by the plasmon resonance, lowers the reflected light intensity in the lower-wavelength (blue/green) part of the spectrum but does not affect the higher-wavelength (red) region with the Bragg peak. Theoretical investigations reveal that the position of the gold nanoparticles within the ball strongly influences the purification effect: Positioning the particles within the ordered parts of the photonic structures increases color saturation whereas absorbers placed selectively in the disordered part decrease color saturation (Fig. 2.9). Simulations reveal an optimal absorber concentration of approximately 15% gold by volume (Fig. 2.9), when gold nanoparticles are placed exclusively in an idealized, ordered colloidal crystal.

The effect of nanoparticle addition becomes much more apparent in ensembles of photonic balls. Microscope images taken with identical exposure times, shown in Fig. 2.8 D and E, as well as a macroscopic photograph (Fig. 2.8F) reveal a whitish appearance of plain photonic balls due to unselective light scattering. The selective suppression of scattered light at lower wavelengths by absorption of light by the gold nanoparticles increases the contrast with little effect on the color intensity, resulting in a macroscopically more crisp color.

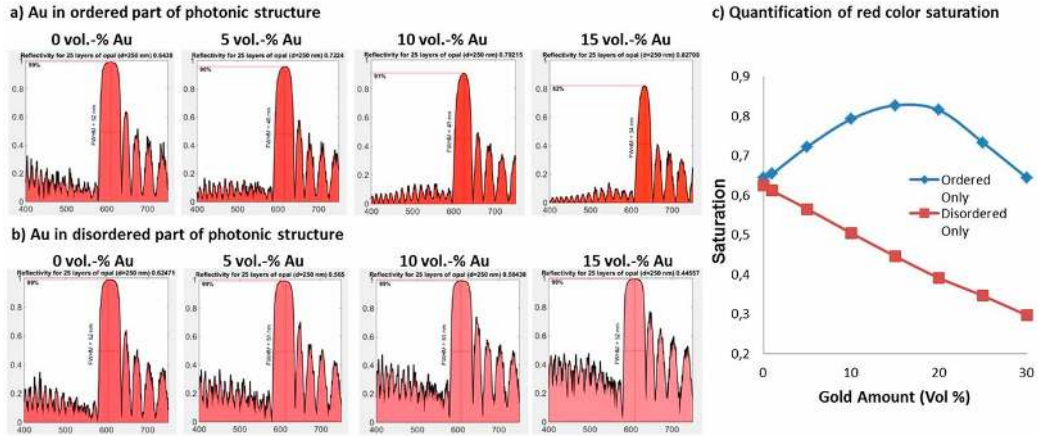


Figure 2.9: Effect of nanoparticle addition, concentration, and position within the photonic ball on the structural color, examined by one-dimensional (1D) transfer matrix simulations. (A and B) Effect of position and concentration of gold nanoparticles within the photonic structure. (A) Gold nanoparticles placed within the periodic structure; (B) gold nanoparticles placed in the disordered region underneath the periodic structure. (C) Dependence of the extracted red color saturation on the amount of gold nanoparticles added to the photonic structure.

### 2.3.4 Coloration Arising from Grating Diffraction

Photonic balls assembled from colloids with a diameter above 400 nm show color patterns that differ substantially from their analogs with smaller colloid sizes. Bright, multichromatic color patches appear at the outer regions of the photonic ball, showing color travel from blue to red with increasing distance from the center. This contrasts with the uniform coloration with colorless rims observed for photonic balls from colloids with sizes smaller than 400 nm. Previously, such color patterns in larger colloid assemblies were attributed to Bragg diffraction from different crystal planes [89] and grating diffraction effects [64]. Here, we present further evidence that Bragg diffraction from different crystal planes is an unlikely origin of color patterns and that diffraction-grating effects, arising from periodic arrangements of colloids at the surface of our micron-scale photonic balls, are responsible for the optical effect. A representative SEM image (ball diameter 15  $\mu\text{m}$ ), highlighting the ordered, close-packed arrangement of 400-nm colloids at the surface of the spherical superstructure,

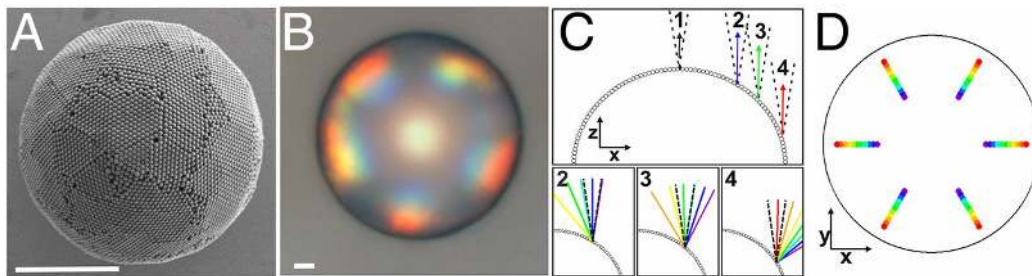


Figure 2.10: Observation of grating diffraction from the periodic surface structures of photonic balls. (A and B) SEM and optical micrographs of photonic balls prepared from 400-nm colloids. Diffraction-grating colors, arising from the periodic arrangements of the colloids at the ball's surface, are visible toward the rims of the ball. (Scale bars, 10  $\mu\text{m}$ .) (C) Model of the photonic ball's surface as a one-dimensional, curved diffraction grating and angular distribution of colors at different parts of the curved surface. Only light that is reflected back with a small range of angles (defined by the N.A. of the objective, indicated as a dotted cone in the image) close to normal to the surface from the grating is picked up by the objective lens and appears as color on the ball's surface. Because the incident angle increases from point 1 to point 4, light with increasing wavelengths is back-reflected into the lens. (D) Spatial distribution of the color predicted by the model, plotted on a circular surface mimicking the top-view image of the ball. The positions of color in the model and micrograph coincide.

is shown in Fig. 2.10A. A microscope image of a larger photonic ball ( $d = 100 \mu\text{m}$ ) from similar-sized colloids, shown in Fig. 2.10B, shows strong rainbow colors extending toward the rim. The lateral distribution of colors is not affected by the ball size (38) and can be seen in all samples with photonic ball diameters between  $15 \mu\text{m}$  and  $100 \mu\text{m}$  (Fig. 2.11). Clearly, the coloration is characterized by a gradual change from blue to red. Such a color travel is characteristic of grating diffraction, as described by the grating equation,  $m\lambda = d(\sin\theta_i + \sin\theta_m)$  (39). For each diffraction order  $m$ , the wavelength of constructive interference ( $\lambda$ ) changes with increasing angles of incident light ( $\theta_i$ ) and reflected light ( $\theta_m$ ) and with the distance ( $d$ ) between the individual scatterers. In contrast, were the colors to arise from Bragg diffraction at different crystal planes, few distinctive colors would be observed.

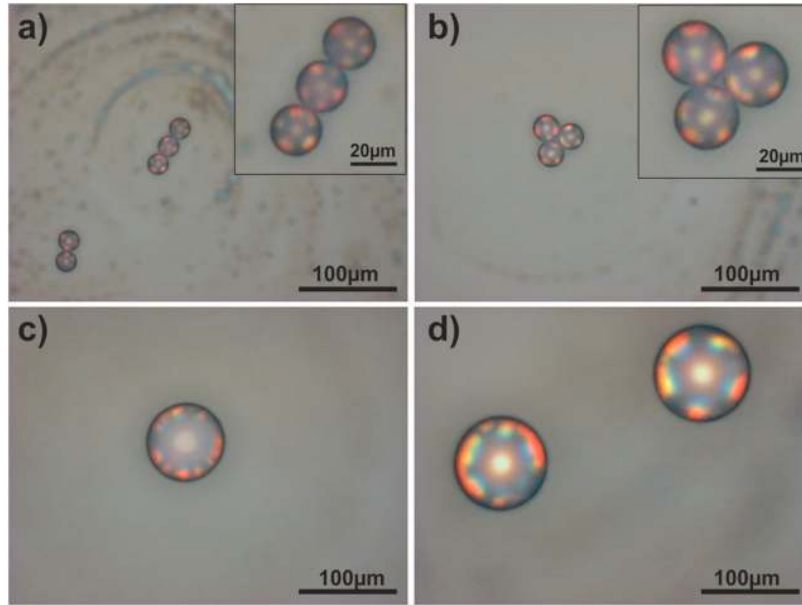


Figure 2.11: (A-D) Grating colors on differently sized photonic balls (A,  $15 \mu\text{m}$ ; B,  $30 \mu\text{m}$ ; C,  $60 \mu\text{m}$ ; D,  $90 \mu\text{m}$ ), all prepared from  $400\text{-nm}$  colloids. The position of the colors does not change with the size of the balls.

To resolve the origin of the coloration, we model the surface of a photonic ball as a regularly spaced arrangement of spheres on a hemispherical substrate, as shown in Fig. 2.10C. We assume that the colloids serve as a curved diffraction grating and calculate the angular distributions of constructively interfering waves for different



colors from the grating equation for different positions along the surface. Although the illumination is fixed from the top (normal to the substrate plane), the angle that the incoming light beam forms with the ball's surface differs at different positions as a result of the curved nature of the photonic ball. It is necessary to keep in mind that only light reflected in a small range of angles given by the numerical aperture around the surface normal (with respect to the substrate plane, not the ball surface) is collected by the microscope objective lens (indicated by dotted cones in Fig. 2.10C). Colors that are visible in the microscope image must therefore be reflected at angles within this cone. Because the angle of incident light with the curved surface changes with increasing distance from the center, so does the wavelength of light constructively interfering at angles that can be picked up by the objective lens. As we move the beam away from the center (Fig. 2.10 C, 1), grating diffraction predicts the shortest wavelength (blue light, modeled at 400 nm) to be picked up by the microscope first (Fig. 2.10 C, 2). With increasing distance from the center, the light arriving in the microscope changes gradually along the visible spectrum via green (550 nm, Fig. 2.10 C, 3) toward red (750 nm), which the model predicts to reach the objective lens only by reflection close to the rim (Fig. 2.10 C, 4).

To facilitate comparison between model and experimentally observed coloration, we present the results of the model in a top-view representation in Fig. 2.10D. Light of a given wavelength that is collected by the microscope objective at a given distance from the center is represented by a colored dot. We choose to illustrate the data obtained by the 1D model on the surface of a disk, representing the photonic ball as seen in a microscope, and assign a sixfold symmetry for the color map to depict the symmetry of a colloidal crystal. Image analysis, performed by measuring the distance of different color patches from the center of the photonic ball, reveals quantitative agreement on the color position between model and experiment (Table 2.2).

From the grating diffraction model, we expect a shift of the diffracted colors toward lower angles with larger periodicities. For the photonic balls, this translates into a shift of the rainbow-colored patches toward the center of the ball if the size of the constituent colloids is increased [64]. The theory also predicts the appearance of higher-diffraction orders at larger angles [100], which should be observed at locations

$d_{colloid}$ , nm	D.O.	$\lambda$ , nm	$r_{calc}/r_{ball}$	$r_{meas}/r_{ball}$	$\sigma$ , %
400	1	400	0.50	$0.44 \pm 0.06$	11.8
		550	0.69	$0.62 \pm 0.05$	10.0
		750	0.94	$0.91 \pm 0.04$	3.4
610	1	400	0.33	$0.30 \pm 0.03$	9.7
		550	0.451	$0.46 \pm 0.04$	3.0
		750	0.61	$0.69 \pm 0.05$	13.7
	2	400	0.66	$0.62 \pm 0.04$	5.0
		550	0.901	$0.81 \pm 0.05$	10.5
		750	1.00	$0.91 \pm 0.02$	9.5
1,060	1	400	0.19	$0.19 \pm 0.02$	0.6
		550	0.26	$0.30 \pm 0.03$	14.7
		750	0.35	$0.40 \pm 0.04$	14.6
	2	400	0.38	$0.41 \pm 0.04$	9.0
		550	0.52	$0.52 \pm 0.03$	0.5
		750	0.71	$0.63 \pm 0.03$	11.5
	3	400	0.57	$0.64 \pm 0.03$	13.3
		550	0.78	$0.77 \pm 0.03$	1.4
		750	1.00	$0.91 \pm 0.02$	9.5
610*	1	400	0.33	$0.27 \pm 0.01$	16.3
		550	0.45	$0.45 \pm 0.04$	0.7
		750	0.61	$0.73 \pm 0.03$	19.3
	2	400	0.66	$0.65 \pm 0.02$	1.4
		550	0.90	$0.81 \pm 0.05$	10.8
		750	1.00	$0.91 \pm 0.02$	9.5

\* Monolayer-on-microsphere architecture.

Table 2.2: Distance of selected colors represented as wavelengths  $\lambda$  (blue, 400 nm; green, 550 nm; red, 750 nm) from the ball center calculated from the diffraction-grating equation ( $r_{calc}$ ) and measured from microscopy images ( $r_{meas}$ ) as fractions of the ball radius  $r_{ball}$  for all visible diffraction orders (D.O.)

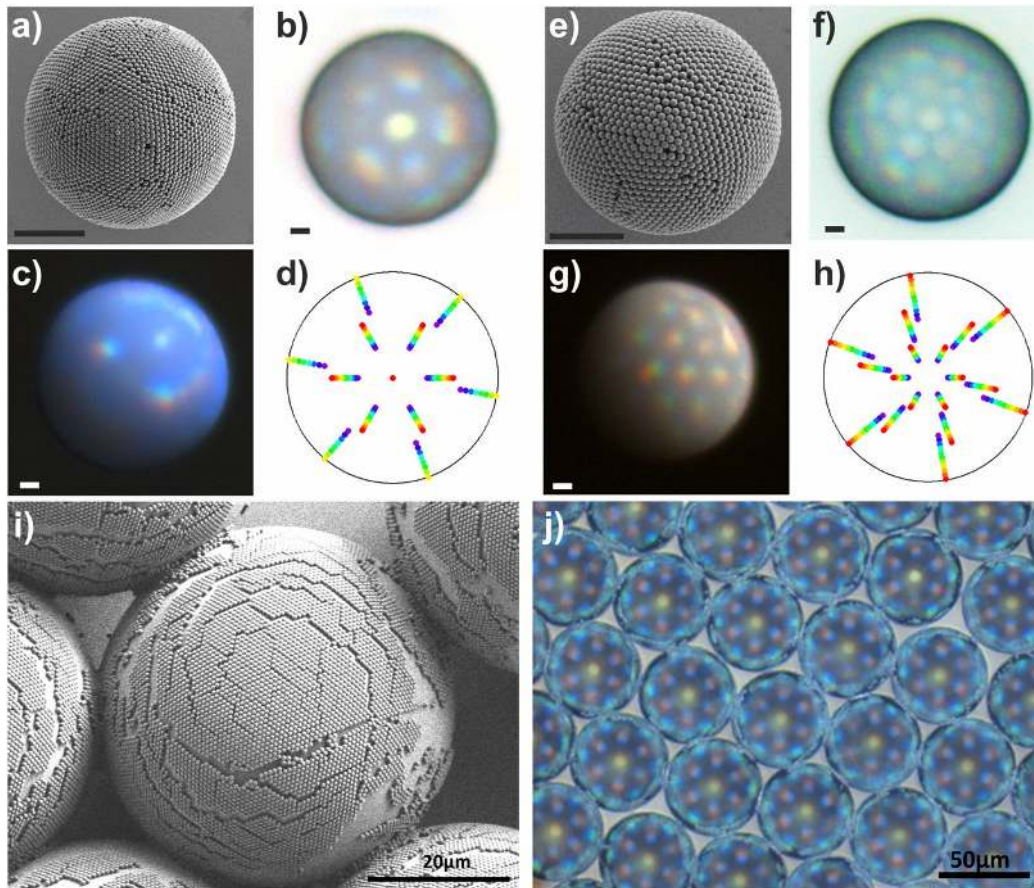


Figure 2.12: Multiple diffraction orders are observed in photonic balls from larger colloids. (A-D) SEM micrograph (A) and optical properties (B and C) of photonic balls prepared from 610-nm colloids. Two diffraction orders are visible as polychromatic spots in the optical micrographs in top (B) and side (C) illumination. The positions of the colors on the ball coincide with theoretical expectations based on a 1D model of grating diffraction on a curved surface (D). (E-H) SEM micrograph (E) and optical properties (F and G) of photonic balls prepared from 1,060-nm colloids. The optical micrographs in top (F) and side (G) illumination show three diffraction orders, the position of which coincides with theoretical expectations (H). The color patches assigned to the individual diffraction orders in the model are slightly offset for better visibility. (All scale bars, 10  $\mu\text{m}$ .) (I and J) SEM and optical micrographs of a close-packed monolayer of 610-nm colloids deposited onto a 50- $\mu\text{m}$  bead, mimicking the periodic arrangement of the colloids at the surface of a photonic ball. The monolayer-on-microbead architecture shows similar coloration, implying that grating diffraction is the origin of the color.

farther from the center of the ball. Indeed, both features are visible in the optical micrographs shown in Fig. 2.12. Photonic balls assembled from 610-nm colloids illuminated from the top and side are shown in Fig. 2.12 B and C, with a second grating order visible toward the rim of the structure. The position of the individual colors again coincides with the model quantitatively (Table 2.1 and Fig. 2.13). More remarkably, in photonic balls from 1,060-nm colloids (Fig. 2.12 F and G), three diffraction orders are visible and can be correlated with the model (Fig. 2.12, Table 2.2, and Fig. 2.13). The color patches assigned to the individual diffraction orders in the model (Fig. 2.12 D and H) are offset for better visibility.

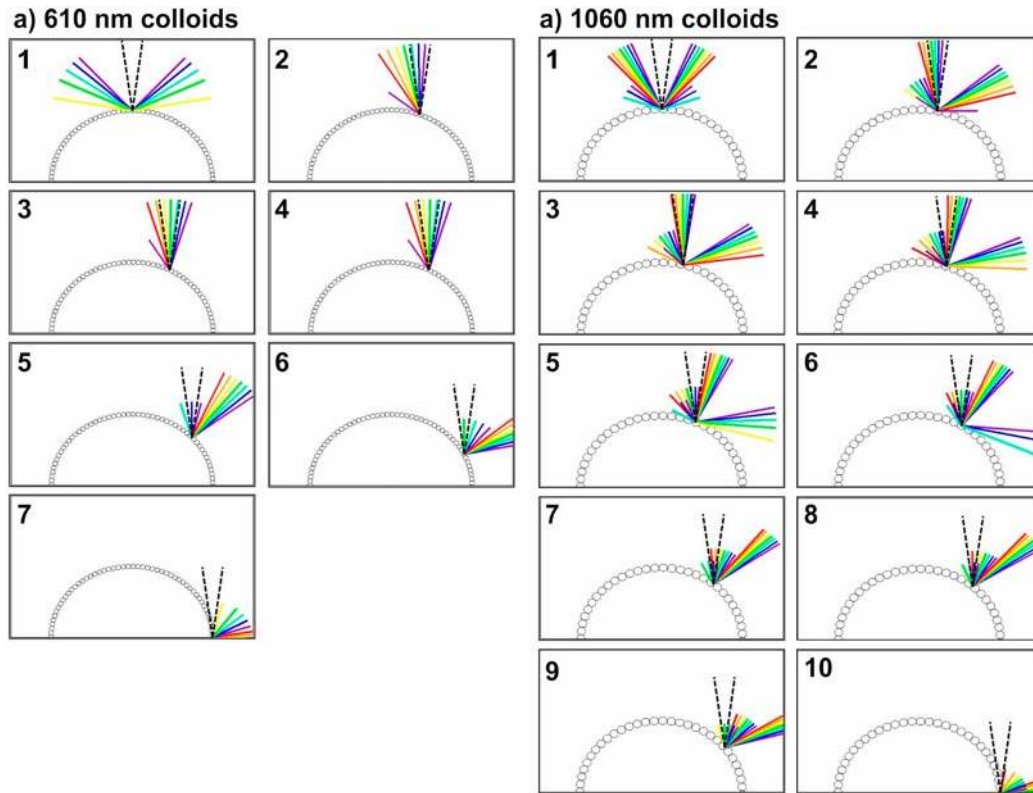


Figure 2.13: (A and B) Simulated grating diffraction from periodic arrangements of colloids at the balls' surfaces for 610-nm colloids (A) and 1,060-nm colloids (B). The plots in Fig. 2.12 show the colors collected by the objective lens (i.e., the colors in the dashed-stripe cone) as they appear with increasing distance from the ball center.

To unambiguously assign the observed color to grating diffraction and not Bragg

diffraction [64, 89], we coat large, 50- $\mu\text{m}$  polystyrene microbeads with a monolayer of 610-nm colloids—the same particles used to assemble the photonic balls in Fig. 2.10 A-C—following a protocol from the literature [101]. This monolayer-on-microbead architecture, shown in Fig. 2.12I, mimics the surface of a photonic ball but not its crystalline interior. Therefore, it cannot show Bragg diffraction. However, in the optical microscope image shown in Fig. 2.12J, we observe similar color patterns to those for the 3D photonic ball, with matching lateral position of the colors (Table 2.1). Therefore, we conclude that we indeed observe diffraction-grating effects on individual microscale photonic balls.

## 2.4 Conclusion

We explore how hierarchical order influences the properties of a self-assembled structure by studying individual microscale spherical colloidal crystals, known as photonic balls. Curvature, imposed on the colloidal crystal through the spherical confinement of an emulsion droplet, is the key element that alters the properties of the assembly. We provide a complete physical understanding of all optical effects observable in the prepared photonic balls and connect them to their structural origins.

FIB-assisted cross-sectioning indicates a layered morphology in the photonic balls that consists of radially ordered layers stacked from the interface toward the interior and a more disordered assembly towards the center. The layered structure gives rise to structural coloration by Bragg diffraction. When observed in a microscope, the presence of curvature creates uniform, angle-independent colors with a distinct colored ball area that reflects the numerical aperture of the objective. In contrast to flat opal films, the transmission spectra of a photonic ball are not the inversion of the reflection spectra but resemble a long-pass filter—again caused by reflection of light from the curved crystal. We control the degree of crystallinity via the size of the photonic balls and correlate the internal structure with the observed color intensity. Furthermore, we show that gold nanoparticles can be used as spectrally selective absorbers to suppress scattering, leading to a macroscopically brighter color. We present evidence that photonic balls assembled from colloids with a diameter of 400 nm or

larger show diffraction-grating coloration arising from the periodic arrangement of colloids at the surface of the particles.

We anticipate these results will lead to several research directions. First, additional insight into crystallization in spherical confinements, especially with respect to the crystallization mechanism and its kinetics, is needed to understand and control the assembly of colloids into spherical superstructures. Second, if the quality of the photonic balls can be reproducibly provided, they may serve as interesting materials for potential use as miniaturized photonic elements, for example as long-pass filters, diffraction gratings, or colorimetric sensors; in (optical) laboratory-on-a-chip applications; or as dispersible structural color pigments. Finally, the use of photonic balls as building blocks to create higher levels of hierarchy by self-assembly into more complex superstructures is a promising approach to further refine and exploit their rich optical properties.

## 2.5 Materials and Methods

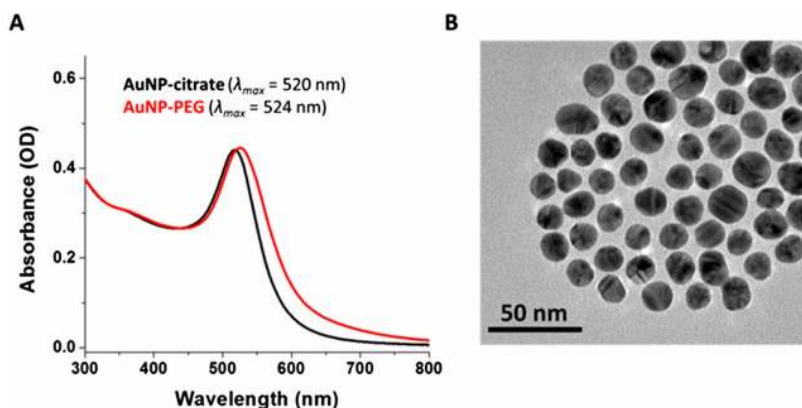


Figure 2.14: (A) UV-vis absorption spectra of citrate-capped AuNPs (black trace) and PEG-modified AuNPs (red trace) in water. (B) Representative TEM image of PEG-modified AuNPs.

Colloidal particles were synthesized by surfactant-free emulsion polymerization with acrylic acid as comonomer [102]. PEG-modified gold nanoparticles with a size of 12 nm were synthesized by reduction of sodium tetrachloroaurate (Fig. 2.14) as de-

scribed in the literature [103]. Microfluidic devices were prepared by soft lithography from masters prepared by photolithography [95]. Simulation of the optical properties was performed as a 1D transfer matrix method implemented in Matlab and effects of gold nanoparticles were included by adjusting the refractive index profile [104]. Optical spectra of individual photonic balls were measured through a microscope objective lens.

Styrene, acrylic acid, ammonium peroxodisulfate, sodium citrate, sodium tetrachloroaurate dihydrate, and methoxy-poly(ethylene glycol)-thiol (mPEG-SH) ( $M_r = 5,000$ ) were purchased from Sigma Aldrich and used as received. Poly(dimethylsiloxane) (PDMS) was purchased as a two-component system (Sylgard 184) from Dow Corning. The fluorinated oil HFE-7500 was purchased from 3M.

Electron microscopy was performed on a Zeiss Ultra Plus scanning electron microscope. Cross sections of photonic balls were performed on a Zeiss NVision 40 focused ion beam.

Polystyrene colloidal particles were synthesized by surfactant-free emulsion polymerization, using acrylic acid as comonomer and ammonium peroxodisulfate as an initiator following a recipe from the literature [102].

Polyethylene glycol (PEG) modified gold nanoparticles (AuNP-PEG) were synthesized from a solution of citrate-stabilized gold NPs, which were prepared according to a modified literature procedure [103]. Briefly, sodium citrate (50 mg, 0.17 mmol) was added to a refluxing, vigorously stirred solution of sodium tetrachloroaurate dihydrate (25 mg, 0.065 mmol) in 120 mL ultrapure water (MilliQ system). The mixture was stirred under reflux for 15 min before it was allowed to cool to room temperature. The initially yellow solution changed to deep red and was stored in a glass bottle protected from light. The AuNP formation was confirmed by UV-Vis spectroscopy ( $\lambda_{\max} \sim 520$  nm in water) and by TEM ( $D \sim 12$  nm). The calculated amount of AuNPs in the as-prepared solution was  $\sim 1.4 \times 10^{15}$  NPs and the concentration was  $\sim 16$  nM. Subsequently, mPEG-SH ( $M_r = 5,000$ ) was covalently grafted to the surface of the AuNP following a literature protocol (42). Briefly, 2 mL of mPEG-SH (25 mg/mL) solution was added dropwise to the vigorously stirred as-prepared AuNP solution. The solution was stirred for 3 h, allowing citrate ligands to exchange with

mPEG-SH (Fig. 2.14). PEG-modified particles were then centrifuged ( $20,800 \times g$ , 1 h) twice to remove excess mPEG-SH and concentrated to 12 mL to give an  $\sim 160$ -nm AuNP-PEG solution.

## 2.5.1 Microfluidic Fabrication of Photonic Balls

### Device Fabrication

Microfluidic devices were fabricated by soft lithography. Negative photoresist SU-8 (MicroChem, Newton, MA, USA) was spin coated onto a clean silicon wafer to a thickness of 10  $\mu\text{m}$ , 25  $\mu\text{m}$ , or 50  $\mu\text{m}$  and patterned by UV exposure through a transparency photomask (CAD/Art Service). After developing the microstructure, a mixture of Sylgard 184 PDMS (Dow Corning) and curing agent (ratio 10:1) was poured onto the pattern, degassed, and cured overnight at 65  $^{\circ}\text{C}$ . The PDMS molds were peeled off the master and the channel inlets and outlets were made by using a 0.75-mm diameter biopsy punch (Harris Uni-Core; Ted Pella). The PDMS replicas were bonded to a glass slide after oxygen-plasma activation of both surfaces and cured for 1 h at 65  $^{\circ}\text{C}$  to enhance bonding. To avoid wetting of the channels by the inner phase, the devices were treated with Aquapel (PPG Industries) by flushing the channels with the solution as received, air drying, and heating to 65  $^{\circ}\text{C}$  for 1 h.

### Drop Generation

To fabricate droplets of an aqueous colloidal dispersion, the dispersion was loaded into polycarbonate syringes (BD Luer-Lok Disposable Syringes). A mixture of 0.1 wt% perfluoropolypropyleneglycol-block-polyethyleneglycol-block-perfluoropolypropyleneglycol surfactant (purchased from RainDance Technologies; Dolomite Pico Surf) in perfluorinated carbon oil (3M Novec 7500 Engineered Fluid) was used as outer phase. PE/2 tubing with an outer diameter of 1.09 mm and an inner diameter of 0.38 mm (Scientific Commodities) was used to connect the channel inlets with the syringes. Flow rates were controlled by syringe pumps (PHD 2000; Harvard Apparatus). The droplet generation was performed in a customized cross-junction



device and monitored with an inverted microscope. The flow rates were 100  $\mu\text{L}/\text{h}$  for the inner (colloidal dispersion) phase and 200  $\mu\text{L}/\text{h}$  for the outer (fluorocarbon oil) phase.

### **Assembly of Photonic Balls**

The emulsion droplets of the colloidal dispersion in oil were collected in glass vials surface functionalized with 1H,1H,2H,2H -(tridecafluorooctyl)- trichlorosilane (Gelest) via vapor phase deposition at reduced pressure. Before silanization, the vials were activated by oxygen plasma (Diener Electronics; model femto) for 10 min. The vials with the emulsion were placed in an oven at 45 °C to allow the water to evaporate and the photonic balls to self-assemble. Depending on the amount of droplets within the vial, the drying time varied between a few minutes and several hours.

### **2.5.2 Optical Characterization**

Individual photonic balls were spectrally analyzed by illuminating them through a microscope objective (Olympus, 50 $\times$  objective lens, 0.5 N.A.). Reflected light is channeled through the same objective and an additional tube lens before it is collected with an optical fiber (Ocean Optics; 100- $\mu\text{m}$  core) and analyzed with a grating spectrometer (Ocean Optics; Maya Pro) controlled via the software IGOR. This procedure allows us to collect reflected light from an area of a few micrometers, small enough to probe the color of the individual photonic balls.

### **2.5.3 Computer Simulations and Theoretical Models**

A 1D transfer matrix method was implemented in Matlab, using laterally averaged permittivity values for an opal structure as shown in Fig. 2.5. Reflectance values were calculated for each wavelength, using this method for the various colloid sizes shown in the main text. For the diffraction-grating models, the angular location of each color/diffraction order combination was calculated using the grating equation with the assumption that at a given position along the photonic ball, the diffraction

can be modeled as that from an infinite grating with periodicity equal to the diameter of the colloids and orientation given by the tangent to the ball at that location.

Simulations were used to investigate how the concentration and position of nanoparticle absorbers affects the color of photonic balls (Fig. 2.9). The simulations are performed using 25 ordered layers with a refractive index profile matching that of a colloidal crystal (compare with Fig. 2.5) and a random refractive index material underneath the multilayer structure, approximating the more disordered interior regions. Gold nanoparticles were simulated by calculating the effective refractive index of the air/gold nanoparticle composite medium used in the transfer matrix calculations, using a method from the literature (43). The resulting macroscopic color is indicated by the color underneath the simulated reflection curve. The color intensity is calculated by using the CIE 1931 (Commission Internationale de l’Eclairage; International Commission on Illumination) tristimulus color-matching functions to convert the spectra into RGB (red, green, blue) values and then converting to the HSV (hue, saturation, value) color space and plotting the saturation value.

Positioning the particles in the ordered layers results in color purification because the decrease in reflected light intensity primarily occurs in the high-energy part of the spectrum (Fig. 2.9A). With increasing amount of gold nanoparticles, the total absorption increases and increasingly also suppresses the Bragg peak due to the nonzero absorption of gold nanoparticles in the red part of the spectrum. Note that absorption is nevertheless more pronounced in the blue/green part of the spectrum. Adding nanoparticles to the disordered part does not increase saturation (Fig. 2.9B). On the contrary, scattering is increased due to the increase in refractive index in the randomized matrix. A maximum in color saturation exists (Fig. 2.9C) because of the balance between increased absorption of wavelengths off the Bragg reflection peak and increasing total absorption. The optimal scenario for color purification is a concentration of around 15 vol% of gold nanoparticles placed in the ordered layers of the photonic structures. Because the simulation assumes a uniform distribution of gold nanoparticles within the photonic ball and perfect ordering of the reflective layers, this number may differ from experimental results.

Page intentionally left blank

## Chapter 3

# Combining Bottom-Up Self-Assembly with Top-Down Microfabrication to Create Hierarchical Inverse Opals with High Structural Order

In this chapter we discuss another example of a colloidal photonic crystal as introduced in Chapter 1. Here, the addition of a photolithographic step to the fabrication of the structurally colored material allows for interesting geometries and patterns to be created as well as an addition of hierarchical structuration to the material in the form of a diffraction grating created out of inverse opal. This hierarchy allows for the creation of an optical material having properties of both a surface diffraction grating and an inverse opal simultaneously. More examples of this kind of combination effect are discussed beginning with Chapter 4 as an introduction.

## **3.1 Overview**

### **3.1.1 Abstract**

Colloidal particles can assemble into ordered crystals, creating periodically structured materials at the nanoscale without relying on expensive equipment. The combination of small size and high order leads to strong interaction with visible light, which induces macroscopic, iridescent structural coloration. To increase the complexity and functionality, it is important to control the organization of such materials in hierarchical structures with high degrees of order spanning multiple length scales. Here, a bottom-up assembly of polystyrene particles in the presence of a silica sol-gel precursor material (tetraethylorthosilicate, TEOS), which creates crack-free inverse opal films with high positional order and uniform crystal alignment along the (110) crystal plane, is combined with top-down microfabrication techniques. Micrometer scale hierarchical superstructures having a highly regular internal nanostructure with precisely controlled crystal orientation and wall profiles are produced. The ability to combine structural order at the nano- and microscale enables the fabrication of materials with complex optical properties resulting from light-matter interactions at different length scales. As an example, a hierarchical diffraction grating, which combines Bragg reflection arising from the nanoscale periodicity of the inverse opal crystal with grating diffraction resulting from a micrometer scale periodicity, is demonstrated.

## **3.2 Introduction**

Colloidal self-assembly is widely appreciated as an experimentally simple, low-tech process to create well-defined nanostructures. [5, 105, 106] Owing to their high order and periodicity at a length scale comparable to the wavelengths contained in the optical spectrum, colloidal crystals can interact strongly with visible light. The periodic modulation of the refractive index in opaline materials gives rise to a photonic bandgap, which results in high intensities of reflected light in the wavelength range corresponding to the range of frequencies within the bandgap. The position of the

bandgap can be varied, for example, by changing the size of the colloidal particles used in the crystal's creation or by altering composition or shape. [97, 107, 108] Moreover, colloidal crystals can be used as sacrificial templates to fabricate inverse opals. Like their direct opal analogues, inverse opals possess interesting optical properties and have been extensively used in photonic applications. [97, 107–110] The well-defined, interconnected porosity at the nanoscale further allows for applications in various fields, including wetting, [44, 111–113] (photo)catalysis, [114, 115] cell culturing, [116] photovoltaics, [117, 118] energy storage, [119–121] and sensing. [108, 111, 122, 123] Most of these applications simplistically utilize inverse opals as thin films.

Precise spatial control of colloidal assemblies in hierarchical structures spanning multiple length scales can enable more advanced applications, for example, multiplexed and miniaturized sensing devices, [91] pixelated arrays of structural color units, [67, 124, 125] miniaturized photonic elements, [126] or microstructured electrodes with high surface area. [120] Furthermore, a hierarchical design may enable us to alter or to enhance the optical properties of such self-assembled structures by combination of the photonic bandgap properties with reflective, scattering or dispersive elements, with a potential to mimic complex structural colors found in nature. [74, 127]

The assembly of hierarchical colloidal crystal structures can be controlled from the bottom up by pre patterning the substrate with a desired topography. [128–134] If the topography is chosen to match the symmetry of the colloidal crystal, highly ordered, hierarchical structures result. [131, 134, 135] If the imposed topography interferes with the overall lattice orientation, the crystal growth is frustrated, leading to disorder and cracks. [134] As a consequence, the quality of the crystal is significantly reduced.

If the order in the colloidal assembly is to be maintained for any desired structural feature, the assembly process must be separated from the patterning. This can be achieved by using top-down, microfabrication techniques such as photolithography, [66, 67, 136, 137] microcontact printing, imprinting and stamping, [68, 125, 138] or inkjet printing. [139] In these approaches, defects in the crystal structures can be created by curvature or patterning protocols, be inherited from the assembly process or mechanical treatment and include polycrystallinity arising from different nucleation

sites, cracks and over- or underfilled pores when replicated into inverse structures.

Here, we use a coassembly method to crystallize polymer colloids in the presence of tetraethylorthosilicate (TEOS), which has been shown to result in well ordered inverse opal thin films with open and interconnected pores and low density of cracks at square centimeter dimensions and beyond. [140] Most remarkably, the assembled structures show single crystal orientation throughout the substrate arising from a preferred growth along the (110) crystal plane. [134, 140] To preserve the order, we apply photolithography and reactive ion beam etching in a post-assembly step to fabricate arbitrarily shaped hierarchical superstructures and patterns that possess an equally high degree of order and crystal orientation.

### 3.3 Results and Discussion

Figure 3.1A schematically shows the fabrication of the hierarchical inverse opal superstructure. We crystallize polystyrene colloidal particles by evaporative assembly in the presence of a silica sol-gel precursor (TEOS). After calcination at 500 °C, we obtain a highly ordered, iridescent inverse opal thin film with oriented crystallinity throughout the substrate. [134, 140] We then infuse the porous matrix with a photoresist that has a refractive index closely matching that of the surrounding silica. The resulting infiltration of the pores by the resist is indicated by the disappearance of the iridescence. [111, 141] The resist-filled inverse opal is UV-exposed through a mask with the desired structural pattern. Since the pores are all filled with the index-matched photoresist, scattering of UV-light is prevented, leading to high quality photolithographic patterns without blurring of features. We thus create a protective photoresist layer covering selected parts of the substrate. Anisotropic reactive ion beam etching is then used to mill into the substrate, removing the inverse opal structures at all unprotected areas. In a final calcination step, photoresist residues are removed, yielding a pattern of highly ordered, inverse opal superstructures.

The etching depth can be precisely controlled via the etching time, allowing us to remove individual layers of the inverse opal (Figure 3.1B). The minimum obtainable feature sizes are defined by the resolution of photolithography and the reactive ion

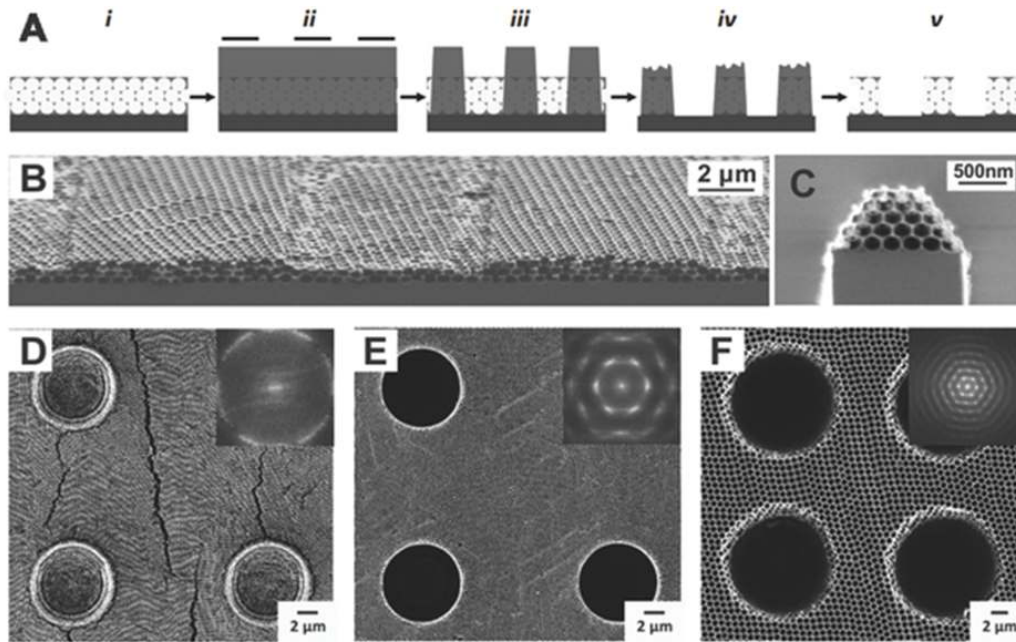


Figure 3.1: Decoupling the crystal formation from patterning creates hierarchical structures with uncompromised order. A) Schematic illustration of superstructure fabrication. A highly ordered inverse opal (i) is infiltrated with photoresist and exposed to UV light to create a pattern (ii). The inverse opal/photoresist hybrid structure is developed, removing the photoresist from the porous structure at the exposed substrate areas (iii). Anisotropic reactive ion beam etching is used to remove all unprotected parts of the opal (iv). After calcination to remove photoresist, the inverse opal superstructure is formed (v). B) Patterned inverse opal with a step size of one colloidal layer, demonstrating high vertical resolution. C) Side-view image of an inverse opal line pattern, showing vertical etching along the (111) plane of the crystal. D-F) Comparison of the order in hierarchical structures obtained by assembling a direct opal on a lithographically patterned substrate with topography (D), co-assembling colloids in the presence of TEOS on a similarly patterned substrate to create a hierarchical inverse opal (E), and by decoupling the crystal formation from the lithographic patterning step, following the procedures described in the current paper (F). The crystal order is completely preserved if the patterning step is applied after crystal formation.



beam etching step: for straight line patterns, we find a selective vertical etching along the (111) cleavage plane of the substrate to produce a characteristic trapezoidal wall profile (Figure 3.1C), which we attribute to the minimal amount of mass that needs to be removed along that plane. This etching characteristic leads to 60° vertical incline at the edges, giving us a reproducible three-dimensional morphology of the patterned inverse opal. Simple geometric considerations (Supporting Information) allow us to determine the lateral resolution of the hierarchical inverse opal feature  $x$  as a function of the inverse opal layer thickness  $h$  and the lateral size of the photoresist pattern used as a mask  $x(\text{lithography})$ :

$$x(h) = x(\text{lithography}) + \frac{2}{\sqrt{3}}h \quad (3.1)$$

Figure 3.1D-F compares the degree of order in hierarchical colloidal assemblies prepared by self-assembling direct (Figure 3.1D) and inverse opals (Figure 3.1E) on substrates with a topography, and by top-down patterning of prefabricated inverse opals (Figure 3.1F). As we have observed previously, the co-assembly of colloids with TEOS increases long-range order and eliminates crack formation (Figure 3.1E) as compared to a direct assembly of colloids (Figure 3.1D). [134] However, since the geometry of the topography does not match the crystal structure, the co-assembled crystal shown in Figure 1E shows frustrated crystallization, creating disorder around the obstacle. In contrast, the high order and orientation of the crystal is completely retained when assembly and patterning are separated (Figure 3.1F).

The preferential growth of the co-assembled colloidal crystal film along the (110) plane generates inverse opal films with high crystal alignment, [134,140] which can be transferred into the hierarchical pattern by aligning the photolithography mask at a controlled angle (e.g. parallel or perpendicular to the growth direction of the inverse opal crystal) to create identical macroscopic patterns with various crystallographic orientations of the constituent self-assembled photonic crystal. Figure 3.2 shows slabs of inverse opals with crystal orientations along the (110) plane and (100) plane, respectively. The insets show the orientation of the inverse opal film as grown on the substrate and the resulting orientation of the crystal within the pattern. The Fourier

transformations, showing undisturbed hexagonal patterns, indicate high order and crystal alignments.

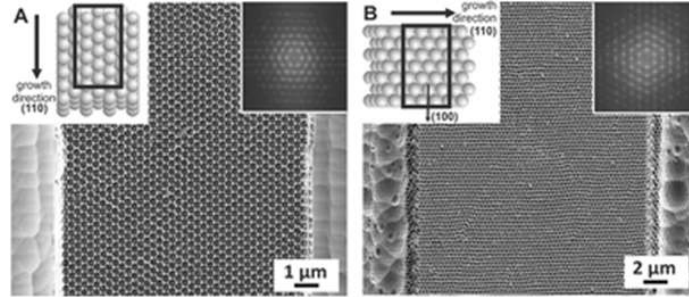


Figure 3.2: Control of crystal orientation within the superstructure. The inverse opal thin films preferentially grow along the (110) direction (see insets). Any arbitrary orientation of the constituent photonic crystal within the final hierarchical pattern can be achieved by simple rotation of the mask relative to the orientation of the substrate. A) When a pattern (black box) is aligned along the growth direction, hierarchical structures with a (110) orientation of the inverse opal crystal within the superstructure form; B) Aligning the pattern perpendicular to the growth direction yields hierarchical structures with a (100) orientation. High order and uniform orientation are evident from the FFT images shown as insets.

The process allows the creation of complex, arbitrarily shaped hierarchical structures with high accuracy and resolution while maintaining order and orientation of the inverse opal crystal, which we demonstrate by a micrometer scale reproduction of a world map (Figure 3.3A). The map, with its complex shape, demonstrates our ability to pattern arbitrary features with multiple length scales-including adjacent concave and convex features. Moiré patterns, indicative of high crystal order, [142] are visible throughout the image. Order and crystal alignment throughout the complete structure is further highlighted in high magnification images of selected regions (Figure 3.3B-D), which all show uniform crystal alignment resulting from the single crystal orientation of the underlying coassembled inverse opal. This uniform alignment of the crystal is evidenced by Fourier transform analyses shown as insets. The specific crystallographic orientation of the inverse opal single crystal in the pattern can be altered by rotation of the imposed photolithographic mask with respect to the substrate (compare, for example, two perpendicular orientations of the line pattern in

the [110] and [100] directions in Figure 3.2). The lateral resolution achieved in some parts of the map is below 1  $\mu\text{m}$ -only a few colloidal particles in width.

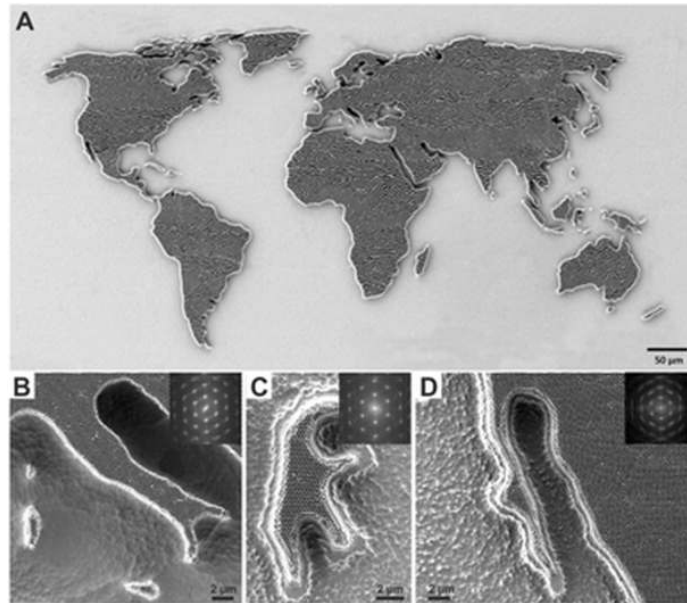


Figure 3.3: Fabrication of single crystalline, complex patterns with hierarchical features spanning multiple length scales. A) SEM image of a micrometer scale inverse opal pattern in the shape of the world map. The Moiré patterns visible throughout the image indicate high order. B-E) Close-up SEM images and Fourier transformation analyses (insets) of different parts of the world map. The images show (B) Italy, (C) Sulawesi, and (D) the Baja California peninsula. Order and uniform crystal orientation in images are evident from Fourier transformation (insets).

Since the order of the colloidal assembly is retained in the generated hierarchical structures, they also maintain their distinctive structural coloration. The wavelength of constructive interference changes with the incident angle, giving the inverse opals their vivid iridescence. This color shift allows us to create complex, micrometer scale structures with dynamic coloration (Figure 3.4). We design arbitrary, micrometer scale "artworks" and illuminate the structure under a microscope. With an illumination normal to the surface, the structures show green (top, 250 nm colloids used as template) and red colors (middle, bottom, 320 nm colloids) depending on the size of the colloids (Figure 3.4B). The variation of color in the top image of Figure 3.4B arises from changes in crystal thickness. [111] As expected, the observed color shifts into

the blue part of the spectrum with increasing light incidence angles (Figure 3.4C). Additional levels of complexity may be introduced to the system by tailoring liquid infiltration by means locally changing the surface chemistry [141] or locally modifying the color by changing the pore sizes, for example using atomic layer deposition.

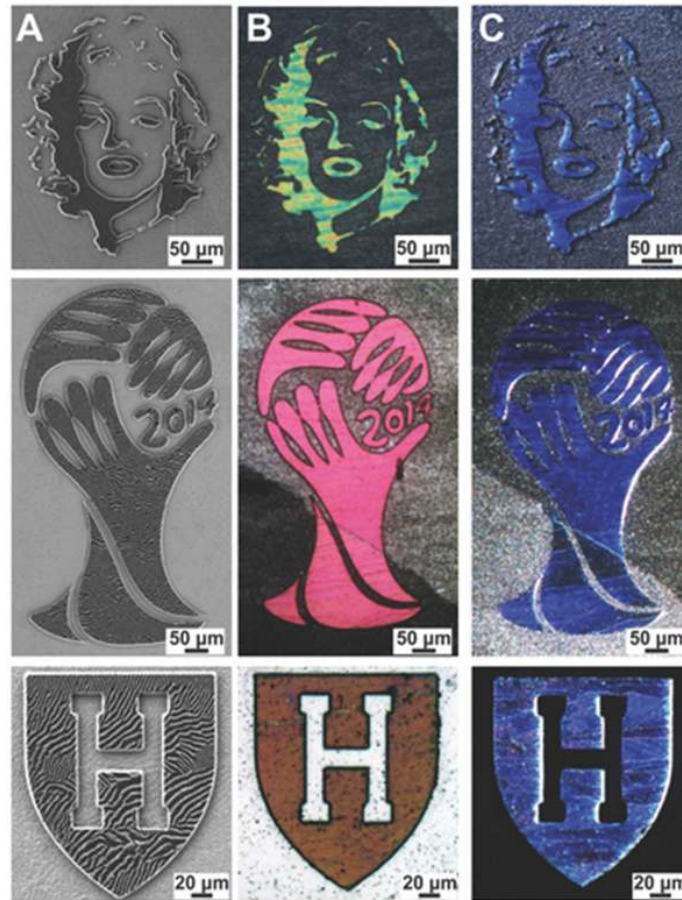


Figure 3.4: Structural color imaging at micrometer scale. A) SEM images of hierarchical inverse opal structures; microscopy images taken (B) with illumination normal and (C) off-normal to the surface. The images show real, dynamic structural color that blue-shifts with increasing illumination angle.

The hierarchical microfabrication allows the combination of photonic effects occurring on disparate length scales. For example, we can create a hierarchical diffraction grating by patterning inverse opals into periodic stripes (Figure 3.5A,B). A diffraction grating creates an angular dispersion of light (with a wavelength  $\lambda$ ) de-

pendent on the illumination conditions (angle of incident light  $\theta_i$  and diffracted light  $\theta_d$ ) and the periodicity  $d$  of the grating as described by the grating equation: [100]

$$m\lambda = d(\sin\theta_i + \sin\theta_d) \quad (3.2)$$

We investigate the optical properties of our hierarchical diffraction grating by variable angle spectroscopy, measuring reflection spectra as a function of observation angle over a wide range of angles. Figure 3.5C,D shows the reflected light intensity for all measured wavelengths and diffraction angles (plotted as  $\sin(\theta)$  for better comparison with the grating equation). The data are plotted as an image with vertical columns corresponding to spectra measured at each detection angle and rows corresponding to the wavelengths detected by the spectrometer. Intensity of the reflected light is color-coded with black signifying low and yellow high intensities. The incidence angles shown are  $0^\circ$  and  $30^\circ$  for Figure 3.5C,D. Multiple diffraction orders, arising from the microscale periodicity of the superstructure are visible as straight lines in the plots.

The distribution of light intensity in the individual diffraction orders shows the fingerprint of the second optical element present in the hierarchical material—the inverse opal. The photonic bandgap, arising from the nanoscale periodicity of the colloidal crystal, is encoded in all individual diffraction orders and, as expected, blue-shifts with increasing angle of incident light. In Figure 3.5C, enhanced reflected intensity is detected around 500 nm for all diffraction orders. This signature of the Bragg diffraction peak shifts toward 420 nm when the angle of incident light is changed (Figure 3.5D). Figure 3.5E,F presents the wavelength-dependent intensity, extracted along the first five positive diffraction orders for both incident angles. Again, the incident angle-sensitive signature of the Bragg diffraction peak is clearly visible at 500 nm ( $0^\circ$  incident light, Figure 3.5E) and 420 nm ( $30^\circ$  incident light, Figure 3.5F) in all diffraction orders.

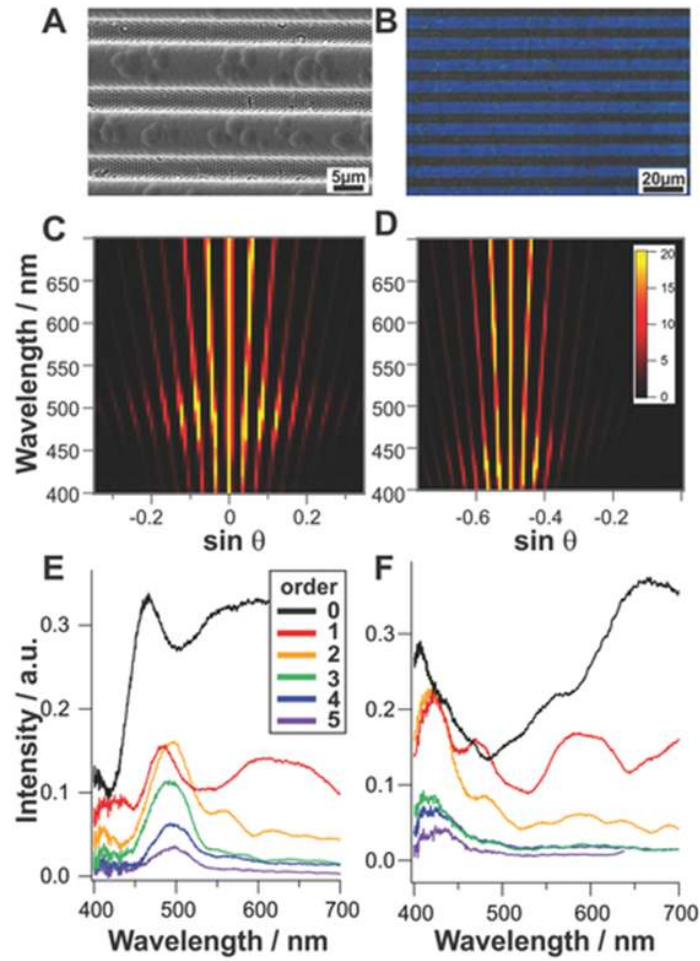


Figure 3.5: Multiple optical properties arise from periodicities at different length scales in hierarchical inverse opal structures. A) SEM and B) optical microscope image of periodically spaced inverse opal slabs serving as a hierarchical diffraction gratings. C,D) Optical properties of the inverse opal diffraction grating represented in two dimensions by plotting the sine of the reflected light versus the wavelength. Each vertical line represents an individual spectrum. The spectra were taken for (C) incident light normal to the surface and (D) at an angle of  $30^\circ$  relative to the surface normal. The hierarchical structure shows multiple diffraction orders, visible as straight lines in the figure. E,F) Wavelength-dependent intensity, taken along the first five diffraction orders. As a result of the inverse opal structure, the light intensity in these individual orders is modulated and shows enhanced intensity at the Bragg diffraction peak, which shifts with increasing incident light angle.

## **3.4 Conclusions**

In conclusion, we have exploited the high order and single crystal orientation found in inverse opals assembled from polymeric colloids in the presence of TEOS to create superstructures by a combination of photolithography and reactive ion beam etching of the pre-assembled, crystallographically oriented inverse opal films. The uniform crystal orientation across the entire patterned area remains unaltered in the produced, highly ordered hierarchical structures and can be controlled by orienting the lithographic pattern at an arbitrary angle relative to the underlying single crystal. This enables us to align different crystal planes within the individual hierarchical elements. In addition to the resolution of the lithographic procedure, the minimal structural feature width (coupled with the feature height) is limited by the anisotropic trapezoidal etch mechanism that follows (111) cleavage planes of the crystal. These hierarchical patterns show angular-dependent structural coloration which we exploit to create iridescent real color images at a micrometer scale. Furthermore, the control of order and periodicity at multiple length scales allows creating materials that combine multiple optical properties. We demonstrate such complex optical materials by encoding the photonic bandgap properties within the individual diffraction orders of a diffraction grating. We believe that the controlled fabrication of high-quality inverse opal superstructures with full control of feature sizes, controlled crystal orientation, and minimum defect density will open pathways to harvest the intriguing properties of inverse opals in advanced applications and devices—from miniaturized sensing architectures to a sophisticated tailoring of light-matter interactions in photonics or phononics. Especially, we anticipate the technology to serve as an experimentally simple platform to create multi-scale optical materials to help understand and mimic the vivid coloration of hierarchical structures occurring in nature.

## **3.5 Methods**

### **3.5.1 Preparation of Inverse Opals**

Polystyrene (PS) colloids were synthesized using a surfactant-free emulsion polymerization following a protocol from literature. [102] Inverse opals were synthesized by a coassembly process with TEOS. [140] PS colloids were added to 20 mL of water and adjusted to 0.1% solid content. 150  $\mu$ L of prehydrolyzed TEOS solution (1:1:1.5 by volume of TEOS:0.1 M HCl:ethanol, stirred for 1 h at room temperature) was added and the mixture was sonicated for 5 min. A cleaned silicon wafer (exposed to acid piranha for 45 min and extensively rinsed with water) was vertically suspended in the vial and placed inside the oven for several days for the solvent to evaporate completely. A vibration-free oven set to 65  $^{\circ}$ C was used for the coassembly process. After complete solvent evaporation, a single-domain opal film with silicon dioxide filling the interstitials was left on the wafer substrate. Calcination for 5 h at 500  $^{\circ}$ C with a defined heating ramp of 2  $^{\circ}$ C min<sup>-1</sup> and a cooling time to room temperature in 3 h resulted in high quality inverse opal film. Deionized water was used from a Milli-Q system, ethanol was purchased from Koptec, and all other chemicals were purchased from Sigma-Aldrich.

### **3.5.2 Photolithography on Inverse Opal Film**

Photolithography was performed in an ISO class 5 clean room at CNS, Harvard. Inverse opal films were cleaned with acetone and isopropyl alcohol (IPA) on a Headway Research spin coater at 3000 rpm for 10 s each. Complete solvent evaporation was performed on a Torrey Pines hot plate at 180  $^{\circ}$ C for 5 min. Samples were then pre-coated with hexamethyl disilazane (HMDS) at 3000 rpm for 60 s and soft baked at 110  $^{\circ}$ C for 60 s. Thereafter, Shipley S1818 positive photoresist was spin coated on the sample at 2000 rpm for 45 s and hard baked at 110  $^{\circ}$ C for 60 s, giving a protective layer thickness of 2  $\mu$ m. Chrome masks were designed with AutoCAD 2014 and printed using a Heidelberg DWL 66 mask writer. Using a Suss MJB4 mask aligner, soft-contact (1.3 bar) was established between the chrome mask and



the coated sample. Exposure time was calculated by dividing the exposure dose E0 (180 mJ  $cm^{-2}$  for S1818) by the h-line intensity (405 nm) of the MJB4 mask aligner. Standard exposure time was 4.5 s. For feature sizes smaller than 6  $\mu m$ , additional 0.1 s were added to the calculated exposure time for every 1  $\mu m$  decrease in size. After exposure, samples were hard baked at 110  $^{\circ}C$  for 60 s and developed with Microposit MF CD-26 developer. Developing steps were first 50 s in CD-26, followed by 10 s in fresh CD-26 and 15 s in DI water. Samples were blow dried with nitrogen.

### **3.5.3 Reactive Ion Etching**

Anisotropic reactive ion etching was performed on a STS induced coupled plasma reactor (STS ICP RIE) with a standard recipe for silicon dioxides etch. The plasma reactor was first cleaned with oxygen plasma for 20 min, followed by a 10 min stabilization cycle of the etch program. 10 sccm  $C_4F_8$ , 10 sccm SF6 and 3 sccm H2 were used with 900 W coil power, 100 W platen power at 7 mTorr and 38  $^{\circ}C$ . Etch rates were determined by a Veeco Dektak profilometer. We found etch rates of 0.43  $\mu m$  min $^{-1}$  for inverse opal and 0.35  $\mu m$  min $^{-1}$  for photoresist, giving an etching ratio of 1:1.23 resist to inverse opal. Samples were rinsed with ethanol and IPA. To remove the protective photoresist layer, the samples were calcined for 5 h at 500  $^{\circ}C$  with a defined heating ramp of 2  $^{\circ}C$  min $^{-1}$  and a 3 h cooling time back to room temperature.

### **3.5.4 Imaging and Characterization**

Scanning electron microscopy (SEM) was performed on a Zeiss Ultra Plus field emission microscope. ImageJ was used for subsequent image analysis. An Ocean Optics DH-2000 UV-vis-NIR light source was used for the variable angle spectrometry measurements to illuminate a small spot (<1 mm) on the sample at a given incidence angle. Individual spectra were collected at half degree increments for  $-75^{\circ}$  to  $+75^{\circ}$  relative to the sample normal for each angle of illumination and spectrally analyzed using an Ocean Optics Maya Pro 2000 spectrometer.

# Chapter 4

## Emerging Optical Properties from the Combination of Simple Optical Effects

In this chapter we give a more robust overview of the field introduced in Chapter 3, discussing many types of structurally colored materials created utilizing hierarchy to allow for combination optical effects to be observed. Expanding on this, we further discuss the addition of absorption into structurally colored materials—both in a structured and an unstructured way—to modify the optical properties of the material (as discussed in Chapter 1) and create new types of photonic effects. Finally, we briefly discuss the use of plasmonic materials (whether nanoparticles or lithographically defined meta-materials) to create colored materials with novel effects.

### 4.1 Introduction

Structurally colored materials (SCMs) are prized for their absence of photo-bleaching and wide range of optical properties not obtainable in bulk materials. [75,79] They can also create special color effects that are not obtainable in standard pigments such as iridescence or environmentally-induced color change. [45,143] Natural organisms have optimized their color-producing features through millions of years

of evolution, utilizing SCMs, pigments, or combinations of the two to achieve their desired appearance. [74] Using such organisms as inspiration, scientists have learned how to create and optimize SCMs for a variety of purposes; the use of bio-inspired, rather than bio-mimetic [106], approaches to this field have yielded materials which capture the essence of the color-producing elements in natural organisms by distilling the structures down to their key components: order/disorder, hierarchy, and absorption/scattering.

The use of order and disorder in photonic crystals allows for control over the amount of angular variation or color travel, with more disordered materials having less angular dependence of their reflected color due to the lack of coherent crystal planes within the photonic crystal. Scientists have gained a fundamental understanding of the interrelationship of structural arrangements and the resulting coloration of a material and have used this understanding to fabricate structured materials with controlled order or disorder at nanoscale length scales. [4]

Hierarchy is a common theme in biological materials, whether as a necessity for multifunctional materials or a consequence of self-assembly. [144] For SCMs, this hierarchy is the simplest method by which to obtain multiple optical effects from the same structure; for example, the angular dependence of an SCM can be reduced by the including diffusive elements. Using combinations of self-assembly and top-down fabrication methods, scientists have been able to create hierarchical nanostructures for a variety of applications. [145]

Absorption and scattering can also be used to influence the color produced by SCMs. Scattering within an imperfect SCM or reflections from surfaces outside of the SCM can lead to a desaturation of a structural color. If saturated colors are desired, absorbers can be used to mitigate the color desaturation caused by scattering. On the other hand, strong scattering can itself lead to enhanced color purity. For example, when there is a surface external to the SCM that is affecting its color, a strong scattering layer can be used to reduce the coherence of the reflecting surface.

Nature has developed a panoply of SCMs using a very limited set of materials within extremely constrained systems. Biological systems must, naturally, rely on biological components and bottom-up self-assembly to create any material; for SCMs,

the most limiting constraint is the lack of high refractive index materials in nature which limits the obtainable index contrast for SCMs. Tools and materials developed in the laboratory can be used to expand the diversity of SCMs leading to a variety of possibilities that cannot be observed in nature. By using plasmonic materials and high-index dielectrics, which are typically unavailable for biological organisms, the physical size of SCMs can be greatly reduced. In addition, the large imaginary portion of the complex refractive index of these materials causes the phase change upon reflection from their surface to be anomalous (different from the 0 or  $\pi$  phase change from non-absorbing materials). This anomalous phase-shift can lead to many types of SCMs which cannot be created in other ways as well as allow for a great reduction in the thickness required for thin-film SCMs.

This review discusses three techniques to create or enhance SCMs: (1) hierarchical structuration to take advantage of the optical properties of multiple structural elements, (2) absorption for color purification of SCMs or to cause asymmetric effects due to the anomalous phase change upon reflection from an absorbing layer, and (3) introduction of plasmonic moieties to reduce the physical size of SCMs in order to create materials which do not exist in nature. All of these techniques use engineered structures to combine relatively simple optical effects and achieve complex optical properties.

## **4.2 Hierarchy**

Biology has developed a host of SCMs including diffraction gratings, multilayers, and 3D photonic crystals. [74] A particular strength of these biological SCMs is their use of hierarchy to generate optical effects that would not be possible using idealized models one might find in a standard optics textbook. For example, a common method to reduce the angle-dependence of structural color is to introduce disorder into a 3D photonic crystal such that the local order is strong enough to create a structural color, but the long-range order is weak. [146] Thus, many different photonic crystal "grains" of slightly different orientations are observed simultaneously and their individual angle-dependence is averaged such that only the primary peak

is easily observed. [31, 146–149] In addition, hierarchical structuration can be used to diffuse (and therefore reduce the angular dependence) of a structural color. For example, many species of butterfly, including those of the famous *Morpho* genus, reduce color iridescence due to combinations of diffraction gratings and multilayer structures. [150, 151]

A recurring motif of hierarchical SCMs in nature is the combination of a diffraction grating with another optical element; a wide range of possibilities for such a combination is depicted in Figures 4.1 and 4.2. Often, the superposition of a diffraction grating with another optical element, such as 3D photonic crystal or a multilayer, as is the case for *Morpho rhetenor*, is used to give a wider angular distribution to the visibility of a structural color (Fig. 4.1a) [65, 152]. However, several other interesting effects can be created by creating hierarchical structural color materials of different types. A thin film in conjunction with a diffraction grating can produce predictable structural colors which can be used as a structural color printing mechanism (Fig. 4.1b) [153]. Another option is to combine one diffraction grating with an orthogonally oriented diffraction grating. This can lead to a reverse color-order diffraction pattern wherein the color shifts from red to blue as the observation angle is increased, instead of the typical blue-to-red color order, an effect that can also be found in nature on the wings of the male butterfly *Pierella luna* (Fig. 4.2c) [154, 155]. In these examples, the combination of a diffracting grating with another optical structure is used to achieve novel optical properties. Rather than superposing a diffraction grating onto another optical structure, other types of geometries can be combined hierarchically to generate complex optical effects. Combining a multilayer with a retroreflector in different configurations can give rise to spatially modulated reflection colors as exemplified in the butterfly *Papilio blumei* [156] (Fig. 4.3a(i-iv)). By slightly modifying the organization of the structural elements—namely by placing the multilayer above the retroreflecting concavities rather than depositing it conformally on top of them—a different effect can be created wherein the reflected color of the multilayer and its transmission color can both be observed in reflection mode, albeit with orthogonal polarizations [156] (Fig. 4.3a(v)). Meanwhile, diffraction gratings are also frequently used to increase the light transfer efficiency into or out of light-generating

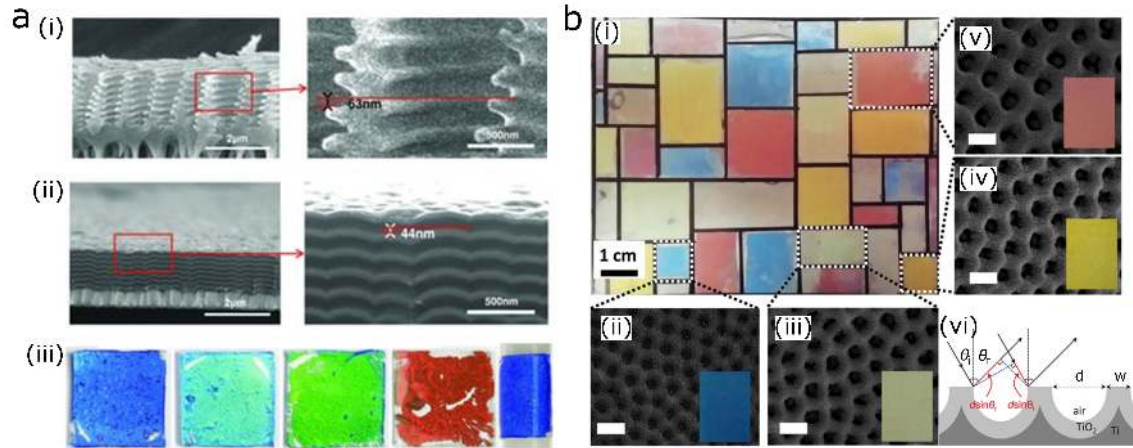


Figure 4.1: Combination of diffraction gratings with other structural color elements. a) [152] Diffraction Grating + Multilayer. Structural comparison between butterflies and fabricated angle-insensitive structural color films. (i) (left) Cross-sectional SEM image of the multilayered ridges on the dorsal ground scale of a *Morpho Didius* butterfly. (right) A close-up view of the ridges, showing a vertical offset of 63 nm between two neighboring ridges, taken from the area outlined in red. (ii) (left) Cross-sectional SEM image of the deposited multilayer thin film. The bright layers are SiO<sub>2</sub> and the dark layers are TiO<sub>2</sub>. A Cr-covered monolayer of silica microspheres is located at the bottom of the multilayer structure, causing a column-like structure of in the multilayer. (right) A close-up view of the multilayer, showing a vertical offset of 44 nm between neighboring columns (similar to the ridge offset in (i)), taken from the area outlined in red. (iii) Images of fabricated films. Various colors ranging from deep blue through green to coppery red realized by controlling the layer thicknesses. (left) Image of the deep blue reflector wrapped around a rod with a diameter of 1 cm. Note that the color appears the same throughout, even though the reflector is bent, and thus presents a viewing angle that varies from 0 to 90°. (right) b) [153] Diffraction Grating + Thin Film. Structural color painting using thin-film structured gratings in Littrow configuration. (i) Centimeter-scale reproduction of a Mondrian painting titled "Composition with Color Planes and Gray Lines". (ii-v) SEM images of selected areas, which illustrate different diameters and uniform alignment of the nanobowls. White scale bars are 200 nm. (vi) Ray diagram depicting light reflection from TiO<sub>2</sub> nanobowls of diameter  $d$  and wall thickness  $w$ .  $\theta_i$  and  $\theta_r$  are the angle of incidence and reflection, respectively.

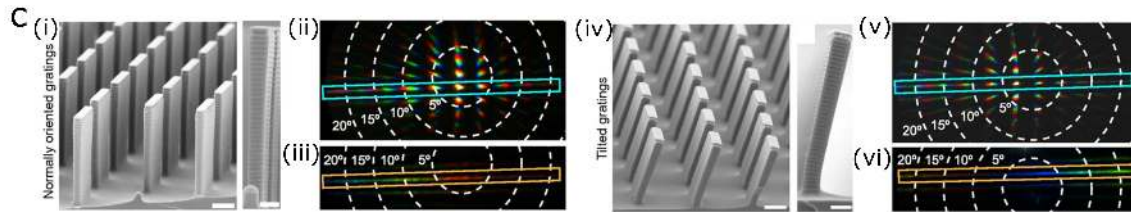


Figure 4.2: Combination of diffraction gratings with other structural color elements. (continued). c) [154] Diffraction Grating + Diffraction Grating. Reverse color-order diffraction grating based on the Pierella luna butterfly. (i) SEM of an array of scalloped microplates. Scale bar, 5  $\mu\text{m}$ . (left) SEM of an individual plate with regular scallops. Scale bar, 2  $\mu\text{m}$ . (right) (ii) Diffraction pattern caused by the periodic ensemble of microplates for 45° light incidence. A choice of propagation angles is visualized by the white dashed lines. (iii) Diffraction pattern resulting from the scallops on individual plates. (iv-vii) Same as i-iii, for tilted gratings.

or absorbing structures [157–165] as gratings promote coupling of light that would otherwise be trapped by total internal reflection modes to free space. As seen in Fig. 4.3b, the addition of gratings can therefore be lead to brighter light emitting diodes (LEDs) [166, 167]. In all of the above cases, hierarchy is used to enrich the optical properties of an SCM. The examples presented so far only rely on the combination of different morphologies of purely dielectric materials to generate interesting and useful structures. An even greater variety of effects can be achieved by introducing optically active elements, such as absorbers, into SCMs.

### 4.3 Absorption

Typically, absorption is added to a SCM in order to reduce the desaturation of color that results from nonspecific scattering. Since scattering is typically stronger for shorter wavelengths, this effect is most noticeable when a structural blue color is being created, as is the case for the brilliant blue Steller’s jay bird which appears pure white (due to scattering) when the bird has no melanin in its plumage. [17] In real-world structures (whether biological or man-made), there are many causes of such nonspecific scattering such as inevitable deviations from perfect periodicity and

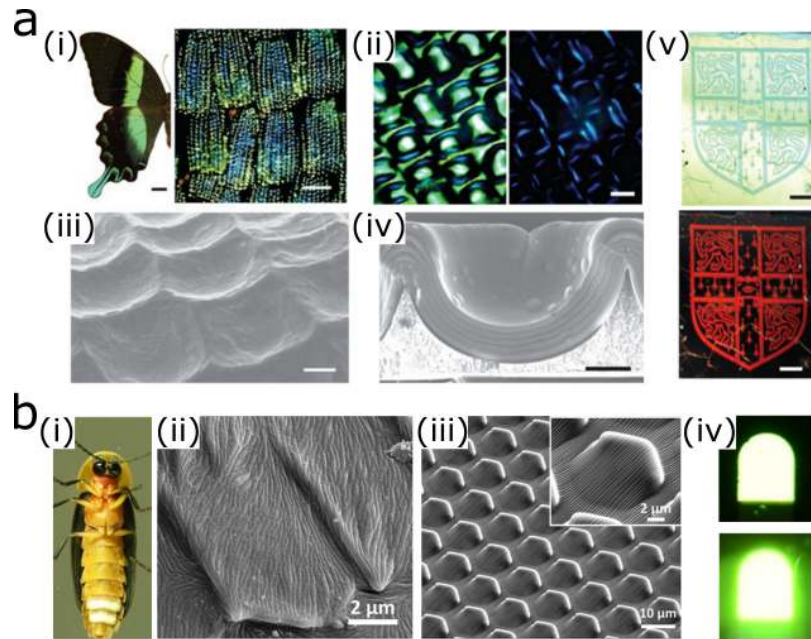


Figure 4.3: Arrayed hierarchical optical structures. a) [156] Multilayer + Retroreflector for polarization-dependent color. (i) The bright green wings of the *P. blumei* butterfly result from the mixing of the different colors that are reflected from different regions of the scales found on the wings of these butterflies (scale bars: left, 1 cm; right, 100  $\mu\text{m}$ ). (ii-iii), Optical micrographs (ii, scale bar: 5  $\mu\text{m}$ ) and SEM images (iii, scale bar: 2  $\mu\text{m}$ ) showing that the surface of a wing scale is covered with concavities (diameter  $\approx$  5-10  $\mu\text{m}$ ) that are arranged in ordered lines along the scale. These concavities are clad with a multilayer that reflects yellow-green light at their centers and blue at their edges (ii, left). By observing the scales in an optical microscope with crossed polarizers, the yellow-green light is extinguished, but the blue light can still be detected along four segments of each edge (ii, right). (iv) SEM of a fabricated concavity covered by a conformal multilayer stack of 11 alternating layers of titania and alumina (scale bar: 1  $\mu\text{m}$ ). (v) Samples viewed in direct specular reflection (top) and in retro-reflection (bottom) (scale bars 5 mm), show a striking change in color from blue to red, for a different sample with the multilayer above the concavity. b) [167] Combination of hierarchical structures with an LED to enhance out-coupling of light based on the microstructures found in firefly lantern scales. (i) An optical image of a male firefly (*Pyrocoelia rufa*). (ii) SEM of the male firefly lantern cuticle. (iii) Perspective SEM of the hierarchical structures designed based on the structures in (ii). (inset: magnified view). (iv) Photographs of OLEDs in operation (top) without and (bottom) with structured surfaces.



the presence of unintended surface roughness. An absorbing moiety (whether a dye or an absorbing plasmonic nanoparticle) dispersed homogeneously throughout the SCM can greatly reduce the desaturation effects of this nonspecific scattering. Even for broadband absorbers such as carbon black, the color purity of the material can be improved, as the intensity of the structural color peak relative to the background will be increased. [6,8,11,98,168–170] This approach is general and will improve the color saturation for color produced by multilayers or 3D photonic crystals, provided the doping level of the absorbing particles is correctly optimized. For situations in which the desired color is known a priori, a specific absorber can be chosen such that its absorption spectrum does not overlap with the structural color peak; however, it can be challenging to find an absorber whose spectrum precisely corresponds to the desired color of the SCM. [14,15,80]

When the absorbing moieties are localized at defined locations within the SCM instead of distributed homogeneously throughout it, more complicated optical effects can arise beyond the reduction of nonspecific scattering. Specifically, drastically different colors can be observed by using different illumination and observation conditions. Asymmetric reflection (and absorption) can be observed by defining an absorbing layer on a transparent substrate that is coated with at least one layer of a dielectric thin film (one which would give rise to structural color even in the absence of an absorber). The effect can be observed with a range of absorbing layers, for example plasmonic nanoparticles [171] (see Chapter 6), structured plasmonic absorbers such as metal hole arrays [172], or simply thin metal films (see Chapter 6). A fully dielectric Bragg stack without absorbers will appear identical regardless of which side is being observed. As shown in Fig.4.4, the addition of an absorbing layer leads to a different observed color when viewing from the top of the sample as compared to the bottom. This geometry allows for the structure to be partially transparent; therefore, the structure isn't equivalent to a substrate coated on either side with a pigment (which would also display different colors depending on which side is being viewed) and a third color can be observed when viewing the sample in transmission mode. Due to conservation of energy, the difference in reflected color must also manifest itself in a difference in the absorption or scattering between the different sides of the

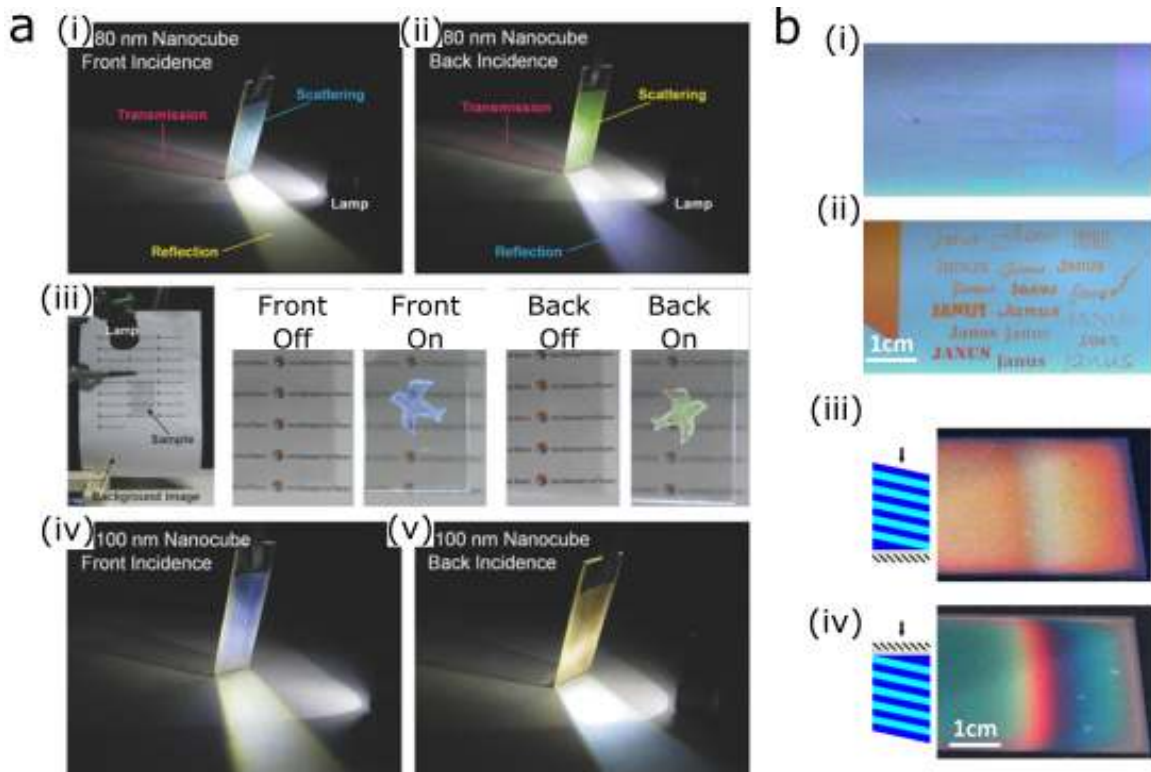


Figure 4.4: Asymmetric optical effects achieved by adding structured absorption to SCMs. a) [171] Optical behaviors of Ag nanocubes on thin TiO<sub>2</sub>-coated glass plates. (i, ii, iv, v) Asymmetric color routing for the front (i, iv) and back (ii, v) incidence. (iii) Dichromatic scattering. A bird image drawn by Ag nanocubes is almost invisible under ambient light both from the front and back side. The image is clearly visible both from the front and back side when the sample is illuminated by a Xe lamp from the side of the observer. b)(Chapter 6) Viewing direction dependent optical effects from Janus coatings using a thin metal film as the absorbing element. (i-ii) Partially invisible Janus color patterns (i) Photograph of the coating side surface of a micro-patterned asymmetric structural color stack of SiN and SiO<sub>2</sub> with a thin film of patterned chromium designed to match colors of the features and the background from the coating side and thus hide the pattern. (ii) Photograph of the substrate side surface of the sample in (i) showing high contrast between the color in the regions containing chromium and those containing only the Bragg stack. (iii) Photograph of a structure of SiN/SiO<sub>2</sub> with a gradient-thickness layer of SiN and a thin film of chromium showing a near solid orange color when viewed from the coating side. (iv) Sample in (iii) photographed from the substrate side, revealing a rainbow pattern in the region of the thickness gradient.

structure since the transmission must be the same due to time-reversal symmetry. This effect has been used to create asymmetric absorption materials for potential applications in photovoltaics [172, 173], facile glass structural coloration [174], and plasmonic color routing [171]. Another interesting feature is that multilayer Bragg stacks can be used to further tune the reflected colors from either side of the SCM and allow for viewing direction dependent camouflage of a photolithographically designed pattern (Fig 4.4b(i)). Moreover, the introduction of a gradient-thickness layer into a Bragg stack designed with its peak in the center of the visible spectrum, can allow for a sample that appears nearly monochromatic from one side, while allowing for a smooth color gamut to be viewed from the other side (see Chapter 6)(Fig 4.4b). This type of coloration methodology can also be used on non-transparent substrates for a variety of color applications as shown in Figure 4.5. Ultra-thin structural color coatings [175–179] such as the one highlighted in Fig. 4.5a, ultra-thin absorbing coatings [180–183] can be used to color a material with a much thinner coating that would be possible with a standard Bragg stack. This method has even been applied to solar cells to color the solar cells by varying the thickness of a dielectric within the photovoltaic architecture (Fig. 4.5b) [184, 185].

If metal films are used instead of absorbing particles, the absorption begins to affect the resonance of the SCM more directly due to the typically high index of refraction of metals as compared to the effective index of refraction of a dielectric film containing metal nanoparticles. In this way, color filters can be made much thinner than conventional dielectric Bragg stacks by using metal-insulator-metal structures [186–191]. When there are a large number of metal layers separated by dielectrics, and the layers are sufficiently thin, such a material constitutes one type of a hyperbolic metamaterial [192] and can be used for applications in superlensing, negative index of refraction, and sensing [193]. Until this point, we have shown that the addition of absorbing layers can be applied to increase the color saturation of a SCM and that by structuring the absorption within the SCM, ultra-thin colored materials and asymmetric reflection/absorption materials can be created. All of these examples of patterned absorption, rely on tight confinement of the absorber in one dimension only (although large-scale patterning of this confinement is also possible). With the

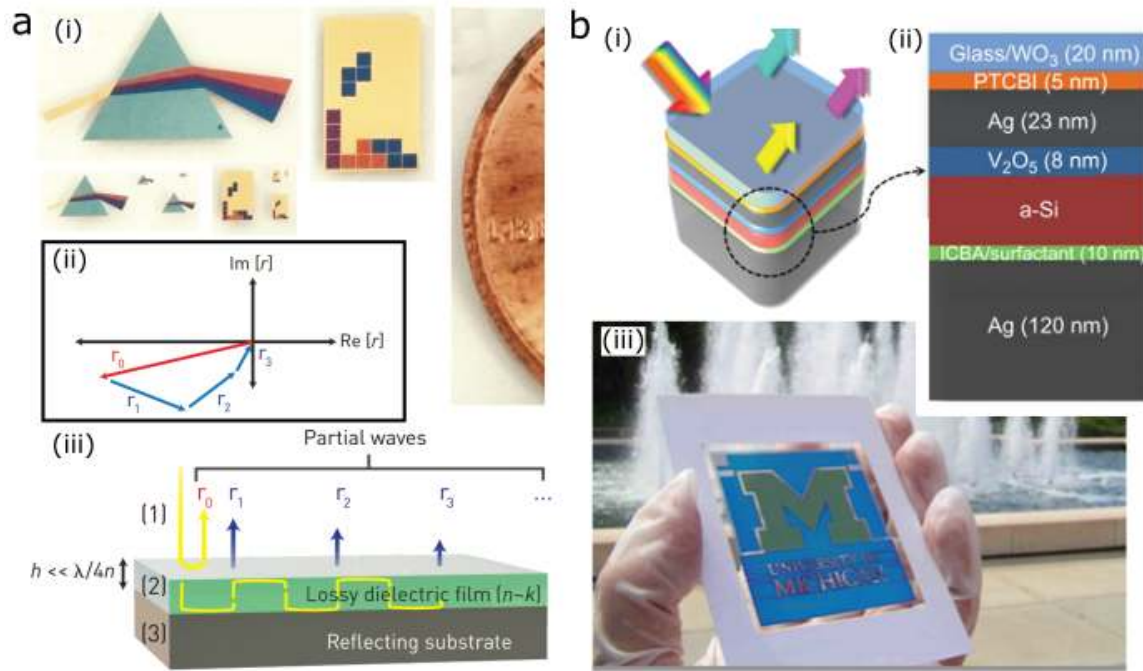


Figure 4.5: Ultra-thin SCMs. a) [176] Germanium thin film colored film. (i) Five steps of photolithography with alignment are used to selectively deposit an optically thick layer of Au on a glass slide, followed by Ge layers of either 7, 11, 15 or 25 nm. This yields light pink, purple, dark blue and light blue colors, respectively (ii) Plot showing the sum of the partial reflections from a lossy dielectric film on a reflecting substrate leading to a suppression of reflection for a specific wavelength. (iii) Schematic showing the partial reflections in (ii). b) [184] Colored ultra-thin photovoltaic. (i) Schematic of the device structure. (ii) The cathode comprises a thick Ag layer and an organic layer, and a dielectric-metal structure is used for the anode. Between the two electrodes is an ultrathin a-Si layer. (iii) A university logo, consisting of green and blue colors, is successfully realized with the generation of electric power.

addition of patterning the absorber in two and three dimensions on smaller length scales, we enter the realm of plasmonics and allow for the creation of a host of colored materials.

## 4.4 Plasmonics

In the previous section, the addition of plasmonic absorbers was discussed as a method for either providing wavelength-selective absorption to improve the color saturation of an SCM or a way to tailor the complex refractive index of an absorbing layer to achieve asymmetric reflection/absorption properties in a multilayer architecture. In addition to these applications, plasmonic absorbers can be designed or patterned to allow for polarization- or angle-dependent color effects enabled by the difference in efficiency with which light can couple into the absorbing plasmonic modes depending on its polarization and incidence angle.

Several studies have probed using plasmonic absorbers for polarization and angle dependent colors. Plasmonic absorbers featuring asymmetric geometries can be used to tune the color for two orthogonal resonances nearly independently [194] (Fig. 4.6a). Angular asymmetry in the color produced by a grating can be achieved by coating the grating asymmetrically with a plasmonic metal [195] (Fig. 4.6b). Similarly, by introducing an analyzing polarizer into the setup, color filters which produce several different colors depending on the polarization of the incident illumination and the relative angle of the analyzing polarizer can be created [196] (Fig. 4.7c). In addition, metal nanowire arrays with different periodicities [197–200] and pillar-based gratings (sometimes referred to as vertical nanowires) [201–204] have also been used to create polarization-dependent color filters. Such polarization and angle dependent structures can be used as filters or color routers in optical experiments or as security materials for anti-counterfeiting purposes. As discussed previously, by incorporating hierarchical structures and absorbing materials, the photonic properties of SCMs can be improved, while the number of repeating units, and thus their physical size, can remain constant or even be reduced. The dimensions of these structures can be reduced even further by creating metasurfaces, the two-dimensional analog of metamaterials [205]. These

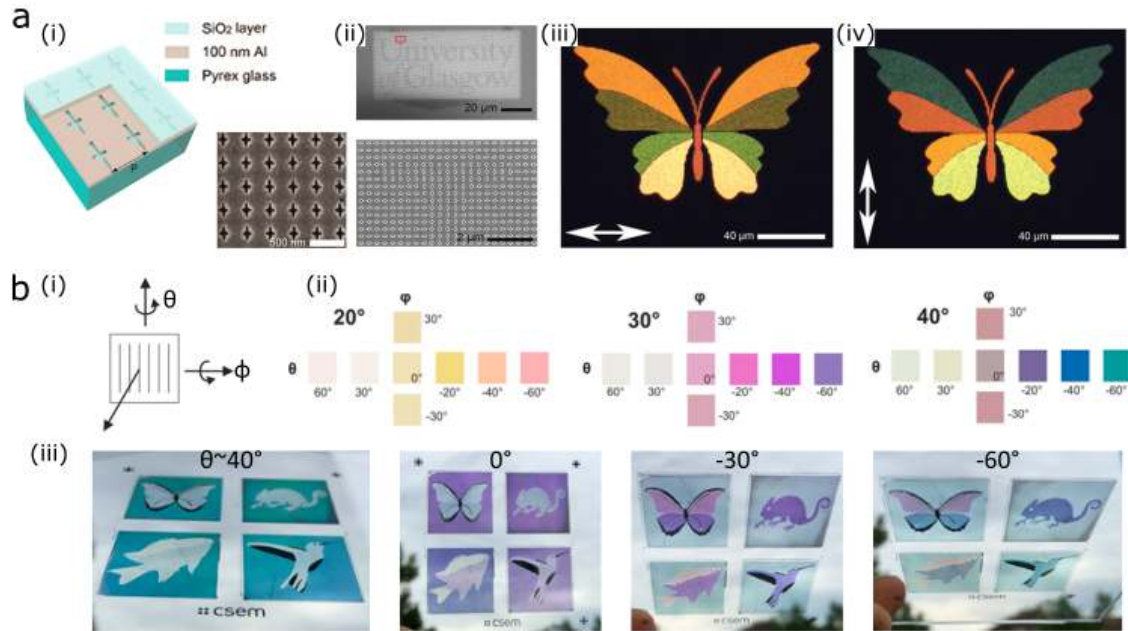


Figure 4.6: Polarization- and angle-dependent colors created using patterned plasmonic absorbers. a) [194] Polarization-dependent structural colors based on t-shaped resonators (i) (left) Schematics showing aperture geometry and arrangement and (right) SEM of a typical pixel array. Scale bar 500 nm. (ii) SEM image with enlarged view shows the top right part of letter U. The pixels in letter sections are rotated through  $90^\circ$  with respect to those in the background region. Scale bars, 20  $\mu\text{m}$  and 2  $\mu\text{m}$ . (iii - iv) Microscope images of a butterfly with switchable wing panel colors due to the electric-field of the incident light being polarized along the x and y-axes, respectively (the arrows display the oscillation direction of the electric-field). Scale bars 40  $\mu\text{m}$ . b) [195] Asymmetric color behavior of asymmetric aluminum coated gratings. (i) Sketch defining viewing angles  $\theta$  and  $\phi$ . (ii) Measured colors of the samples characterized for different evaporation angles (bold) and different viewing angles  $\theta$  and  $\phi$  defined in sketch. Colors mainly appear at negative angles  $\theta$ . (iii) Glass substrates with 4 different sample areas (2 cm  $\times$  2 cm) created by the evaporation angles  $20^\circ$ ,  $30^\circ$  and  $40^\circ$ . Photographs were taken in front of a cloudy sky and with unpolarized light.

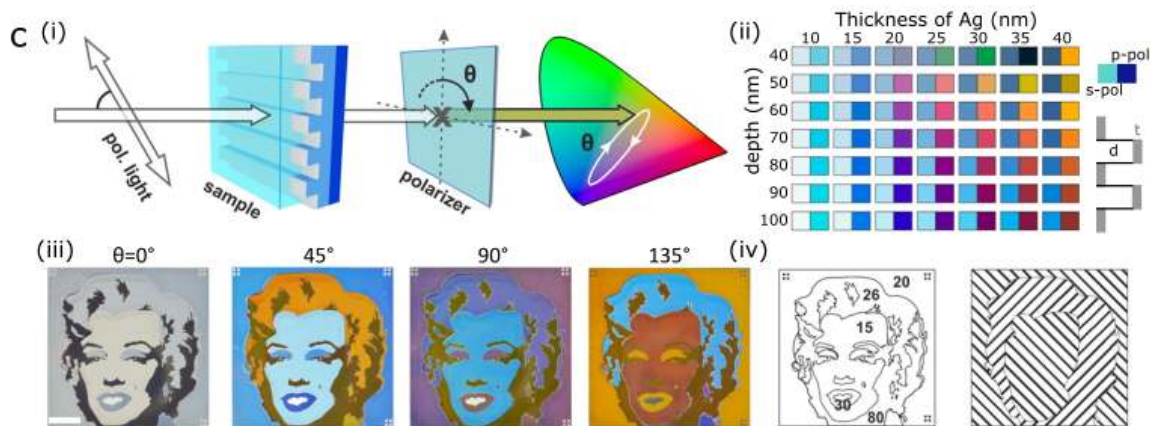


Figure 4.7: Polarization- and angle-dependent colors created using patterned plasmonic absorbers. (continued) c) [196] Four-fold color filter (i) Schematic of the experimental setup showing (from left to right) the input linearly-polarized light, the plasmonic phase-retarding sample, the analyzing polarizer, the CIE x-y color space with a closed loop representing the obtainable colors for the sample. (ii) Simulated color map of s-pol and p-pol colors for varying depth and silver thickness. The illustrations qualitatively indicate the arrangements. The color palette displays the computed transmission color. (iii) Images of Marilyn Monroe for four different analyzing polarizer settings (angle  $\theta$  is indicated, scale bar: 1cm). (iv) Illustration of the mask consisting of five regions of different silver thicknesses (bold) and the analyzing polarizer designed to allow for contrast between her hair and the rest of the image.

can be designed to produce a variety of optical effects with extremely thin photonic devices. Several review articles have already been written on this topic. [206–208] Here, we will focus on the use of metasurfaces to achieve color effects similar to those discussed above.

Metasurfaces can be used to create the highest resolution color images in existence, which has potential in high density data storage, anti-counterfeiting, and color filtering for display technologies. Taking advantage of the high physical confinement allowed by plasmonic structures and the utility of modern fabrication methods, specific plasmonic absorbers can be fabricated with high precision to allow for full color images to be achieved on unprecedented size scales. Nanoscale arrays of pillars, holes, or pillar/hole combinations coated with films of plasmonic metals can feature high quality factor resonances, generate different colors in pixels as small as  $250 \times 250$  nanometers, and allow for 100,000 dpi printing as shown in Fig. 4.8a. [209] Many groups have developed and expanded this field by increasing the scalability of the technique [210], or creating angle-independent structural color on a similar length scale [211]. More recently, there has been a growing trend to move away from expensive noble metals [212, 213] as the plasmonic material and shift to using aluminum, which has favorable plasmonic properties at visible wavelengths and gives a more neutral white color for the back-reflected light. Using aluminum, the color palette available for metal-coated photoresist post arrays has been expanded (Fig. 4.8b) [214–216]. Additional geometries of aluminum nano-disk or nano-hole metal-insulator-metal structures (Fig. 4.9c) [217, 218] allow for the use of different fabrication technologies to create the structures, with similar achievable colors and resolutions. These techniques often employ soft lithography to replicate an electron-beam lithographically generated master so that many samples can be created rapidly. Others rely on colloidal lithography [39, 81, 219] to generate resonators of the desired shape and periodicity, but this technique doesn't allow for high-resolution patterning of the resultant structures [220–224]. Directed self-assembly of pre-synthesized nanoparticles can be used to allow for high resolution and polarization-dependent color [225], but this technique requires a different photolithographic step for every type of nanoparticle (and therefore basis color) being deposited. A more realistic



method for generating a large number of photonic/plasmonic nanostructures is to use nanoimprint lithography as discussed in a recent review. [226] This type of structural color printing has been further pushed towards display applications by integrating the plasmonic pixels with a tunable liquid crystal to enable a method to actively change the color of a plasmonic image. [227, 228]

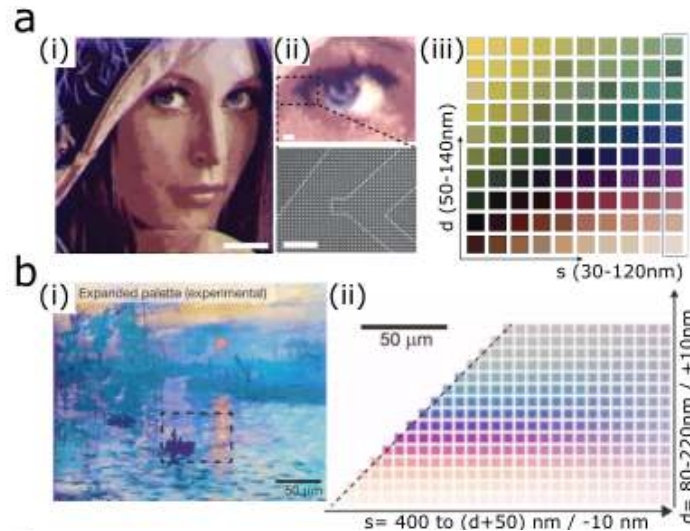


Figure 4.8: Improvements in color palette available for plasmonic printing. a) [209] Gold-coated pillar arrays with varying spacing and diameter. (i) Optical micrographs of the Lena image after metal deposition. (ii) Optical micrograph of an enlarged region of the image (top) with SEM image of the indicated region (bottom) For clarity, the individual regions of similarly sized disks are separated by the dotted lines. Each pixel consists of a  $2 \times 2$  array of disks with a pitch of 250 nm. (iii) Full color palette obtainable with this method showing similar colors from bottom left to top right, indicating that areas with similar fill factors produce areas with similar colors. Squares are  $12 \mu\text{m} \times 12 \mu\text{m}$ . The highlighted column was used to produce the image in a(i-ii). b) [214] Aluminum-coated pillar arrays with varying space and diameter. (i) Realistic reproduction of Monet's "Impression, Sunrise" using an expanded palette of colors. (ii) Spacing color palette with both size variations ( $d = 80$  to  $220$  nm) and spacing variations ( $s = d + 50$  to  $400$  nm) among four nanodisks within an  $800 \times 800$  nm pixel, at a step size of 10 and 20 nm, respectively. Optical images were normalized to a white background.

Plasmonic absorbers can be used to enrich SCMs in a variety of ways. By designing asymmetric plasmonic absorbers, polarization- and angle-dependent color

filters can be created. By increasing the dimensionality of this patterning further, metasurfaces with all kinds of optical properties can be fabricated. For the purposes of this review, we focus on those metasurfaces with applications related to color; the field of plasmonic printing allows for the highest resolution color images possible to be created, although the complexity of the fabrication does not yet allow for large numbers or unique samples or dynamic display technologies.

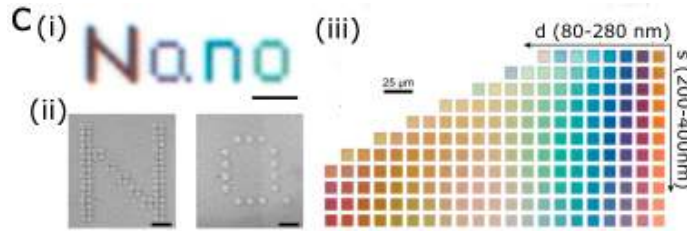


Figure 4.9: Improvements in color palette available for plasmonic printing. (continued) c) [217] Aluminum nano-disks on aluminum oxide coated aluminum with varying spacing and diameter. (i) Optical micrograph of the subwavelength-pixel "Nano" letters in color. The patterns are composed of dark color and colored pixels (violet,  $d = 100$  nm; blue,  $d = 120$  nm; green,  $d = 140$  nm). Each single pixel is a  $300 \text{ nm} \times 300 \text{ nm}$  square. The images were obtained through an objective of  $150\times$  and  $0.9 \text{ NA}$ . Scale bar,  $2 \mu\text{m}$ . (ii) SEM images of enlarged regions of "N" and "a". Scale bar,  $500 \text{ nm}$ . (iii) Optical image of nanodisk arrays with varying diameters  $d$  from  $80$  to  $280$  nm in  $10 \text{ nm}$  increments and periods  $P$  from  $200$  to  $400$  nm in  $20 \text{ nm}$  increments. The image was obtained with a  $20\times$  objective ( $\text{NA} = 0.45$ ) under unpolarized white light illumination.

## 4.5 Conclusions

In this review, we have discussed several different methods for creating novel SCMs: (1) Hierarchical structuration can be used to generate optical effects that are unobtainable with simple geometries, (2) absorption can be used either to purify the spectrum of an SCM or to expand the SCM's behavior due to the plasmonic or optical phase-change properties of the defined absorbing layer, and (3) plasmonic materials can be used to create much smaller photonic materials for generating color by taking advantage of the extremely high confinement and purity of the available

photonic modes in the structures. The toolkit discussed in this review has been built up from combinations of classical SCMs and includes the addition of absorbers as well as patterned plasmonic materials. These tools have led to the discovery of new types of SCMs and have allowed for the improvement and extension of their optical performance. Decades or centuries after understanding the fundamentals of the individual optical elements, the field of structural coloration is still very active and the combination of simple and well understood optical elements continues to yield materials with surprising optical effects. The discovery of the intricate nature of light matter interactions at different length scales naturally precedes applications, but it is clear that such effects will be useful in diverse fields of technologies, including imaging, display technologies, photovoltaics, colorimetric sensing, high density optical storage, and security printing will be improved by their development.

# Chapter 5

## Bio-inspired micro-grating arrays: Mimicking the reverse color diffraction elements evolved by the butterfly *Pierella luna*

In this chapter we present a specific example of the types of hierarchical structurally colored materials presented in Chapter 4. Here, the combination of a diffraction grating with an orthogonally oriented diffraction grating allows for the observation of diffraction satisfying the grating equation for both diffraction gratings to be observed simultaneously.

### 5.1 Overview

In the course of evolution, many organisms have developed unique light manipulation strategies that rely on intriguing combinations of a broad range of optical effects generated by materials with sophisticated multiscale hierarchical structural arrangements. By exploiting the optical principles underlying natural structural color, we can generate new photonic materials. Researchers have only just begun to match nature's morphological and compositional complexity in man-made materials using

nanofabrication. We present a bioinspired photonic material that mimics the reverse color-order diffraction found in the butterfly *Pierella luna*. Exploiting and improving the butterfly's strategy, we create photonic materials that increase our basic understanding of the optical interplay of hierarchical structures and provide a platform for the development of novel photonic devices.

### 5.1.1 Abstract

Recently, diffraction elements that reverse the color sequence normally observed in planar diffraction gratings have been found in the wing scales of the butterfly *Pierella luna*. Here, we describe the creation of an artificial photonic material mimicking this reverse color-order diffraction effect. The bioinspired system consists of ordered arrays of vertically oriented microdiffraction gratings. We present a detailed analysis and modeling of the coupling of diffraction resulting from individual structural components and demonstrate its strong dependence on the orientation of the individual miniature gratings. This photonic material could provide a basis for novel developments in biosensing, anticounterfeiting, and efficient light management in photovoltaic systems and light-emitting diodes.

## 5.2 Introduction

Three-dimensional photonic crystals [74,229–232], materials with two-dimensional micro- or nanosized periodic morphologies [233–235], and one-dimensional multilayer configurations [236] have been identified as the primary cause of structural coloration in a wide variety of nonrelated biological organisms. In contrast, surface-confined diffraction elements for the separation of incident light into specific colors are less abundant in nature and have only been discovered in a handful of organisms [237], including a fossil polychaete [234], sea mouse *Aphrodita* sp. [233], and some flowering plants [238]. Recently, diffraction elements that reverse the color sequence normally observed in planar diffraction gratings have been found in the scales of the butterfly *Pierella luna* [155].

Inspired by this biological light manipulation strategy, we devised an artificial material morphology mimicking the butterfly's diffraction effect by creating periodic arrays of vertically oriented individual microdiffraction gratings. In addition to the butterfly-inspired reverse color-order diffraction arising from each individual micrograting, the periodicity between the individual gratings causes diffraction on a different length scale, leading to complex intensity distributions in experimentally measured angularly resolved reflection spectra. An in-depth analysis of the observed diffraction phenomenon complemented by optical modeling revealed a strong dependence of the optical signature on the orientation of the gratings. Such an effect can only be seen because of the hierarchical nature of the superposed, orthogonal grating features. To further elucidate the role of the different structural components for the emerging reflection spectra, the initially vertically oriented individual microgratings were subjected to a tilt, resulting in a predictable change of the surface's optical signature.

The dorsal side of the fore- and hind wings of *P. luna* males are dull brown in diffuse ambient illumination (Fig. 5.1A, Left). When exposed to directional illumination at grazing incidence, a coin-sized spot on each fore wing displays an angle-dependent color variation across the whole visible spectrum (Fig. 5.1A, Right). The color changes from red to blue with increasing observation angle, unlike the variation from blue to red normally observed in conventional diffraction gratings [100]. This reverse color diffraction effect results from the local morphology of individual scales within the colored spot on the fore wings [155]. The top parts of the scales are curled upward, orienting lines of periodically arranged cross-ribs perpendicular to the wing surface. (Fig. 5.1 C and D). Light incident at an angle onto the curled parts of the scales is diffracted by the cross-rib structure acting as a diffraction grating, with a periodicity of  $\approx 400$  nm. The alignment of the grating perpendicular to the surface results in the reverse color sequence that can be observed in angularly resolved reflection spectra and in the diffraction pattern (Fig. 5.1 E and F). Figure 5.2 shows a scanning electron micrograph (SEM) comparison of the butterfly scales responsible for the reverse color-order diffraction with those found in a region not showing structural color.

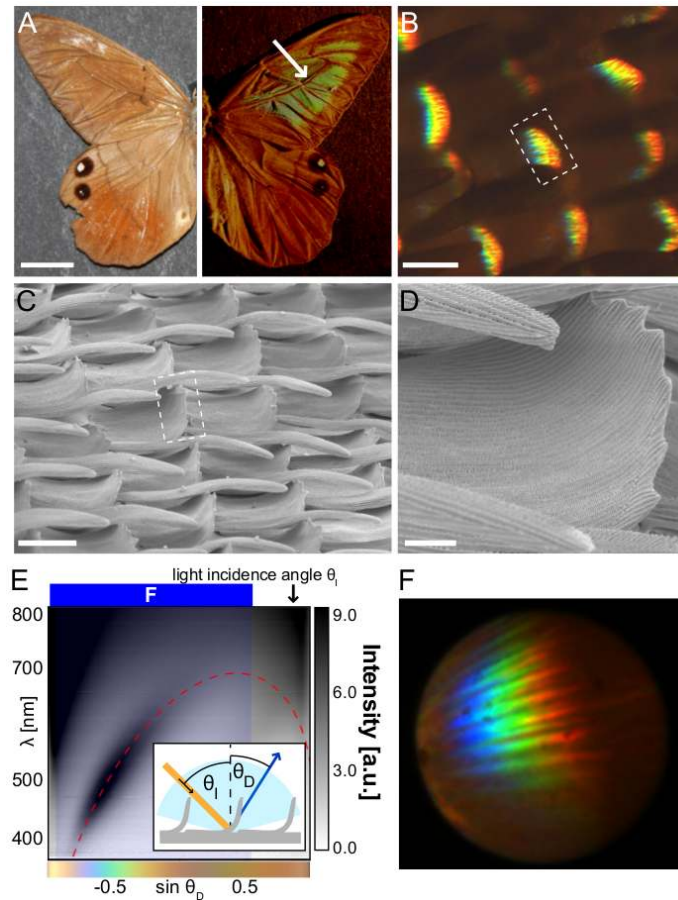


Figure 5.1: Optical properties of the curled scales in butterfly *Pierella luna*. (A) Optical image of *Pierella luna* under diffuse lighting (Left) and directional lighting at grazing incidence (Right). Scale bar, 10 mm. (B) Optical micrograph of *Pierella luna* scales under oblique illumination. Scale bar, 50 m. (C) SEM of scales in the colored wing region. Scale bar, 50 m. White dashed boxes in B and C mark the curled tops of the scales from which the color originates. (D) Close-up image of the curled region of the scale from which the color originates. Scale bar, 20 m (E) Gray-scale encoded reflection intensity as a function of wavelength and propagation direction showing the inverse color-order diffraction pattern for  $65^\circ$  light incidence. The red dashed line indicates the predicted location of the diffraction due to the cross-rib structures for an orientation of the curled scale sections of  $\sim 25^\circ$  relative to the surface normal and a cross-rib periodicity of 390 nm. The blue shaded region signifies the angle range for which the diffraction microscopy image of curled *P. luna* scales in F was obtained. The color bar under the graph shows the human-eye-perceived color for the spectra observed at the corresponding angles calculated by the CIE 1931 standards [239]. (F) Diffraction microscopy image of the colored spot of a *Pierella luna* wing showing multiple diffracted orders in similar angular locations due to the variation in the position and angle of the diffracting scales.

### 5.3 Mimicking *P. Luna*

The identification of this unusual diffraction effect on the wings of *P. luna* [155] provided inspiration for the development of a bioinspired photonic system that incorporates vertically oriented microdiffraction gratings with submicrometer periodicity analogous to the key features observed in the natural structure. In addition, the artificial system displays a periodic arrangement of the individual vertical gratings in large arrays with 2D microscale periodicity. This structural feature, which is not found in the natural organism, enriches the optical signature of the artificial system via coupling of the diffractive modes of the two present hierarchical morphologies. In the following, we discuss the optical properties of the artificial system and demonstrate that the modification of either one of the grating morphologies changes the diffraction signature in predictable ways.

The artificial system consists of an array of individual 10- $\mu\text{m}$ -long, 2- $\mu\text{m}$ -wide, and 18- $\mu\text{m}$ -high plates arranged in rows with an interplate spacing of 10  $\mu\text{m}$  and a separation of 5  $\mu\text{m}$  between individual rows of plates (Fig. 5.3A). These parameters result in an overall periodicity of 12  $\mu\text{m}$  in the direction perpendicular to the plates and 15  $\mu\text{m}$  in the direction collinear with the plane of the plates and the sample surface. A periodic wave pattern—termed “scallop”—of  $\approx 500\text{-nm}$  pitch runs along the sides of each individual plate (Fig. 5.3B).

The bioinspired diffraction elements are fabricated in a double-molding procedure. Starting from a silicon master, a periodic array of scalloped microplates is first cast into polydimethylsiloxane (PDMS) to form a negative mold [240], which is then replicated with a UV-curable epoxy to produce a positive replica of the master silicon structure with the original scallops on the individual plates well preserved. The silicon master is formed using the Bosch process [241], in which multiple etching and passivation steps give rise to the periodic undulations on the microplate surface. The pitch and height of these grating structures can be controlled by adjusting the etching parameters [242, 243]. Here, they are chosen to be comparable to the spacings and dimensions of the diffraction-inducing microribs on the *P. luna* scales (Fig. 5.3B), and hence are expected to cause a similar diffraction effect.



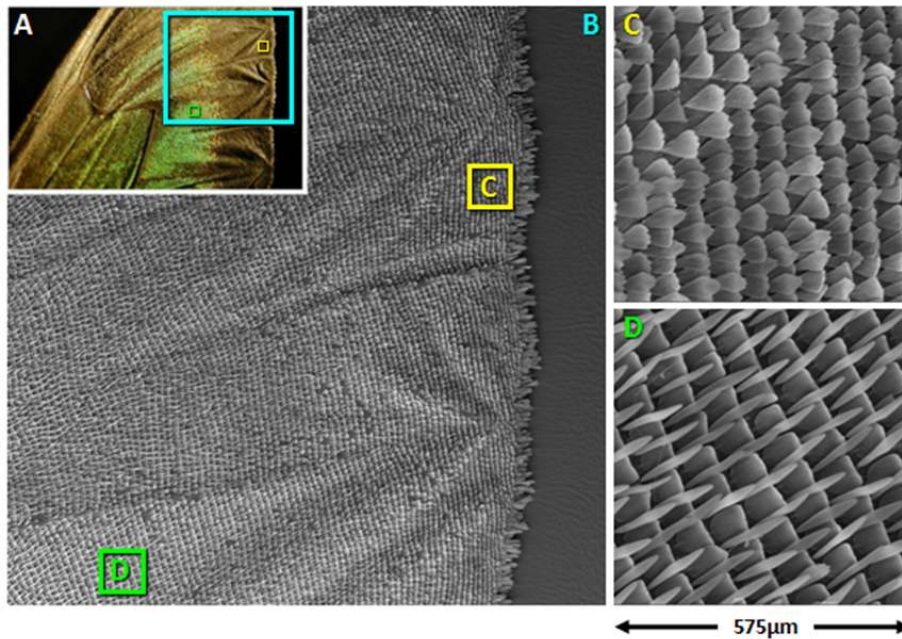


Figure 5.2: (A) Photograph of the dorsal side of the forewing of a male *P. Luna* butterfly. (B) SEM image of the region marked with a cyan square in A. (C) Higher magnification SEM of the yellow region marked in B showing the flat scales which don't show diffraction. (D) Higher magnification SEM of the green region marked in B showing the curled scales responsible for the reverse color-order diffraction.

Notice that in the biological system, the periodicity of the diffraction grating-supporting scales is of the order of  $80 \pm 10$  m along their length and  $60 \pm 10$  m perpendicular to the scale axis (Fig. 5.1B). Due to these large distances between diffraction elements and a nonnegligible amount of irregularity in the location of individual scales, no coherence is observed for light diffracted from adjacent scales. The overall color splitting only results from the diffraction caused by the cross-rib gratings on the individual scales, which is confirmed by variable-angle spectroscopy and by diffraction microscopy measurements (Fig. 5.1 D-F). Unlike in the biological system, the individual microdiffraction gratings in the artificial system are intentionally arranged in a highly periodic manner, which is expected to result in a richer diffraction signature and provide additional possibilities of tailoring the interaction of light beyond the diffraction induced by the scallops on the plates.

## 5.4 Analysis

Variable observation-angle spectroscopy performed on the artificial system serves to spectrally and angularly resolve parts of the complex diffraction pattern (Fig. 5.3C). For each measurement the plane of light incidence is chosen to be perpendicular to the surface of the individual microplates. The light incidence angle  $\theta_I$  is fixed and the observation angle  $\theta_D$  is varied in the plane of light incidence to capture light reflected in an angular range of  $\pm 75^\circ$  around the sample surface normal. A clearer description of the features in this measurement can be found in Fig. 5.4. Two main features are observed in these measurements:

i) Straight lines of higher intensity resulting from diffraction caused by the interplate periodicity represent the individual diffraction orders; the experimentally observed locations of these diffraction orders (shown in Fig. 5.3 C and H) can be directly calculated using the grating equation [100]. An example of such a calculation can be seen in Fig. S1. Due to the large interplate pitch of 12 m, the angular separation between adjacent diffraction orders and the free spectral range of each individual order are small. For light incident at an angle  $\theta_I = 45^\circ$ , eight positive propagating diffraction orders [left of the zeroth order at  $\sin(\theta) = -0.71$  in Fig. 5.3C]

and 53 negative propagating orders are captured with the highest intensity in the direct reflection (zeroth order) and in the adjacent orders.

ii) There is an arc-shaped distribution of intensity maxima across different diffraction orders (emphasized by the red shaded region in Fig. 5.3C).

This anomalous redistribution of light in the diffraction orders is caused by the scallops on each individual plate. To properly describe the diffraction resulting from the microdiffraction gratings oriented normally to the substrate, the grating equation [100] has to be reformulated taking into account their vertical orientation for diffraction in the plane of the scallops:

$$\lambda = \frac{d}{m}(\cos \theta_I + \cos \theta_D) \quad (5.1)$$

where  $d$  is the grating periodicity,  $m$  is the diffraction order,  $\theta_I$  is the light incidence angle, and  $\theta_D$  is the diffraction angle. This equation describes the arc-shaped pattern observed in the experiment under the assumption that the plates are vertical (Fig. 5.3C, red shaded region).

Imaging of the diffraction patterns by diffraction microscopy provides a direct visualization of the effects observed in the variable-angle spectroscopy measurements. The angle range that can be visualized in these measurements is determined by the numerical aperture of the microscope objective. For a given light incidence angle  $\theta_I$  the diffraction caused by the periodic ensemble of plates is most clearly observed when collecting light with the objective's axis aligned with the specular reflection direction  $\theta_D = -\theta_I$  (Fig. 5.3D, with the signal in the blue box corresponding to the blue shaded spectral range in Fig. 5.3C). Imaging of the sample's diffraction in the Littrow mounting [100], where light is incident on the sample through the microscope objective, allows for the capturing of the diffraction component induced by the scallops on the individual plates (Fig. 5.3E, with the signal in the yellow box corresponding to the yellow shaded spectral range in Fig. 5.3C). This feature is easily distinguished from the diffraction of the plate ensemble by the wider color spread.

Overall, the measurements provide clear evidence of coupling between the first-order mode of the scallop diffraction and the interplate periodicity-based diffraction

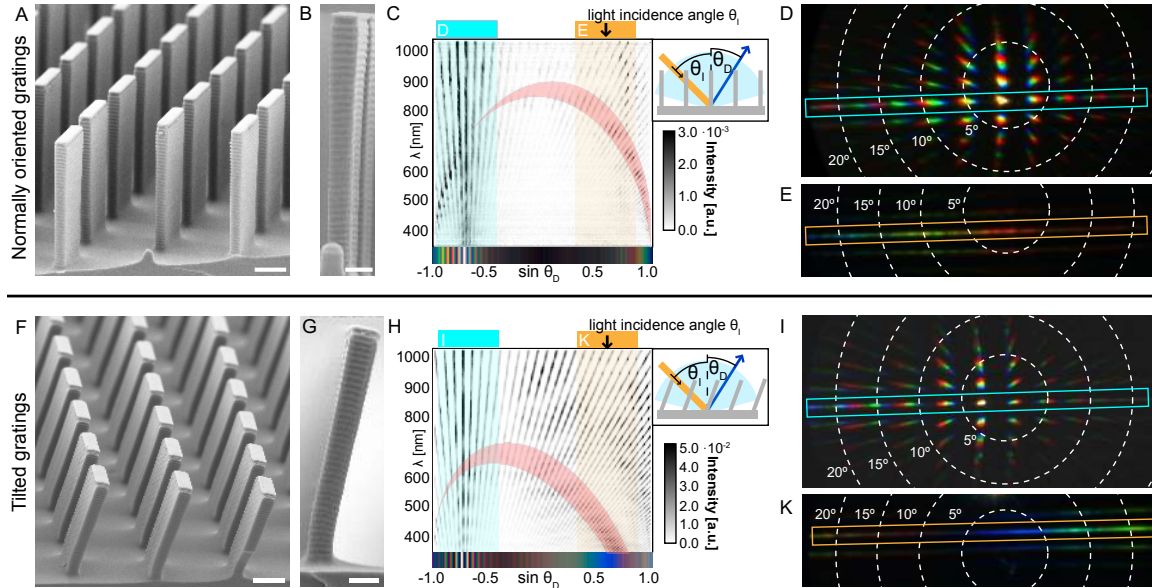


Figure 5.3: Geometry and optical properties of the artificial photonic structure mimicking *P. luna* with vertically oriented (Top) and tilted (Bottom) diffraction gratings. (A) SEM of the array of scalloped microplates. Scale bar, 5  $\mu\text{m}$ . (B) SEM of an individual plate with regular scallops. Scale bar, 2  $\mu\text{m}$ . (C) Variable-angle spectroscopic data for  $45^\circ$  light incidence showing the arc-shaped diffraction pattern caused by the diffraction from the scallops coupled with the diffraction due to the plates. (Inset, Top Right) Measurement geometry. The red overlay displays where the first diffraction order of the scallops based on the grating equation (Eq. 2) is expected for tilt angles of  $-3^\circ$  to  $5^\circ$ . The color bar under the graph shows the human-eye-perceived color for the spectra observed at the corresponding angles calculated by the CIE 1931 standards [239]. (D) Diffraction pattern caused by the periodic ensemble of microplates for  $45^\circ$  light incidence. A choice of propagation angles is visualized by the white dashed lines. The diffraction orders within the blue frame correspond to the diffraction observed in the angular range marked in blue in C. (E) Diffraction pattern resulting from the scallops on individual plates. The diffraction orders within the yellow frame correspond to the diffraction observed in the angular range marked in yellow in C. (F-K) Same as A-E, for tilted gratings. Red overlay in H marks the range where higher intensities are predicted by the grating equation for tilt angles between  $19^\circ$  and  $27^\circ$ .

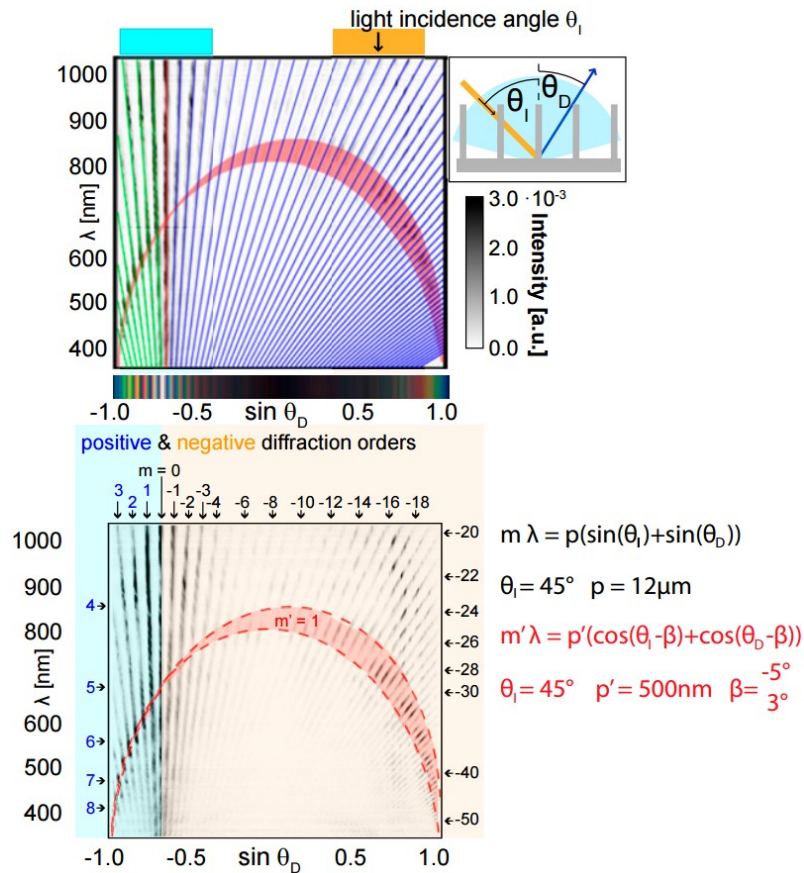


Figure 5.4: (Top) Excerpt from Fig. 5.3C showing the theoretically predicted locations of the positive (green), zeroth (red), and negative (blue) diffraction orders due to the periodicity of the plates as well as a shaded region showing the theoretically predicted location for diffraction due to the scallops within a  $-5^\circ$  to  $3^\circ$  plate tilt range. (Bottom) Excerpt from Fig. 5.3C numbering the diffraction orders and showing the equations and values used to predict their locations.

modes. The diffraction coupling can be controlled by adjusting the pitch of the scallops on individual plates and the interplate geometry in the manufacturing procedure. Likewise, a change in inclination of the microdiffraction gratings with respect to the substrate is expected to be reflected in a variation of the diffraction patterns. This change can indeed be observed by imposing a controlled tilt of  $\approx 20^\circ$  on the microplates by shearing the sample (Fig. 5.3 F and G).

The bending leaves the locations of the diffraction modes resulting from the interplate periodicity largely unaffected. Only minor wavelength-dependent intensity variations in each diffraction mode are apparent (Fig. 5.3 H and I). At large angles  $\theta_D$ , measured from the sample surface normal, a region of higher reflection intensity appears, which is related to the inclination of the individual plates, i.e., the blaze of the grating array. By contrast, the diffraction caused by the scallops on the individual plates is strongly influenced by the variation in plate tilt angle shifting the observed arc-shaped pattern in wavelength and angular position (Fig. 5.3 H and K). For micrometer-sized diffraction gratings, which have a tilt angle  $\beta$  relative to the surface normal, the diffraction grating equation can be reformulated as

$$\lambda = \frac{d}{m}(\cos(\theta_I - \beta) + \cos(\theta_D - \beta)) \quad (5.2)$$

By calculating a fit for the arc-shaped intensity distribution across the different diffraction orders in the variable-angle spectroscopic data (Fig. 5.3H, red shaded region), the tilt angle of the plates relative to the surface normal is found to be  $\beta \approx 23^\circ$ , in agreement with the SEM image analysis.

These findings are further supported by finite-difference time-domain simulations (FDTD) [244]. By comparing the plates with and without scalloping, the arc-shaped intensity distribution across diffraction orders is clearly identified as the diffraction resulting from the scallops (Fig. 5.5). Simulations of  $23^\circ$  tilted plates with  $45^\circ$  incident illumination show that this arc-shaped diffraction pattern gets skewed and spectrally shifted as predicted by Eq. 5.2 and observed in the experiments; the influence of the blaze of the regular array of individual gratings, separate from the effect of the scallops, can also be seen by closely examining Fig. 5.5 and noting that

the two tilted plate simulations have regions of high-intensity reflection at  $\sin(\theta) \approx 0$  whereas the upright plates do not. Furthermore, the simulations serve to predict and optimize the influence of variations in interplate geometry, scallop grating pitch and shape, and plate tilt angle before the manufacturing of the system.

Further FDTD simulations (Fig. 5.6) show the effect of tilting the plate at different angles, wherein it can clearly be seen that the diffraction pattern doesn't shift, but the increase in intensity of the features therein change as predicted by Eq. 5.2. As the diffraction signature from the scallops is quite weak, a final FDTD simulation was conducted to determine the effect of deeper scallops. Figure 5.7 shows the results of these simulations for three different tilt angles of the plates.

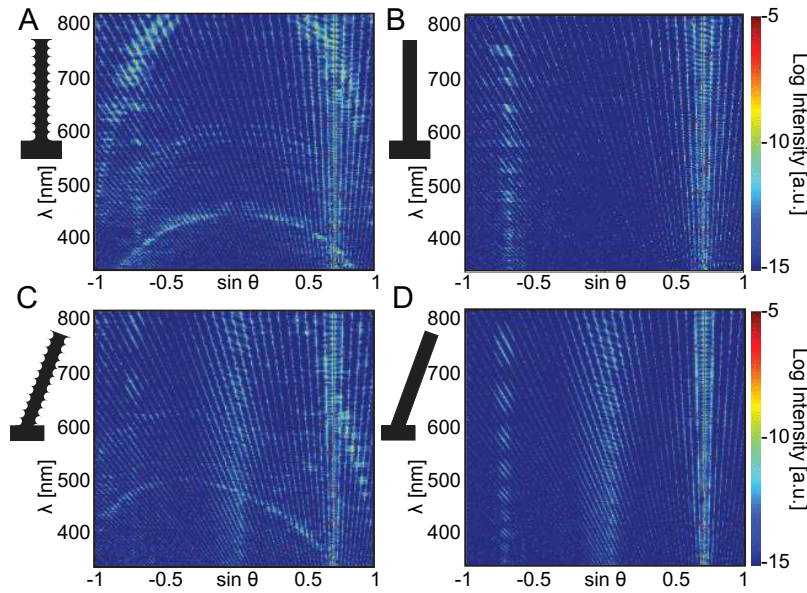


Figure 5.5: Modeling of the expected diffraction patterns originating from the ordered array of gratings with  $45^\circ$  illumination. (A) Calculated diffraction pattern for upright plates with scallops. (B) Calculated diffraction pattern for upright plates without scallops. (C) Calculated diffraction pattern for  $23^\circ$  tilted plates with scallops. (D) Calculated diffraction pattern for  $23^\circ$  tilted plates without scallops.

Whereas the angular positions of the diffraction modes resulting from the interplate periodicity only vary with the angle of light incidence  $\theta_I$ , for a given  $\theta_I$  the diffraction pattern caused by the regular scallops on individual plates is strongly affected by

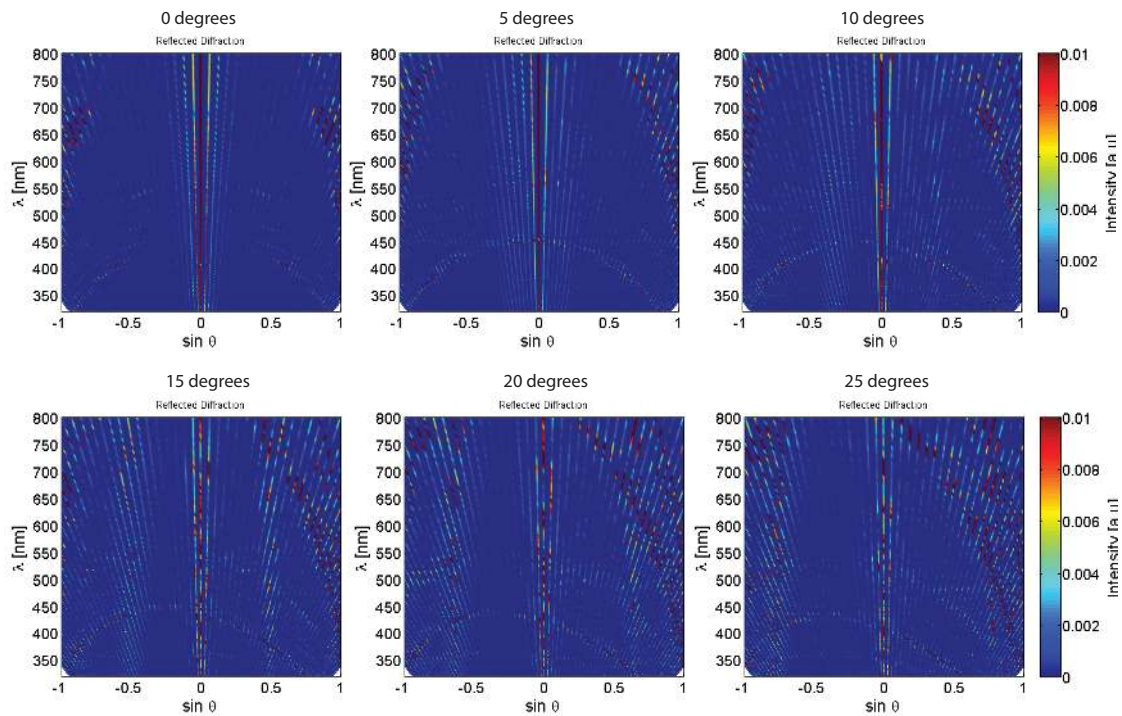


Figure 5.6: Table of simulations in Lumerical showing the diffraction pattern from an array of scalloped plates similar to those in Fig. 5.3 for different tilt angles. The reverse color-order diffraction pattern changes location as predicted by Eq. 5.2.

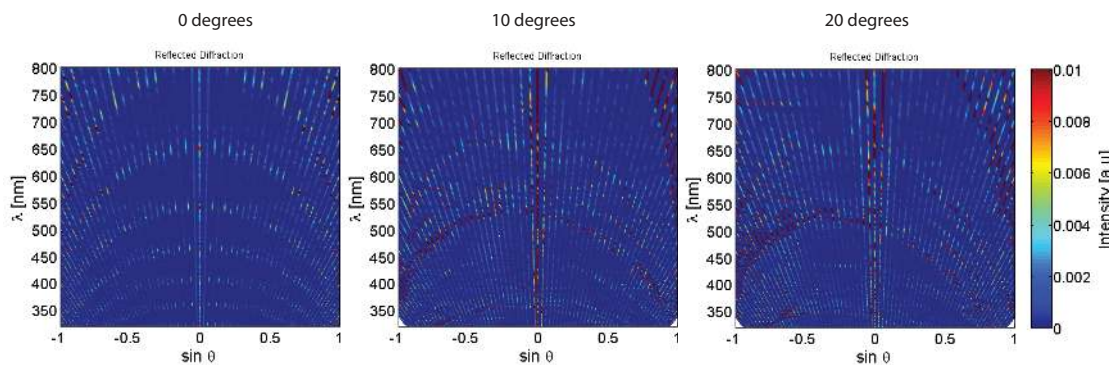


Figure 5.7: Simulations in Lumerical showing the larger number of reverse color-order diffraction orders visible when the depth of the scallops is increased.



a change in tilt of the plates relative to the sample normal. Consequently, a means of reversibly varying the plate tilt angle can provide the possibility to dynamically tune the diffraction pattern independent of light incidence. Possible means of achieving such reversible actuation include embedding the plates in a stimuli-responsive hydrogel [245–248], using a soft material negative of the structure and applying shear force to bend the microgratings, modifying the tips of the plates with ferromagnetic particles to allow for dynamic reconfiguration of the plate geometry using magnetic fields [249], or implementing tuning mechanisms shown for simple planar diffraction gratings that rely on electric fields or mechanical deformation [250–253].

## 5.5 Conclusions and Discussion

Biological strategies for light manipulation have already been successfully implemented in nanophotonic devices for applications in chemically selective vapor sensing, pH determination, infrared imaging, surface-enhanced Raman spectroscopy-based chemical analysis, and localized heating from infrared absorption [254–259]. The rich and tunable optical signature of our hierarchical bioinspired diffraction-based photonic material platform could provide a basis for novel developments in biosensing [260–262], efficient light management in photovoltaic systems [263–265], enhanced light extraction and radiation profile shaping in light-emitting diodes [266–268], and optically variable devices in consumer product design and anticounterfeiting [269–271].

Our results demonstrate the versatility of a bioinspired approach toward the creation of novel photonic systems. The unique diffraction-inducing nano- and microscale architecture previously discovered in the scales of the male butterfly *P. luna* served as inspiration for artificial microdiffraction grating arrays. Our photonic system mimics the reverse diffraction color sequence found in the butterfly’s scales and also provides additional complexity in the diffraction patterns due to a periodic arrangement of the diffraction elements not found in the natural structure. Such arrays provide a platform for hierarchical photonic systems displaying unique diffraction coupling. A detailed optical analysis and modeling of the diffraction patterns allowed us to ob-

serve, understand, and decouple diffraction effects induced by the plate ensemble and by the regular scalloping of individual plates. A variation of the light incidence angle results in the expected shifting of the plate ensemble diffraction modes but does not affect the diffraction resulting from individual plates. On the other hand, a variation in plate inclination leaves the interplate geometry diffraction modes untouched but has a strong influence on the scallop-induced diffraction.

The intensity distribution of the diffraction induced by the scallops is modulated by the diffraction induced by the plate ensemble. Where the scallop diffraction arc coincides with a plate ensemble diffraction order a peak in intensity is observed. A decrease in the plate ensemble period would result in fewer propagating plate ensemble diffraction orders with a larger free angular range in between. This would lead to a discretization of the scallop diffraction pattern (seen in the FDTD simulation in Fig. 5.8) inducing a discrete and easily perceivable color variation with potential applications in the development of novel optically variable devices in security printing and consumer product labeling. Currently, efforts are underway to fabricate the diffraction structures in different material combinations that provide a higher refractive index contrast, thereby strengthening the diffractive signal.

## 5.6 Materials and Methods

### 5.6.1 Manufacture of artificial diffraction structures

When Bosch etching [241] is used in conjunction with photolithography, the multiple etching and passivation steps give rise to a periodicity in the sidewall of the structures due to the repeated underetching. Although typically the goal of this etching method is to create vertical sidewalls, these undulations in the sidewall can form a diffraction grating similar to that on the *Pierella luna* scales if the periodicities are chosen to fall within the range of optical wavelengths.

Once structures with the correct geometry are created in silicon, they can be replicated in other materials with better optical properties by using soft lithographic methods [240]. By using soft, transparent materials instead of silicon, the structures

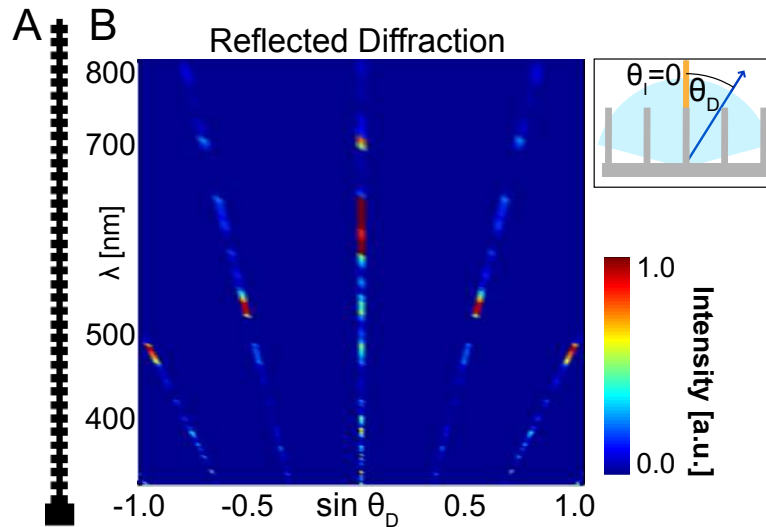


Figure 5.8: Diffraction discretization. (A) One-m-wide unit cell for diffraction grating simulated via FDTD. (B) Reflected spectra calculated from FDTD simulation of A showing bright spots in each diffracted order with discrete jumps in the diffracted wavelength.

can be bent much more easily and the optical properties can be changed by applying metal coatings or doping the material with pigments or other materials with interesting optical properties. The replication is achieved by using a PDMS mold of the silicon master and curing an epoxy via UV light before removal from the mold.

### 5.6.2 Structural and optical analysis

Once scalloped plate structures are made, optical characterization is performed for comparison of the structures observed on *Pierella luna* and the fabricated systems. Several different types of characterization were used, including variable-angle spectroscopy, diffraction microscopy, and SEM. For the variable-angle spectrometry setup, an Ocean Optics DH-2000 ultraviolet-visible-near infrared light source was used to illuminate a small spot ( $\approx 1$  mm) of the sample at a given incidence angle  $\theta_I$ . For each angle of illumination, light was collected at half-degree increments for  $-75^\circ$  to  $+75^\circ$  relative to the sample normal and spectrally analyzed using an Ocean Optics Maya Pro-2000 spectrometer. For the diffraction microscopy images, a Bertrand lens was

used to focus on the back focal plane of the objective of an upright BXFM Olympus optical microscope. The sample was illuminated either from an external source oriented at a  $90^\circ$  angle to the microscope objective with a spot size larger than the sample field of view, or with a small-diameter optical fiber coupled into the microscope light path (Littrow mounting). SEM images were taken on a Zeiss Ultra55 or a Zeiss Supra55VP SEM after coating the polymer structures with a thin layer of gold to prevent charging.

### 5.6.3 Optical modeling

FDTD [272] methods were used to numerically simulate the results obtained from the variable-angle spectroscopy measurements. A commercial-grade simulator based on the FDTD method was used to perform the calculations [273]. Perfectly matched layers [274] were used to prevent reflections from the top and bottom of the simulation cell, whereas Bloch boundary conditions were used for the sides of the simulation cell to model light scattering from a periodic array at nonnormal incidence. To simulate broadband angled scattering, each simulation was repeated for a range of Bloch wavevectors, which were combined to produce scattered field profiles corresponding to an incidence angle of  $45^\circ \pm 1^\circ$  for wavelengths of 320-800 nm. Far-field projections of the calculated local fields resulted in diffraction patterns (Fig. 5.5) analogous to the variable-angle spectroscopic data. The diffraction discretization FDTD simulation was similarly performed in MEEP, a free FDTD software [244]. The use of normal incidence illumination for this simulation allowed all frequencies and angles to be calculated without using a sweep of incidence angles.

Page intentionally left blank

# Chapter 6

## The Optical Janus Effect: Asymmetric Structural Color Reflection Materials

This chapter discusses an example, as introduced in Chapter 4, of absorption localized within a structurally colored material. The concentration of the absorption within a Bragg stack or thin film architecture changes the boundary conditions of the structure such that the classical multilayer- and thin film interference equations no longer predict the correct color for the structure. Additionally, the anomalous phase change upon reflection from the highly absorbing layer within the structurally colored material allows for an asymmetric reflection color to be observed in these types of materials.

### 6.1 Overview

For thousands of years, humans have been fascinated with the panoply of colors found in nature, and have sought to create materials that exhibit these colors in a variety of ways. Throughout this time, there has been continual improvement in the ability to fabricate and understand the underlying physics of these structures, from the 4th century Roman Lycurgus cup [275], showing different color in reflection

and transmission, to the inspiring coloration of ancient church windows [276], and modern effect pigments [277] that use sparkle, luster and color travel to create vivid coloration. Aesthetics and function are often intimately linked in modern materials [278]. Examples can be found in materials that change color to indicate structural fatigue in bridges, buildings, or airplane wings [279] or modify transparency to allow for energy savings [280], as well as in the fields of anti-counterfeiting [154, 196], solar energy harvesting, modulation of absorption and thermal emission [175, 176, 281, 282], and colorimetric sensing. [111, 146] Generally, the coloration of a material results from a combination of absorption, reflection, and scattering. Absorption of light in a given wavelength range leads to a macroscopic color; for example, by electronic excitations in dyes or plasmonic resonances in noble metal nanoparticles. [99, 283] Alternatively, micro-to-nano-scale structured materials can enable optical interference phenomena, resulting in structural coloration. Examples of structural coloration abound in natural species [74, 284, 285], and can also be found in synthetic photonic structures such as diffraction gratings [154, 286], colloidal crystals [5, 287], and multi-layer stacks [288, 289]. The combination of structural coloration and absorption can improve color saturation and create entirely novel color effects. In the simplest case, absorbers-whether dyes or plasmonic absorbers-are used to purify the spectrum of structurally colored materials, especially by distributing an absorber homogeneously throughout the material. [12, 14, 15, 98] More importantly, the controlled localization of the absorbing moieties within a composite architecture can provide avenues for completely new optical effects. The potential of achieving surprising optical effects from rationally designed combinations of absorbing and dielectric material has been demonstrated in several systems, including ultra-thin perfect absorbers [180], ultra-thin-film semi-conductor/metal structural color materials [176], anti-reflective coatings [290], structural color saturation adjustment [189], and asymmetric reflection materials [171, 172, 174, 195]. Strikingly, asymmetric absorption properties can arise from the combination of an absorbing layer with a thin film. In particular, Butun and Aydin have demonstrated asymmetric absorption properties at specific wavelengths in a metamaterial with precisely controlled plasmonic properties by combining two structural color elements (a thin film and a plasmonic metamaterial) with an ab-

sorbing layer (a film of silver). [172] A material with such an asymmetric absorption spectrum, by conservation of energy, must have an asymmetric reflection spectrum; by generalizing the system of a structural color material and an absorbing layer which can impart an anomalous phase shift (one different from 0 or  $\pi$ ) on the reflected light, we can rationally design the reflected color from one side of the material to be arbitrarily different from the reflected color from the opposite side. Here, we take advantage of the anomalous phase shift upon reflection from an absorbing material interface to create semitransparent coatings that exhibit different reflected colors depending on the viewing direction. In analogy to Janus particles [291] that feature different chemical compositions on either side, we will refer to these materials as optical Janus materials to highlight the asymmetric nature of their reflection. We investigate the underlying physical origin of the observed effect, provide general design guidelines to create coatings with arbitrary reflection colors from each side, and use patterning techniques to create optical Janus patterns with viewing direction-dependent optical properties.

## 6.2 Janus Thin Films

We fabricate optical Janus thin films using gold nanoparticles ( $d \sim 12\text{nm}$ ) as an absorbing element in combination with a titania thin film used as the photonic element causing thin film interference. We adsorb gold nanoparticles electrostatically via a silane linker onto a transparent glass slide onto which we deposit a titania thin film ( $d = 228\text{nm}$ ) via sputter coating (supplementary information). The small size of the nanoparticles and the non-directional deposition via sputter coating enables us to embed the nanoparticles without compromising the properties of the titania thin film used as the photonic element. In Figure ??, we compare the viewing direction-dependent optical properties of the thin film to a reference sample without any absorbing gold nanoparticles and a sample with gold nanoparticles deposited at the air/titania interface. As expected, the color observed from either side of the thin film without an absorbing material is identical (Fig. 6.1a), whereas that observed on



the sample with the absorbing layer between the substrate and the dielectric shows a strong difference in the color observed from either side (Fig. 6.1b). The sample appears a bright cyan color when viewed from the film side and a violet color when viewed from the substrate side. The drastic difference between the color observed in these two configurations is further emphasized by the measured reflectance spectra for the two reflectance measurements (dashed lines, Fig. 6.1 b). If the gold nanoparticles are deposited at the air/titania interface, the main difference observed in the color of each side is in the reflected intensity of the spectrum, but not the location of the peak and trough wavelengths (Fig. 6.1c). As we outline in detail below, the complex refractive index (RI) of the absorbing layer is the main origin of the optical Janus effect, which can therefore be observed for different absorbing materials. When noble metal nanoparticles are used, this complex RI is very sensitive to their dielectric environment. [283] Thus, the optical properties can be controlled via the position of the absorbing layer within the composite photonic structure. The three fundamental configurations shown in Fig. 6.2 demonstrate the key parameters in designing coatings with asymmetric structural coloration: the presence of an absorbing element, its position relative to the other optical elements, and its complex refractive index.

### 6.3 Theory

We attribute the observed asymmetric reflection properties to the anomalous phase shifts occurring upon the reflection from an absorbing layer as predicted by the Fresnel reflection coefficient for normal incidence shown below. [292]

$$r_{1,2} = \frac{\tilde{n}_1 - \tilde{n}_2}{\tilde{n}_1 + \tilde{n}_2} \quad (6.1)$$

Where  $\tilde{n}_1$ ,  $\tilde{n}_2$  are the complex RIs of the incident and reflecting media, respectively, with the imaginary part of the RI representing the loss or gain of the material. For non-normal incidence, these coefficients are different for the transverse electric and transverse magnetic polarizations; for simplicity, we assume normal incidence for all calculations. It can easily be seen that when there is no absorption, the Fresnel

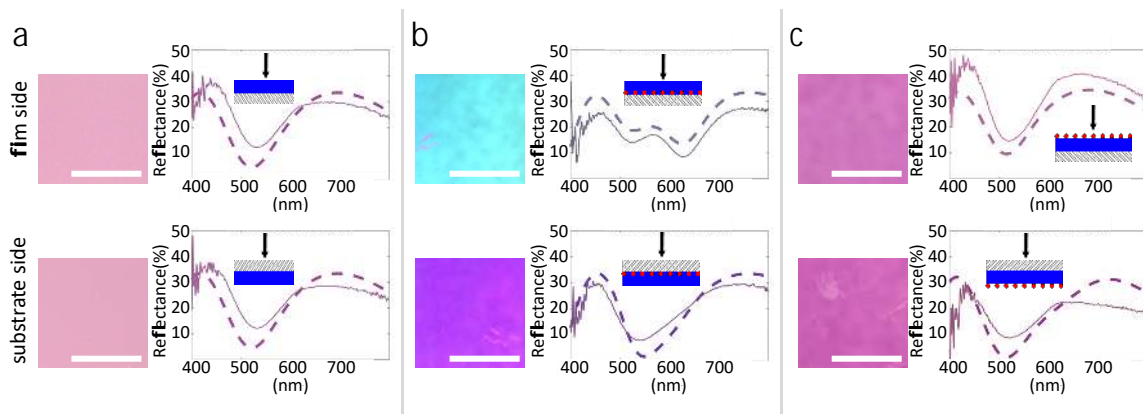


Figure 6.1: The optical Janus effect observed in a thin film architecture. a. (film side) Photographic image (left) of a titania ( $\sim 218\text{nm}$ ) thin film on a glass substrate, with simulated (dashed) and measured (solid) reflectance spectra (right), measured from the film side of the sample. The illustration between the two images shows the sample configuration and observation direction. (substrate side) Same as above, but for the sample measured from the substrate side of the sample. b. Same as (a) but for a thin film containing gold nanoparticles located at the substrate/thin film interface (shown as red circles in the illustration). c. Same as (b) but with the nanoparticles located at the air/thin film interface. All scale bars are 1cm .

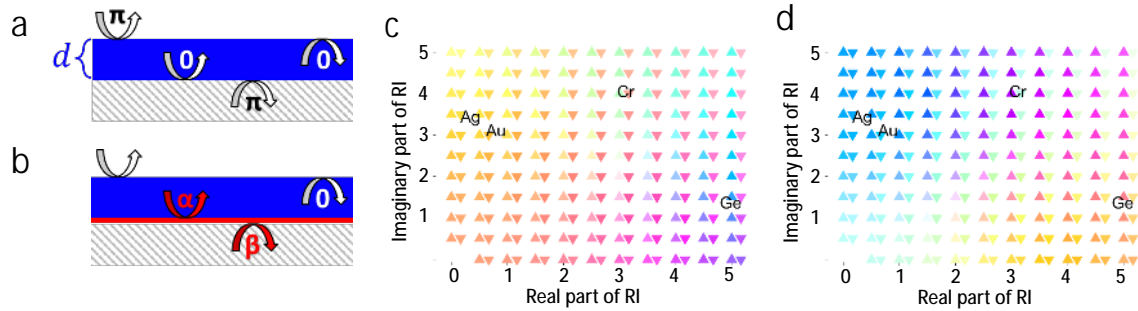


Figure 6.2: Structural origin of the optical Janus effect. a-b. Schematic showing the anomalous phase shift upon reflection from a thin absorbing layer (red) in a thin film material (blue) on a transparent substrate (hatched). The refractive index (RI) of the thin film material is assumed to be higher than that of the substrate. a. Illustration showing the phase changes of  $0$  and  $2\pi$  upon external and internal reflections of a dielectric layer. b. Same as (a) but for a dielectric film deposited on an absorbing layer showing anomalous reflection phase changes from the absorbing interfaces. c. Results of an array of transfer matrix simulations for a 200 nm thin film of Titania (RI=2.45) with a 7 nm absorbing layer at the bottom on a glass substrate for various real and imaginary parts of the RI of the absorbing layer. The triangle pointing up is displayed with the simulated human-eye perceived color as observed from the film side of the sample, while the triangle pointing down is the same for the sample observed from the substrate side. d. Same as (c) but for a thin film of SiN (RI=1.95). The average real and imaginary RIs over the visible spectrum of different absorbing materials are inserted into the diagram.

coefficient will be purely real, and therefore will cause either a 0 or  $\pi$  phase change in the reflected light (Fig. 6.2a). However, when one or both of the media have complex RIs, the Fresnel reflection coefficient becomes complex, and therefore imparts an anomalous phase shift (deviating from 0 or  $\pi$ ) on the reflected light, as shown in Figure 6.2b. In a conventional thin film (Fig 6.2a) without any absorbing elements, a  $\pi$  phase shift (half a wavelength) occurs at the first interface regardless of which direction is being illuminated; provided that the RI of the thin film is higher than that of the substrate. Within the film, there will be no phase shift for the internal reflections. Thus, while the light can reflect off the internal surface any number of times, the total phase accumulated for a given path is the same regardless of the incident direction: the reflected structural color observed from either side of the material is identical. In the presence of absorbing elements, the phase shift will not follow the simple trend as described before. Depending on its complex refractive index and the RIs of the surrounding materials, a phase change in between 0 and  $\pi$  will be observed upon reflection from the absorbing layer(Figure ??e). Since the RIs of the materials on either side of the absorbing layer are different, the accumulated phase is no longer the same for light incident from either side of the structure and we can expect to see the optical Janus effect (see Supplementary Information for a derivation of the analytical calculations of the effect). From these simple arguments, we calculate the strength of the optical Janus effect based on the anomalous phase changes upon reflection from thin film ( $\alpha$ ) and substrate side ( $\beta$ ). We use the transfer matrix method and vary the real and imaginary part of the RI of the absorbing layer, which we model as a thin absorbing layer placed underneath the photonic thin film structure. [292] Figure 6.2c-d shows exemplified analytical solutions for thin-film structures made of titania (Fig. 6.2c) and silicon nitride (Fig. 6.2d) each of which has a thin absorbing layer (7 nm) at the substrate/thin-film interface with varying complex RIs. The triangle pointing up is colored with the simulated human-eye perceived color as observed from the film side of the sample, while the triangle pointing down is the same for the sample observed from the substrate side. The strongest structural color asymmetry, i.e. the biggest color change for different viewing directions, can be observed for high real and imaginary parts of the RI of the absorbing element. These analytical cal-

culations explain the dependence of the observed optical Janus effect on the position of the absorbing element shown in Figure 6.1a-c. If the absorbing gold nanoparticle layer is positioned at the air/thin-film interface, the surrounding material occupying most of the physical volume of the layer is air, so the real part of the effective RI of the absorbing layer is low. Moreover, the localized surface plasmon resonance of gold nanoparticles experiences spectral shifts when they are surrounded by a lower index material-causing a blue-shift and a decrease in intensity of the absorbance peak-which lowers the imaginary part of the RI of the absorbing layer. [292] Both effects weaken the optical Janus effect and cause similar reflection colors to be observed from either side of the sample, as observed in Fig. 6.1c. In contrast, placing the gold nanoparticle layer in between the substrate and the dielectric film will increase both the real and imaginary part of the effective RI of the absorbing layer, leading to a pronounced structural color asymmetry (Fig. 6.1b).

## 6.4 Multilayer Janus Stacks

Coatings with asymmetric color reflection are not limited to thin films but can also be prepared from multilayer architectures, allowing for an increase in overall reflectivity and more control of the optical spectra. Incorporation of a gold nanoparticle layer into the high RI part of the multilayer structure provides a strong optical Janus effect with a pronounced dissimilarity of observed color depending on the viewing direction (Fig. 6.3 a-b). Similar to the thin film architecture, a multilayer without an absorbing layer always shows the same color when observed from both sides (Fig. 6.3c). When changing the location of the nanoparticles within the multilayer, the effect can be enforced or diminished, depending on the RI of the layer embedding the absorbing nanoparticles (Supplementary Information).

## 6.5 Patterning of Janus Films

In Figure 6.4, we show micron-scale structures with controllable, viewing direction-dependent optical properties by controlling the spatial patterning of the absorbing

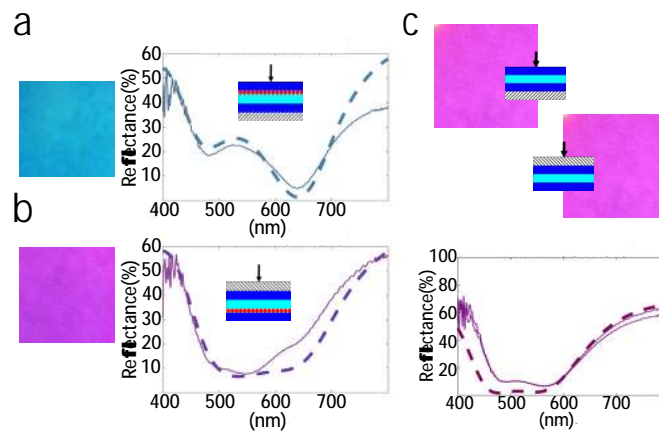


Figure 6.3: The optical Janus effect observed in a multilayer stack a. (left) Photographic image of a titania/silica/titania ( $n=2.45/1.45/2.45$ ) 3-layer multilayer with absorbing gold nanoparticles between the 2nd and 3rd layers measured from the film surface. Thicknesses of the layers are all 100nm. (right) Simulated (dashed) and measured (solid) spectra of the sample viewed from the coating side. b. Same as (a), but viewed from the substrate side. c. Photographic images (top) of a sample containing no gold nanoparticles with the same layers as (a-b) on a glass substrate, with simulated (dashed) and measured (solid) reflectance spectra, measured from both sides of the sample (bottom). The optical properties are identical from both viewing directions. All scale bars are 1cm.

elements using photolithographic techniques. We deposit a thin gold film on a photolithographic pattern and apply a lift-off technique to remove the gold film from pre-patterned structures. A dewetting process at 500°C subsequently transforms the gold film into separated nanoislands [293] at predefined areas (Fig. 6.4a-b). After deposition of a multilayer structure as the photonic element, the nanoparticle-coated areas exhibit the optical Janus effect, while all other areas do not show asymmetric color properties due to the absence of the absorbing element (Fig. 6.4c-d): the color of the predefined pattern in Fig. 6.4c-d changes from orange to green color when viewed from the film side and substrate side, respectively, while the background remains uniformly yellow. A slight modification of the deposition process yields even more complex optical microstructures: when omitting the lift-off step, the photoresist layer is combusted during the dewetting process of the thin gold film. This leaves gold nanoparticles on both areas with and without photoresist. Importantly, a small gap without gold nanoislands remains at the edge between the two areas (Fig. 6.4e-f), providing a clear contrast in the structures shown in Fig. 6.4g-h.

The optical Janus effect can be created using absorbing elements with a large range of complex RIs, as indicated in Figure 6.2c,d. By overlaying the complex refractive index of commonly used metal films into the diagrams, we predict that plain metal films used as absorbing element, e.g. chromium or germanium, can produce strongly asymmetric coloration, enabling simple, scalable and cost efficient fabrication processes. Exemplarily, in Figure 6.5a-b we show a patterned optical Janus stack comprised of two bilayers of  $SiO_2/SiN$  on top of a patterned chromium film on a glass slide. Similar to the gold nanoparticles used above, the large complex refractive index of a chromium thin film induces anomalous phase shifts upon reflection, giving rise to the observed structural color asymmetry. In the example, the structure was designed such that when viewed from the coating side, the pattern would be similar in color to the surrounding Bragg stack color without the absorbing layer, while when viewed from the substrate side, there would be a strong contrast in color between the pattern and background. This creates a viewing-direction selective invisibility of the pattern. An even more complex optical Janus effect is achieved by varying the thickness of the first layer deposited on top of the absorbing layer. Designing the

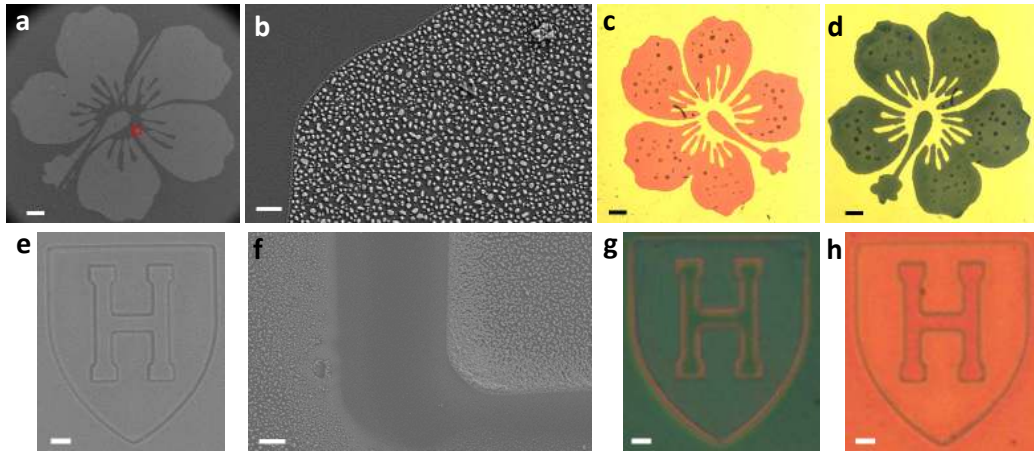


Figure 6.4: Spatially patterned optical Janus properties by local control of absorber deposition. a. SEM image of a single pattern showing the locations of the nanoparticles (bright areas). b. Higher resolution SEM image of the boxed region in (a) showing the nanoparticle size distribution. c. Optical micrograph of the coating side of a patterned layer of gold nanoislands created using the method described in the text. d. Optical micrograph of the same sample viewed from the substrate side e-h. Same as (a-d) but for a sample made without the lift-off step, such that the gold nanoislands are located everywhere except for the edge of the micropattern. The entire sample shows asymmetric structural color (view from coating side shown in (g); view from substrate side shown in (h)), with the contrast giving by the small regions along the lines of the pattern that do not feature any nanoparticles (f). Scale bars: a,c-d, 400 nm; b, 1  $\mu$ m; e,g-h, 10  $\mu$ m; f, 1  $\mu$ m.



Bragg stack in such a way that its peak wavelength is near the middle of the visible spectrum, we create a sample with nearly uniform coloration when viewed from the front side, while displaying a range of colors when viewed from the substrate side. (Fig. 6.5c-d)

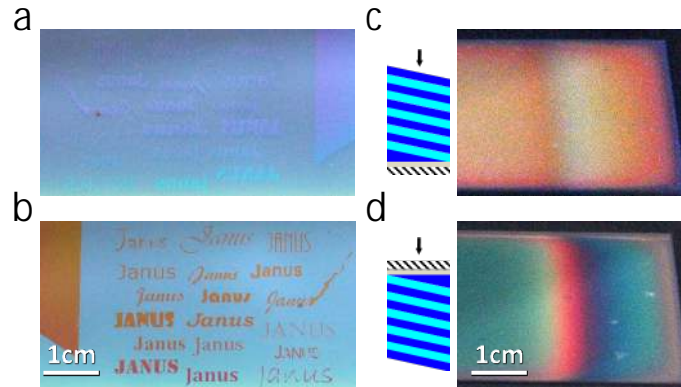


Figure 6.5: Viewing direction dependent optical effects from Janus coatings using a thin metal film as the absorbing element. a,b. Partially invisible Janus color patterns a. Photograph of the coating side surface of a micro-patterned asymmetric structural color stack with 3 bilayers of  $\text{SiN}/\text{SiO}_2$ , a defect layer of  $\text{SiN}$ , and a 7 nm thin film of patterned chromium designed to match colors of the features and the background from the coating side and thus hide the pattern. b. Photograph of the substrate side surface of the sample in (a) showing a high contrast between the color in the regions containing chromium and the color of the simple Bragg stack. c,d. Viewing direction dependent polychromaticity from gradient thickness optical Janus films. c. Photograph of the structure with 5 bilayers of  $\text{SiN}/\text{SiO}_2$ , a gradient-thickness layer of  $\text{SiN}$ , and a 7 nm thin film of chromium showing a near solid orange color when viewed from the coating side. d. Same sample, but photographed from the substrate side, revealing a rainbow pattern in the region of the thickness gradient.

## 6.6 Methods

### 6.6.1 Nanoparticle Synthesis

A stock solution of citrate-stabilized gold nanoparticles was prepared according to a modified literature procedure. Sodium citrate (50 mg, 0.17 mmol) was added to

a refluxing, vigorously stirred solution of sodium tetrachloroaurate dihydrate (25 mg, 0.065 mmol) in DI water (125 mL). The mixture was stirred under reflux for 15 min and then allowed to cool to room temperature. The initially yellow solution changed to deep red and was stored in a glass bottle protected from light.

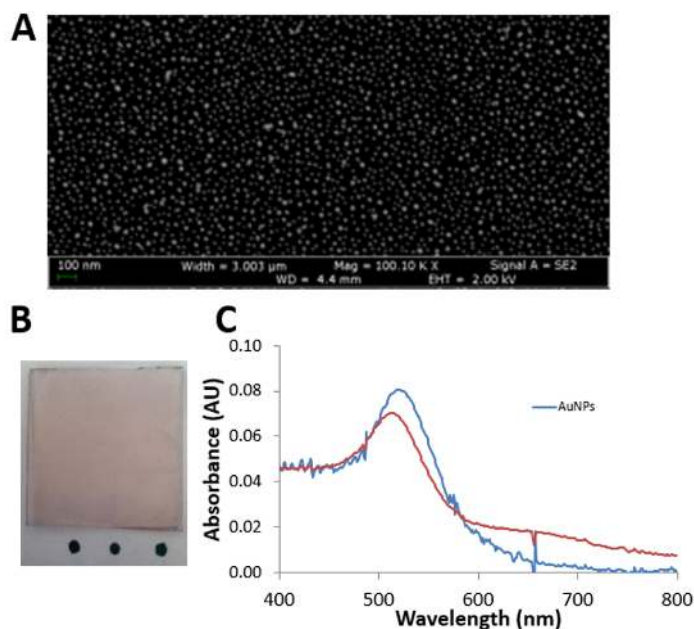


Figure 6.6: A. SEM image of gold nanoparticles. B. Optical image of a  $\sim 1$ in square glass slide functionalized with plasmonic gold nanoparticles. C. Absorbance spectra of gold nanoparticles in solution (blue) and functionalized on glass (red)

## 6.6.2 Nanoparticle Binding

Snow-jet cleaned and piranha or plasma activated glass and silicon samples were submerged in an acetone solution of aminopropyl tri-chlorosilane (5% v/v) for 30 min, then rinsed with acetone, ethanol, and water, and subsequently dried at 130 °C for 10 min. Then, the samples were placed in the aqueous solution of gold nanoparticles for three hours and finally rinsed with water, leaving a monolayer of gold nanoparticles attached to the substrate.

### 6.6.3 Bragg Stack Formation

#### Sputter-Coating

Clean glass slides (with or without nanoparticles) were placed in a 3-target sputter coater (AJA International) and pumped down to 1e-6 torr before sputtering either  $TiO_2$  or  $SiO_2$ . For each layer in the designed Bragg/Janus stack, the process was repeated.

#### CVD-Coating

An STS- plasma-enhanced chemical vapour deposition (PECVD) from Surface Technology Systems (STS) was used to create Bragg/Janus stacks more quickly. Silicon dioxide ( $n=1.45$ ) was deposited by flowing  $SiH_2 + N_2O$  gas; silicon nitride ( $n=1.9$ ) was deposited by flowing SiH, and  $N_2$  gas.

### 6.6.4 Nanoparticle Functionalization / Patterning

#### Photolithographic Patterning

Photolithography was performed in an ISO class 5 clean room at CNS, Harvard. Glass slides were cleaned with acid piranha (3:1 30%  $H_2O_2:H_2SO_4$  @200°C) for 30 minutes, and then rinsed with ethanol. Shipley S1805 positive photoresist was spin coated on the sample at 2000 rpm for 45 s and hard baked at 110 °C for 60 s, giving a protective layer thickness of 2 m. Chrome masks were designed with AutoCAD 2014 and printed using a Heidelberg DWL 66 mask writer. Using a Suss MJB4 mask aligner, softcontact (1.3 bar) was established between the chrome mask and the coated sample. Exposure time was calculated by dividing the exposure dose  $E_0$  (180 mJ cm<sup>-2</sup> for S1805) by the h-line intensity (405 nm) of the MJB4 mask aligner. Standard exposure time was 1.5 s.

#### Nanoparticle Creation by Dewetting Gold Thin Films

For the method of creating nanoparticles from a gold film, a thin film of gold (4-12nm) was evaporated using a Denton electron beam evaporator. If the photoresist

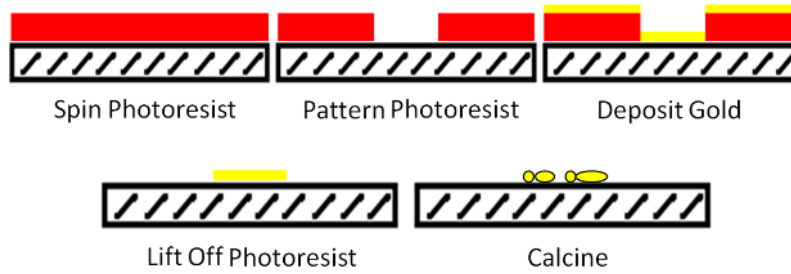


Figure 6.7: Method of creating patterned gold nanoparticles in situ on the sample surface

was desired to be removed, RPG solution was used to remove the crosslinked resist and leave behind a patterned gold film. Next, the sample was placed in a calcining furnace which increased the temperature slowly to 500 °C over 5 hours and held it at that temperature for 2 hours in order to dewet the gold film from the substrate and create gold nano-islands with the desired plasmonic properties. Finally, a Bragg stack was deposited on the substrate using the method described above in order to create a Janus stack.

## 6.6.5 Optical Characterization

### Reflection Spectra Measurement

A Leica microscope with a 50/50 coupler port was used to collect normal incidence reflection spectra for all samples. An optical fiber was coupled into the output port and connected to an Ocean Optics Maya 2000 spectrometer to collect signal from each sample. The raw intensity data was corrected for the dark current of the spectrometer and the intensity distribution of the halogen light source to calculate the reflectance spectra.

### Simulation

A transfer matrix simulation was used to determine the theoretical reflectance spectrum for each side of the Janus stacks for comparison between theory and experiment as well as to design different color combinations before fabricating the Janus

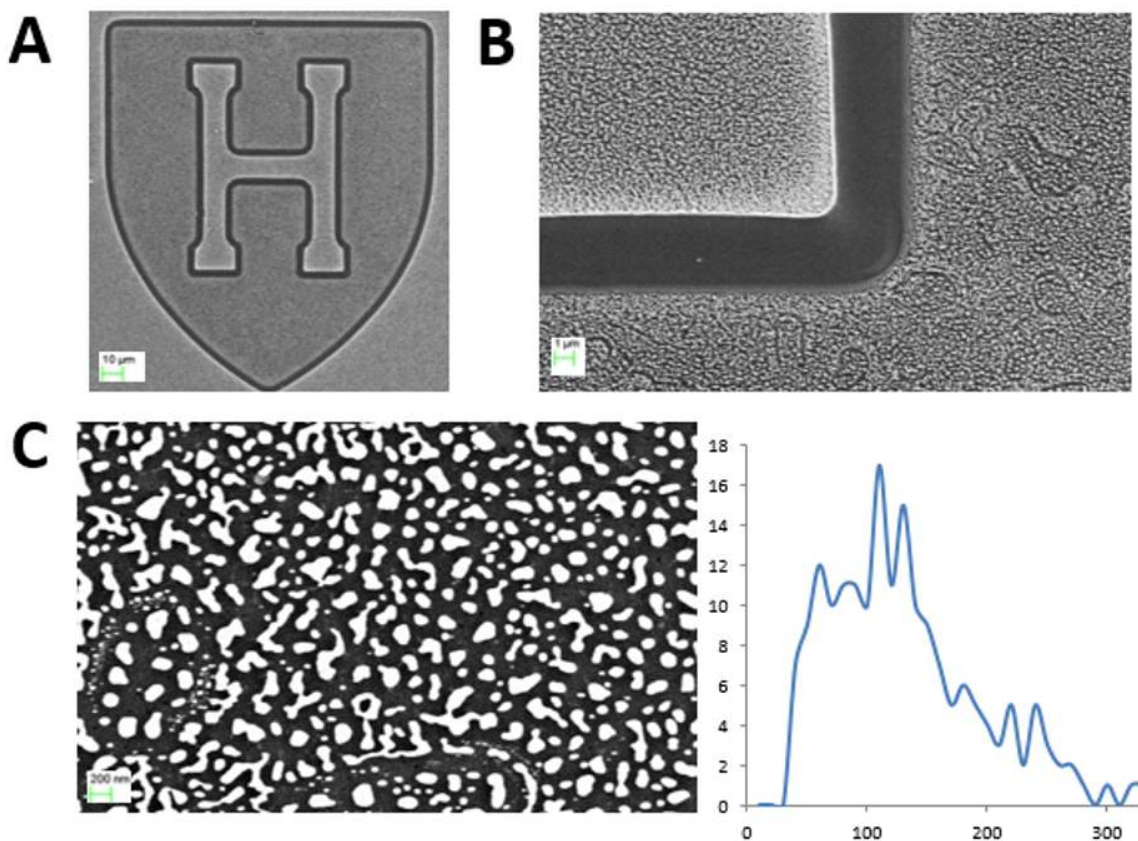


Figure 6.8: Gold nanoparticle size distribution for 6nm gold film. A. SEM image showing a patterned area of gold nanoparticles (scale bar 10m). B. Higher-magnification SEM image of one of the corners of the "H" in (A) (scale bar 1m) C. Higher magnification SEM image (scale bar 200nm) (left) and nanoparticle size distribution calculated from the image showing the sizes of the nanoparticles (right) ( $125 \pm 63\text{nm}$ )

stacks. For this calculation, the complex refractive index and thickness of each layer as well as that of the substrate is required. All materials other than the absorbing layer are assumed to have purely real and nondispersive refractive indices. For the samples containing synthesized gold nanoparticles, the absorbing layer is simulated as a 20 nm thick layer having a complex refractive index with the real part equal to the refractive index of the material surrounding the nanoparticles and the imaginary part a Gaussian function centered at 560 nm with a standard deviation of 70 nm and a magnitude determined by fitting to the experimental data. For the samples containing gold nanoislands, the standard deviation is much higher, and sometimes two Gaussians are used to account for the spread in the absorption resonance of the differently sized and shaped nanoparticles. For the samples using only a thin film of metal, the complex wavelength-dependent refractive index of the metal as reported in literature is used. Similar results are obtained when a commercial software is used to calculate the reflection spectra of the simulated and experimental samples.

For calculation of the reflectance spectra from both sides of the Janus stacks, the following procedure was followed.

$$T_{ij} = \frac{1}{t_{ij}} \begin{pmatrix} 1 & r_{ij} \\ r_{ij} & 1 \end{pmatrix} \quad (6.2)$$

$$P_i = \begin{pmatrix} e^{ik_z d_i} & 0 \\ 0 & e^{-ik_z d_i} \end{pmatrix} \quad (6.3)$$

Where, for normal incidence,

$$r_{ij} = \frac{n_i - n_j}{n_i + n_j} \quad (6.4)$$

$$t_{ij} = 1 + r_{ij} \quad (6.5)$$

From these, if we have a stack with N layers with each layer, i, having refractive index  $n_i$  and thickness  $d_i$ , and assuming that  $n_0$  is the refractive index of air:

$$R_{TOP} = (\prod_{i=0}^{N-1} T_{i,i+1} P_{i+1}) T_{N,substrate} \quad (6.6)$$

$$R_{BOTTOM} = T_{substrate,N} (\prod_{i=N}^2 T_{i,i-1} P_{i-1}) T_{1,0} \quad (6.7)$$

It should be noted that these values must be calculated for each wavelength ( $k_z = 2\pi/\lambda$  for normal incidence) and in general the refractive index of each layer is a complex function of the wavelength. Once the reflectance spectra for a sample was calculated, the CIE 1932 color matching functions were used to generate RGB values corresponding to the color of that spectrum for macroscopic visual comparison of the samples. Typical values for the absorption properties of the gold nanoparticles were:  $\lambda = 560\text{nm}, \sigma = 70\text{nm}, A = 0.2$ .

## 6.7 Derivation of First Order Approximations

### 6.7.1 Thin Film

#### From the top side

Taking the reflections which have taken some number of round trips within the dielectric, we have a phase change accumulation of:  $\pi, 2D, 4D, \dots$  (where  $D = 2\pi nd/\lambda$ ,  $n$  is the refractive index of the material,  $\lambda$  is the wavelength, and  $d$  is the thickness of the film). To calculate the wavelengths for which constructive interference occurs, we set the first two of these terms to be equal (allowing for a multiple of  $2\pi$  shift in between):

$$\pi + 2\pi m = 2\left(\frac{2\pi nd}{\lambda}\right) \quad (6.8)$$

Solving for  $\lambda$ , we have:

$$\lambda = \frac{2nd}{m + \frac{1}{2}} \quad (6.9)$$

#### From the bottom side

We again have a  $\pi$  phase shift at the first interface. Again, taking the phase change accumulation from this first reflection, and for the rays which have taken an integral number of round trips within the dielectric, we have phase change accumulations of:  $\pi, 2D, 4D, \dots$ . So, we arrive at the same expression as above, and we should observe the same structural color regardless of which side of the film is being observed.

**For a thin film with a lower refractive index than the substrate**

Here the accumulated phases from the two sides are  $\pi, 2D+\pi, 4D+2\pi, \dots$  and  $0, 2D, 4D + \pi, \dots$ . So, we can see that there is a difference of  $\pi$  between the two sides for all light paths, which will have no effect on the interference conditions.

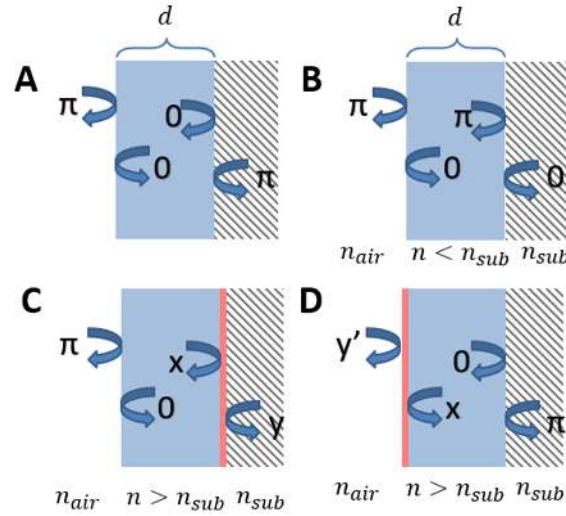


Figure 6.9: Schematic showing the anomalous phase shift upon reflection from a thin absorbing layer (red) in a thin film material (blue) on a transparent substrate (hatched). The refractive index of the thin film material is assumed to be higher than that of the substrate. A. Cartoon showing the phase changes upon external and internal reflections of a dielectric layer. B. Same as (A) but for a thin film with a lower refractive index than the substrate. C. Same as (A) but for a dielectric film deposited on an absorbing layer showing anomalous reflection phase changes from the absorbing interfaces. D. Same as (B), but with the absorbing layer on top of the dielectric.

**6.7.2 Absorbing layer between the dielectric and the substrate**

**From the top side**

Using section 6.7.1 above as a model, we take the reflections which have taken some number of round trips within the dielectric. For this case, we have a phase change accumulation of:  $\pi, 2D + x, 4D + 2x, \dots$  (where  $x$  is the phase change upon reflection from the absorbing material as shown in Fig 6.9B). To calculate the



wavelengths for which constructive interference occurs, we set the first two of these terms to be equal (allowing for a multiple of  $2\pi$  shift in between):

$$\pi + 2\pi m = 2\left(\frac{2\pi nd}{\lambda}\right) + x \quad (6.10)$$

Solving for  $\lambda$ , we have:

$$\lambda = \frac{2nd}{m + \frac{1}{2} - \frac{x}{2\pi}} \quad (6.11)$$

### From the bottom side

Here, the initial reflection is from an absorbing layer, so we have an unknown phase change (labeled as "y") for our initial reflection. If we again assume the absorbing layer thickness to be negligible, and take the reflections which have taken some number of round trips within the dielectric, we have a phase change accumulation of:  $y, 2D, 4D + x, \dots$ . To calculate the wavelengths for which constructive interference occurs, we set the first two of these terms to be equal (allowing for a multiple of  $2\pi$  shift in between):

$$y + 2\pi m = 2\left(\frac{2\pi nd}{\lambda}\right) + x \quad (6.12)$$

Solving for  $\lambda$ , we have:

$$\lambda = \frac{2nd}{m + \frac{y}{2\pi}} \quad (6.13)$$

Comparing this with equation 6.11, we can see that the locations of the peaks for these two different situations can be very different. However, it should be noted that if  $x=0$  and  $y=\pi$ , we recover the expression from section 6.7.1.

### 6.7.3 Choosing a different "cavity"

For these approximations, we used the reflections within the "cavity" of the dielectric. Another choice we could have made was to select this "cavity" as the dielectric and the absorbing layer as a single entity. For this approximation, we need to use the Fresnel equations to determine that the value of the phase changes  $x, y, x'$ , and  $y'$  from the other side of the same interface are off by a  $\pm\pi$  phase shift. Also the thickness of the absorbing layer,  $d_a$ , and the real part of the refractive index of

the absorbing layer,  $n_a$ , should be taken into account. With this selection we come to slightly different equations for the locations of the peaks from the top and bottom side, that can be seen in Table 6.1 below. The new approximations for this larger "cavity" are very similar when you compare the top and bottom reflection peak locations. If we consider that a non-absorbing material has  $x=0$  and  $y=\pi$ , we can see that the case for the absorbing layer on top of the dielectric will have very little difference.

### 6.7.4 Summary of Approximations

Solving the expressions for the peak wavelengths using the dielectric as the cavity such that they are in the same positions for measuring the reflectance from the top and from the bottom surface gives the simple expressions  $x+y=\pi$  and  $x+y'=\pi$ . From this, we can conclude that there will be a weaker Janus effect when these conditions are met or almost met.

Absorbing Layer	No Abs. Layer	Abs. Layer between dielectric and substrate		Abs. Layer on top of dielectric	
Cavity	Dielectric	Dielectric	Dielectric + Abs. Layer	Dielectric	Dielectric + Abs. Layer
From Top: $\lambda = \dots$	$\frac{2nd}{m+\frac{1}{2}}$	$\frac{2nd}{m+\frac{1}{2}-\frac{x}{2\pi}}$	$\frac{2(nd+n_a d_a)}{m-\frac{y}{2\pi}}$	$\frac{2nd}{m+\frac{x}{2\pi}}$	$\frac{2(nd+n_a d_a)}{m+\frac{x}{2\pi}}$
From Bottom: $\lambda = \dots$	$\frac{2nd}{m+\frac{1}{2}}$	$\frac{2nd}{m+\frac{y}{2\pi}}$	$\frac{2(nd+n_a d_a)}{m+\frac{y}{2\pi}}$	$\frac{2nd}{m+\frac{1}{2}-\frac{y'}{2\pi}}$	$\frac{2(nd+n_a d_a)}{m-\frac{x}{2\pi}}$

Table 6.1: Summary of formulas derived to determine the peak locations for different viewing directions, geometries, and approximations.

Doing the full calculation for the infinite series of reflections from all of the surfaces gives a much more complicated expression:

$$\lambda_{\min\{R_{top}\}} = Re\left\{\frac{8\pi dn_1 i}{2im\pi + \log\left(-\frac{(n_0+n_1)(n_0-n_a)}{(n_0-n_1)(n_1+n_a)}\right)}\right\} \quad (6.14)$$

### **6.7.5 Discussion of Approximations**

Ignoring the propagation through the absorbing layer (that is, calculating the peak location via equating the phase accumulation for the reflection at either end of the dielectric material with the phase accumulated by propagating within the dielectric and reflecting from the other side) gives first order approximations that can have as much as 80% error for low-order peaks. This means that, as expected, the multiple reflections within the thin absorbing film are important to the final reflected color of the material, especially for long wavelengths. A better approximation can be calculated by summing up the full infinite series of the accumulated reflections, taking into account the phase accumulated on each round trip in the cavity. However, this calculation results in a complicated complex formula that doesn't provide any intuition into the resulting peak locations and is therefore less useful than a simple transfer matrix model which captures all of the complexities of the reflection spectra.

## **6.8 Additional Experiments**

Several additional experiments were performed to analyze the properties of Janus stacks depending on the location of the absorbing layer within the stack architecture as can be seen in figure 6.10. Here, there is an odd-even effect that is noticeable when comparing the location of the nanoparticle layer within the stack architecture to how noticeable the difference between the first and second side reflection colors are. The gold samples 1 and 3 (where the nanoparticle layer is embedded within the higher index material) show a stronger difference in color between the two sides than the other two samples. As explained above, this effect is due to the increase in the strength of the Janus effect with increases in both the real and imaginary index of the absorbing layer as well as the shift in the absorption profile of the nanoparticles when they are embedded within a higher index material.

Since it is simpler to fabricate samples with the absorbing layer directly on the substrate with a Bragg stack deposited on top of it, we simulate the reflected color of either side of 5-bilayer Bragg stacks on top of a 7 nm absorbing film of varying

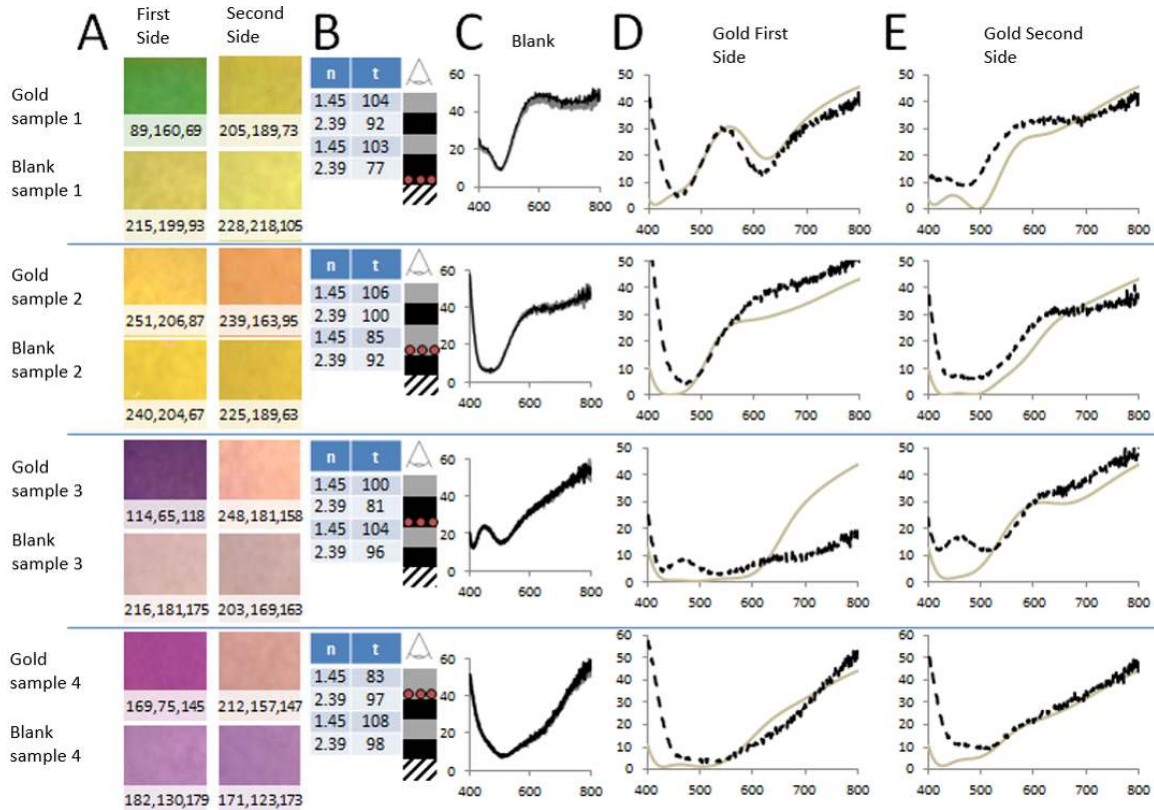


Figure 6.10: A. Optical images of the two different sides of 4-layer Janus stacks with nanoparticles located in between different layers ("Gold") and blank samples ("Blank") with no nanoparticles. Insets are the RGB values for the average color of the image. B. Refractive index values and thicknesses measured by ellipsometry for each layer in the Janus stack (left) and diagram showing the geometry of the film with the substrate (hatched), nanoparticles (red circles), titania (black) and silica (grey). C. Reflection spectra from the front side (black) and back side (grey) of the blank samples showing no discernible difference between the two. D. Reflection spectra (black, dashed) and simulated spectra (grey solid) for the front side of the samples with gold nanoparticles. E. The same as (D) but for the back side.

complex refractive index. The thicknesses of each layer in the Bragg stack were taken to be a quarter of a wavelength in the material for a 500nm peak stack (Fig. 6.11a) and a 650 nm peak stack (Fig. 6.11b).

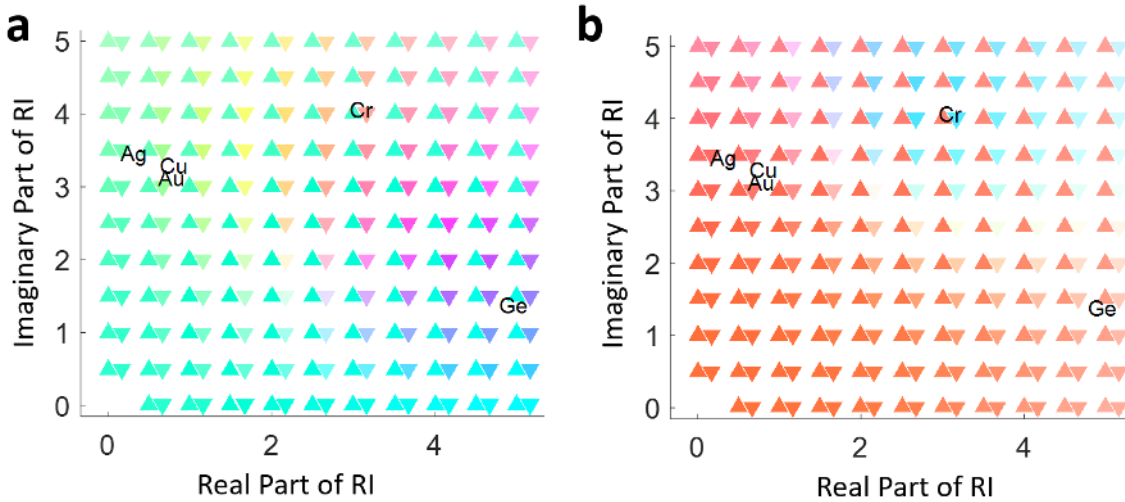


Figure 6.11: a. Results of an array of transfer matrix simulations for a 5-bilayer quarter wave Bragg stack with a 7 nm absorbing layer at the bottom on a glass substrate with a designed peak wavelength of 500 nm for various real and imaginary parts of the refractive index (RI) of the absorbing layer. The triangle pointing up is displayed with the simulated human-eye perceived color as observed from the film side of the sample, while the triangle pointing down is the same for the sample observed from the substrate side. b. Same as (a) but with a designed peak wavelength of 650 nm. The average real and imaginary refractive indices over the visible spectrum of different absorbing materials are inserted into the diagram.

## 6.9 Conclusions

We have designed and demonstrated semi-transparent materials having a different color depending on the viewing direction, by rationally combining absorbing and structural photonic elements. The physical origin of this optical Janus effect lies in the anomalous phase shift of reflected light caused by the complex RI of the absorbing material. In the stack, the dielectric environment of the absorbing material is anisotropic, leading to a different color from constructive interference on both sides of

the sample, which can be predicted by transfer matrix calculations. The optical Janus effect is observed in a wide range of constituent photonic and absorbing elements. These include thin films and multilayer structures as the photonic elements and gold nanoparticles and plain metal films as the absorbing elements. Spatial control of the deposition of the absorbing elements enables the creation of arbitrary asymmetric structural color patterns with controllable, viewing direction dependent coloration as well as more complex anisotropic effects such as viewing direction dependent invisibility of patterns or color travel. This rational design of asymmetric colored materials enables applications in art, architecture and design, and it may also allow for more functional properties, for example in integrated photonic circuits, semitransparent solar cells with independent tunability of absorption profile and transmission color, or security features in anti-counterfeiting materials.

# Bibliography

- [1] Li, L. *et al.* A highly conspicuous mineralized composite photonic architecture in the translucent shell of the blue-rayed limpet. *Nature Communications* **6** (2015).
- [2] Forster, J. D. *et al.* Biomimetic isotropic nanostructures for structural coloration. *Advanced Materials* **22**, 2939–2944 (2010).
- [3] Teyssier, J., Saenko, S. V., Van Der Marel, D. & Milinkovitch, M. C. Photonic crystals cause active colour change in chameleons. *Nature Communications* **6** (2015).
- [4] Galisteo-López, J. F. *et al.* Self-assembled photonic structures. *Advanced Materials* **23**, 30–69 (2011).
- [5] von Freymann, G., Kitaev, V., Lotsch, B. V. & Ozin, G. A. Bottom-up assembly of photonic crystals. *Chemical Society Reviews* **42**, 2528–2554 (2013).
- [6] Josephson, D. P., Miller, M. & Stein, A. Inverse opal  $\text{SiO}_2$  photonic crystals as structurally-colored pigments with additive primary colors. *Zeitschrift für anorganische und allgemeine Chemie* **640**, 655–662 (2014).
- [7] Ito, T., Katsura, C., Sugimoto, H., Nakanishi, E. & Inomata, K. Strain-responsive structural colored elastomers by fixing colloidal crystal assembly. *Langmuir* **29**, 13951–13957 (2013).
- [8] Takeoka, Y. *et al.* Production of colored pigments with amorphous arrays of black and white colloidal particles. *Angewandte Chemie International Edition* **52**, 7261–7265 (2013).
- [9] Zhou, L., Liu, G., Wu, Y., Fan, Q. & Shao, J. The synthesis of core-shell monodisperse p (st-maa) microspheres and fabrication of photonic crystals structure with tunable colors on polyester fabrics. *Fibers and Polymers* **15**, 1112–1122 (2014).

- [10] Lee, J.-S., Lim, C. H., Yang, S.-M. & Kim, S.-H. Monolithic photonic crystals created by partial coalescence of core-shell particles. *Langmuir* **30**, 2369–2375 (2014).
- [11] Aguirre, C. I., Reguera, E. & Stein, A. Colloidal photonic crystal pigments with low angle dependence. *ACS Applied Materials & Interfaces* **2**, 3257–3262 (2010).
- [12] Josephson, D. P., Popczun, E. J. & Stein, A. Effects of integrated carbon as a light absorber on the coloration of photonic crystal-based pigments. *The Journal of Physical Chemistry C* **117**, 13585–13592 (2013).
- [13] Vasquez, Y., Kolle, M., Mishchenko, L., Hatton, B. D. & Aizenberg, J. Three-phase co-assembly: in situ incorporation of nanoparticles into tunable, highly ordered, porous silica films. *ACS Photonics* **1**, 53–60 (2013).
- [14] Koay, N. *et al.* Hierarchical structural control of visual properties in self-assembled photonic-plasmonic pigments. *Optics Express* **22**, 27750–27768 (2014).
- [15] Vogel, N. *et al.* Color from hierarchy: Diverse optical properties of micron-sized spherical colloidal assemblies. *Proceedings of the National Academy of Sciences* **112**, 10845–10850 (2015).
- [16] Kim, J.-J. *et al.* Biologically inspired led lens from cuticular nanostructures of firefly lantern. *Proceedings of the National Academy of Sciences* **109**, 18674–18678 (2012).
- [17] Shawkey, M. D. & Hill, G. E. Significance of a basal melanin layer to production of non-iridescent structural plumage color: evidence from an amelanotic steller’s jay (*cyanocitta stelleri*). *Journal of Experimental Biology* **209**, 1245–1250 (2006).
- [18] Hu, H., Chen, Q.-W., Tang, J., Hu, X.-Y. & Zhou, X.-H. Photonic anti-counterfeiting using structural colors derived from magnetic-responsive photonic crystals with double photonic bandgap heterostructures. *Journal of Materials Chemistry* **22**, 11048–11053 (2012).
- [19] Hu, H. *et al.* Invisible photonic printing: computer designing graphics, uv printing and shown by a magnetic field. *Scientific Reports* **3** (2013).
- [20] Hu, H., Zhong, H., Chen, C. & Chen, Q. Magnetically responsive photonic watermarks on banknotes. *Journal of Materials Chemistry C* **2**, 3695–3702 (2014).



- [21] Yu, Z., Wang, C.-F., Ling, L., Chen, L. & Chen, S. Triphase microfluidic-directed self-assembly: Anisotropic colloidal photonic crystal supraparticles and multicolor patterns made easy. *Angewandte Chemie International Edition* **51**, 2375–2378 (2012).
- [22] Finlayson, C. E. & Baumberg, J. J. Polymer opals as novel photonic materials. *Polymer International* **62**, 1403–1407 (2013).
- [23] Cho, Y. *et al.* Mechanochromic sensors: Elastoplastic inverse opals as power-free mechanochromic sensors for force recording (adv. funct. mater. 38/2015). *Advanced Functional Materials* **25**, 6022–6022 (2015).
- [24] Schäfer, C. G., Lederle, C., Zentel, K., Stühn, B. & Gallei, M. Utilizing stretch-tunable thermochromic elastomeric opal films as novel reversible switchable photonic materials. *Macromolecular Rapid Communications* **35**, 1852–1860 (2014).
- [25] Schäfer, C. G., Smolin, D. A., Hellmann, G. P. & Gallei, M. Fully reversible shape transition of soft spheres in elastomeric polymer opal films. *Langmuir* **29**, 11275–11283 (2013).
- [26] Gallego-Gómez, F., Blanco, A., Golmayo, D. & López, C. Nanostructuring of azomolecules in silica artificial opals for enhanced photoalignment. *Advanced Functional Materials* **21**, 4109–4119 (2011).
- [27] Scheid, D. *et al.* Redox-and mechano-chromic response of metallopolymer-based elastomeric colloidal crystal films. *Journal of Materials Chemistry C* **2**, 2583–2590 (2014).
- [28] Gallego-Gómez, F., Blanco, A. & López, C. Photoinduced local heating in silica photonic crystals for fast and reversible switching. *Advanced Materials* **24**, 6204–6209 (2012).
- [29] Wang, J. *et al.* Multiresponsive hydrogel photonic crystal microparticles with inverse-opal structure. *Langmuir* **29**, 8825–8834 (2013).
- [30] Furumi, S. Active lasing from organic colloidal photonic crystals. *Journal of Materials Chemistry C* **1**, 6003–6012 (2013).
- [31] Magkiriadou, S., Park, J.-G., Kim, Y.-S. & Manoharan, V. N. Disordered packings of core-shell particles with angle-independent structural colors. *Optical Materials Express* **2**, 1343–1352 (2012).
- [32] Yoshioka, S. & Takeoka, Y. Production of colourful pigments consisting of amorphous arrays of silica particles. *ChemPhysChem* **15**, 2209–2215 (2014).

- [33] Prum, R. O., Torres, R., Williamson, S. & Dyck, J. Two-dimensional fourier analysis of the spongy medullary keratin of structurally coloured feather barbs. *Proceedings of the Royal Society of London B: Biological Sciences* **266**, 13–22 (1999).
- [34] Dufresne, E. R. *et al.* Self-assembly of amorphous biophotonic nanostructures by phase separation. *Soft Matter* **5**, 1792–1795 (2009).
- [35] Gotoh, Y. *et al.* An amorphous array of poly (n-isopropylacrylamide) brush-coated silica particles for thermally tunable angle-independent photonic band gap materials. *New Journal of Chemistry* **36**, 2171–2175 (2012).
- [36] Lim, C. H., Kang, H. & Kim, S.-H. Colloidal assembly in leidenfrost drops for noniridescent structural color pigments. *Langmuir* **30**, 8350–8356 (2014).
- [37] Park, J.-G. *et al.* Full-spectrum photonic pigments with non-iridescent structural colors through colloidal assembly. *Angewandte Chemie International Edition* **53**, 2899–2903 (2014).
- [38] Vogel, N. *et al.* Plasmon hybridization in stacked double crescents arrays fabricated by colloidal lithography. *Nano Letters* **11**, 446–454 (2011).
- [39] Zhang, J., Li, Y., Zhang, X. & Yang, B. Colloidal self-assembly meets nanofabrication: From two-dimensional colloidal crystals to nanostructure arrays. *Advanced materials* **22**, 4249–4269 (2010).
- [40] Nemiroski, A. *et al.* Engineering shadows to fabricate optical metasurfaces. *ACS Nano* **8**, 11061–11070 (2014).
- [41] Belardini, A. *et al.* Second harmonic generation circular dichroism from self-ordered hybrid plasmonic–photonic nanosurfaces. *Advanced Optical Materials* **2**, 208–213 (2014).
- [42] Brodoceanu, D. *et al.* Dense arrays of uniform submicron pores in silicon and their applications. *ACS Applied Materials & Interfaces* **7**, 1160–1169 (2015).
- [43] Leem, J. W., Kim, M. S. & Yu, J. S. Broadband highly transparent sapphires with biomimetic antireflective compound submicrometer structures for optical and optoelectronic applications. *JOSA B* **30**, 1665–1670 (2013).
- [44] Vogel, N., Belisle, R. A., Hatton, B., Wong, T.-S. & Aizenberg, J. Transparency and damage tolerance of patternable omniphobic lubricated surfaces based on inverse colloidal monolayers. *Nature Communications* **4** (2013).
- [45] Park, C., Koh, K. & Jeong, U. Structural color painting by rubbing particle powder. *Scientific Reports* **5** (2015).

- [46] Kim, S., Mitropoulos, A. N., Spitzberg, J. D., Kaplan, D. L. & Omenetto, F. G. Silk protein based hybrid photonic-plasmonic crystal. *Optics Express* **21**, 8897–8903 (2013).
- [47] Robbiano, V. *et al.* Hybrid plasmonic–photonic nanostructures: gold nanocrescents over opals. *Advanced Optical Materials* **1**, 389–396 (2013).
- [48] Romanov, S. G., Korovin, A. V., Bahrami, M. R. & Peschel, U. Hybrid architectures: enabling 4-dimensional plasmonic-photonic crystals. In *SPIE Photonics Europe*, 842514–842514 (International Society for Optics and Photonics, 2012).
- [49] Romanov, S. G. *et al.* Probing guided modes in a monolayer colloidal crystal on a flat metal film. *Physical Review B* **86**, 195145 (2012).
- [50] Bravo, J., Zhai, L., Wu, Z., Cohen, R. E. & Rubner, M. F. Transparent superhydrophobic films based on silica nanoparticles. *Langmuir* **23**, 7293–7298 (2007).
- [51] Stelling, C., Bernhardt, C. & Retsch, M. Subwavelength etched colloidal monolayers: A model system for tunable antireflective coatings. *Macromolecular Chemistry and Physics* **216**, 1682–1688 (2015).
- [52] Li, Y. *et al.* Biomimetic surfaces for high-performance optics. *Advanced Materials* **21**, 4731–4734 (2009).
- [53] Guldin, S. & Steiner, U. Soft matter design principles for inorganic photonic nanoarchitectures in photovoltaics, colorimetric sensing, and self-cleaning antireflective coatings. In *SPIE Defense+ Security*, 908320–908320 (International Society for Optics and Photonics, 2014).
- [54] Macleod, H. A. *Thin-film Optical Filters* (CRC press, 2001).
- [55] Budunoglu, H., Yildirim, A. & Bayindir, M. Flexible and mechanically stable antireflective coatings from nanoporous organically modified silica colloids. *Journal of Materials Chemistry* **22**, 9671–9677 (2012).
- [56] Tuvshindorj, U., Yildirim, A., Ozturk, F. E. & Bayindir, M. Robust cassie state of wetting in transparent superhydrophobic coatings. *ACS Applied Materials & Interfaces* **6**, 9680–9688 (2014).
- [57] Zhang, X.-X. *et al.* One-step sol–gel preparation of pdms–silica ormosils as environment-resistant and crack-free thick antireflective coatings. *Journal of Materials Chemistry* **22**, 13132–13140 (2012).

- [58] Hung, W.-B. & Chen, T.-M. Efficiency enhancement of silicon solar cells through a downshifting and antireflective oxysulfide phosphor layer. *Solar Energy Materials and Solar Cells* **133**, 39–47 (2015).
- [59] Wang, Z. *et al.* Formation of a looch and silica composite hierarchical nanostructures thin film by sol-gel dip-coating for superhydrophobic surface with high adhesion force. *Journal of Sol-Gel Science and Technology* **72**, 511–517 (2014).
- [60] Yeo, S. J. *et al.* Angle- and strain-independent coloured free-standing films incorporating non-spherical colloidal photonic crystals. *Soft matter* **11**, 1582–1588 (2015).
- [61] Sowade, E., Hammerschmidt, J., Blaudeck, T. & Baumann, R. R. In-flight inkjet self-assembly of spherical nanoparticle aggregates. *Advanced Engineering Materials* **14**, 98–100 (2012).
- [62] Kuang, M. *et al.* Inkjet printing patterned photonic crystal domes for wide viewing-angle displays by controlling the sliding three phase contact line. *Advanced Optical Materials* **2**, 34–38 (2014).
- [63] Zhao, Y., Shang, L., Cheng, Y. & Gu, Z. Spherical colloidal photonic crystals. *Accounts of Chemical Research* **47**, 3632–3642 (2014).
- [64] Rastogi, V. *et al.* Synthesis of light-diffracting assemblies from microspheres and nanoparticles in droplets on a superhydrophobic surface. *Advanced Materials* **20**, 4263–4268 (2008).
- [65] Schaffner, M., England, G., Kolle, M., Aizenberg, J. & Vogel, N. Combining bottom-up self-assembly with top-down microfabrication to create hierarchical inverse opals with high structural order. *Small* **11**, 4334–4340 (2015).
- [66] Lee, H. S., Shim, T. S., Hwang, H., Yang, S.-M. & Kim, S.-H. Colloidal photonic crystals toward structural color palettes for security materials. *Chemistry of Materials* **25**, 2684–2690 (2013).
- [67] Lee, S. Y., Kim, S.-H., Hwang, H., Sim, J. Y. & Yang, S.-M. Controlled pixelation of inverse opaline structures towards reflection-mode displays. *Advanced Materials* **26**, 2391–2397 (2014).
- [68] Ding, T., Zhao, Q., Smoukov, S. K. & Baumberg, J. J. Selectively patterning polymer opal films via microimprint lithography. *Advanced optical materials* **2**, 1098–1104 (2014).
- [69] Ding, T. *et al.* Modifying the symmetry of colloidal photonic crystals: a way towards complete photonic bandgap. *Journal of Materials Chemistry C* **2**, 4100–4111 (2014).

- [70] Barthlott, W. & Neinhuis, C. Purity of the sacred lotus, or escape from contamination in biological surfaces. *Planta* **202**, 1–8 (1997).
- [71] Aizenberg, J. *et al.* Skeleton of euplectella sp.: structural hierarchy from the nanoscale to the macroscale. *Science* **309**, 275–278 (2005).
- [72] Smith, B. L. *et al.* Molecular mechanistic origin of the toughness of natural adhesives, fibres and composites. *Nature* **399**, 761–763 (1999).
- [73] Srinivasarao, M. Nano-optics in the biological world: beetles, butterflies, birds, and moths. *Chemical Reviews* **99**, 1935–1962 (1999).
- [74] Vukusic, P. & Sambles, J. R. Photonic structures in biology. *Nature* **424**, 852–855 (2003).
- [75] Kinoshita, S., Yoshioka, S. & Miyazaki, J. Physics of structural colors. *Reports on Progress in Physics* **71**, 076401 (2008).
- [76] Kinoshita, S., Yoshioka, S. & Kawagoe, K. Mechanisms of structural colour in the morpho butterfly: cooperation of regularity and irregularity in an iridescent scale. *Proceedings of the Royal Society of London B: Biological Sciences* **269**, 1417–1421 (2002).
- [77] Luke, S. M., Hallam, B. T. & Vukusic, P. Structural optimization for broadband scattering in several ultra-thin white beetle scales. *Applied optics* **49**, 4246–4254 (2010).
- [78] Stavenga, D. G., Leertouwer, H. L., Marshall, N. J. & Osorio, D. Dramatic colour changes in a bird of paradise caused by uniquely structured breast feather barbules. *Proceedings of the Royal Society of London B: Biological Sciences* rspb20102293 (2010).
- [79] Pfaff, G. & Reynders, P. Angle-dependent optical effects deriving from submicron structures of films and pigments. *Chemical Reviews* **99**, 1963–1982 (1999).
- [80] Taylor, R. K. *et al.* Painting by numbers: Nanoparticle-based colorants in the post-empirical age. *Advanced Materials* **23**, 2554–2570 (2011).
- [81] Vogel, N., Weiss, C. K. & Landfester, K. From soft to hard: the generation of functional and complex colloidal monolayers for nanolithography. *Soft Matter* **8**, 4044–4061 (2012).
- [82] Velev, O. D., Lenhoff, A. M. & Kaler, E. W. A class of microstructured particles through colloidal crystallization. *Science* **287**, 2240–2243 (2000).

- [83] Yi, G.-R. *et al.* Monodisperse micrometer-scale spherical assemblies of polymer particles. *Advanced Materials* **14**, 1137–1140 (2002).
- [84] Brugarolas, T., Tu, F. & Lee, D. Directed assembly of particles using microfluidic droplets and bubbles. *Soft Matter* **9**, 9046–9058 (2013).
- [85] Bausch, A. *et al.* Grain boundary scars and spherical crystallography. *Science* **299**, 1716–1718 (2003).
- [86] Meng, G., Paulose, J., Nelson, D. R. & Manoharan, V. N. Elastic instability of a crystal growing on a curved surface. *Science* **343**, 634–637 (2014).
- [87] de Nijs, B. *et al.* Entropy-driven formation of large icosahedral colloidal clusters by spherical confinement. *Nature Materials* **14**, 56–60 (2015).
- [88] Kim, S.-H., Lee, S. Y., Yi, G.-R., Pine, D. J. & Yang, S.-M. Microwave-assisted self-organization of colloidal particles in confining aqueous droplets. *Journal of the American Chemical Society* **128**, 10897–10904 (2006).
- [89] Kim, S.-H., Jeon, S.-J. & Yang, S.-M. Optofluidic encapsulation of crystalline colloidal arrays into spherical membrane. *Journal of the American Chemical Society* **130**, 6040–6046 (2008).
- [90] Kim, S.-H., Park, J.-G., Choi, T. M., Manoharan, V. N. & Weitz, D. A. Osmotic-pressure-controlled concentration of colloidal particles in thin-shelled capsules. *Nature Communications* **5** (2014).
- [91] Xie, Z. *et al.* An optical nose chip based on mesoporous colloidal photonic crystal beads. *Advanced Materials* **26**, 2413–2418 (2014).
- [92] Kim, J. *et al.* Real-time optofluidic synthesis of magnetochromic microspheres for reversible structural color patterning. *Small* **7**, 1163–1168 (2011).
- [93] Zhao, X. *et al.* Colloidal crystal beads as supports for biomolecular screening. *Angewandte Chemie International Edition* **45**, 6835–6838 (2006).
- [94] Liu, W. *et al.* Photonic crystal encoded microcarriers for biomaterial evaluation. *Small* **10**, 88–93 (2014).
- [95] Utada, A. *et al.* Dripping, jetting, drops, and wetting: the magic of microfluidics. *MRS Bulletin* **32**, 702–708 (2007).
- [96] Anna, S. L., Bontoux, N. & Stone, H. A. Formation of dispersions using "flow focusing" in microchannels. *Applied Physics Letters* **82**, 364–366 (2003).
- [97] Phillips, K. R. *et al.* Tunable anisotropy in inverse opals and emerging optical properties. *Chemistry of Materials* **26**, 1622–1628 (2014).

- [98] Pursiainen, O. L. *et al.* Nanoparticle-tuned structural color from polymer opals. *Optics Express* **15**, 9553–9561 (2007).
- [99] Eustis, S. & El-Sayed, M. A. Why gold nanoparticles are more precious than pretty gold: noble metal surface plasmon resonance and its enhancement of the radiative and nonradiative properties of nanocrystals of different shapes. *Chemical Society Reviews* **35**, 209–217 (2006).
- [100] Palmer, C. A. & Loewen, E. G. *Diffraction Grating Handbook* (Newport Corporation Springfield, Ohio, USA, 2005).
- [101] Vogel, N., Goerres, S., Landfester, K. & Weiss, C. K. A convenient method to produce close-and non-close-packed monolayers using direct assembly at the air–water interface and subsequent plasma-induced size reduction. *Macromolecular Chemistry and Physics* **212**, 1719–1734 (2011).
- [102] Vogel, N., de Viguierie, L., Jonas, U., Weiss, C. K. & Landfester, K. Wafer-scale fabrication of ordered binary colloidal monolayers with adjustable stoichiometries. *Advanced Functional Materials* **21**, 3064–3073 (2011).
- [103] Fernández-López, C. *et al.* Highly controlled silica coating of peg-capped metal nanoparticles and preparation of sers-encoded particles. *Langmuir* **25**, 13894–13899 (2009).
- [104] Kubo, S. *et al.* Tunability of the refractive index of gold nanoparticle dispersions. *Nano Letters* **7**, 3418–3423 (2007).
- [105] Li, F., Josephson, D. P. & Stein, A. Colloidal assembly: the road from particles to colloidal molecules and crystals. *Angewandte Chemie International Edition* **50**, 360–388 (2011).
- [106] Kraus, T., Brodoceanu, D., Pazos-Perez, N. & Fery, A. Colloidal surface assemblies: nanotechnology meets bioinspiration. *Advanced Functional Materials* **23**, 4529–4541 (2013).
- [107] Aguirre, C. I., Reguera, E. & Stein, A. Tunable colors in opals and inverse opal photonic crystals. *Advanced Functional Materials* **20**, 2565–2578 (2010).
- [108] Arsenault, A. C. *et al.* From colour fingerprinting to the control of photoluminescence in elastic photonic crystals. *Nature Materials* **5**, 179–184 (2006).
- [109] Arsenault, A. C., Puzzo, D. P., Manners, I. & Ozin, G. A. Photonic-crystal full-colour displays. *Nature Photonics* **1**, 468–472 (2007).

- [110] Diao, Y. Y. & Liu, X. Y. Controlled colloidal assembly: Experimental modeling of general crystallization and biomimicking of structural color. *Advanced Functional Materials* **22**, 1354–1375 (2012).
- [111] Burgess, I. B. *et al.* Wetting in color: colorimetric differentiation of organic liquids with high selectivity. *ACS Nano* **6**, 1427–1437 (2011).
- [112] Phillips, K. R., Vogel, N., Burgess, I. B., Perry, C. C. & Aizenberg, J. Directional wetting in anisotropic inverse opals. *Langmuir* **30**, 7615–7620 (2014).
- [113] Wang, J., Zhang, Y., Wang, S., Song, Y. & Jiang, L. Bioinspired colloidal photonic crystals with controllable wettability. *Accounts of Chemical Research* **44**, 405–415 (2011).
- [114] Chen, J. I., von Freymann, G., Choi, S. Y., Kitaev, V. & Ozin, G. A. Amplified photochemistry with slow photons. *Advanced Materials* **18**, 1915–1919 (2006).
- [115] Liu, J. *et al.* Enhancement of photochemical hydrogen evolution over pt-loaded hierarchical titania photonic crystal. *Energy & Environmental Science* **3**, 1503–1506 (2010).
- [116] Choi, S.-W., Xie, J. & Xia, Y. Chitosan-based inverse opals: Three-dimensional scaffolds with uniform pore structures for cell culture. *Advanced materials* **21**, 2997–3001 (2009).
- [117] Guldin, S. *et al.* Dye-sensitized solar cell based on a three-dimensional photonic crystal. *Nano Letters* **10**, 2303–2309 (2010).
- [118] Tétreault, N. *et al.* High-efficiency dye-sensitized solar cell with three-dimensional photoanode. *Nano Letters* **11**, 4579–4584 (2011).
- [119] Esmanski, A. & Ozin, G. A. Silicon inverse-opal-based macroporous materials as negative electrodes for lithium ion batteries. *Advanced Functional Materials* **19**, 1999–2010 (2009).
- [120] Pikul, J. H., Zhang, H. G., Cho, J., Braun, P. V. & King, W. P. High-power lithium ion microbatteries from interdigitated three-dimensional bicontinuous nanoporous electrodes. *Nature Communications* **4**, 1732 (2013).
- [121] Kim, O.-H. *et al.* Ordered macroporous platinum electrode and enhanced mass transfer in fuel cells using inverse opal structure. *Nature Communications* **4** (2013).
- [122] Fenzl, C., Hirsch, T. & Wolfbeis, O. S. Photonic crystals for chemical sensing and biosensing. *Angewandte Chemie International Edition* **53**, 3318–3335 (2014).



- [123] Tessier, P. M. *et al.* Assembly of gold nanostructured films templated by colloidal crystals and use in surface-enhanced raman spectroscopy. *Journal of the American Chemical Society* **122**, 9554–9555 (2000).
- [124] Kim, S.-H., Lim, J.-M., Jeong, W. C., Choi, D.-G. & Yang, S.-M. Patterned colloidal photonic domes and balls derived from viscous photocurable suspensions. *Advanced Materials* **20**, 3211–3217 (2008).
- [125] Ding, T., Smoukov, S. K. & Baumberg, J. J. Stamping colloidal photonic crystals: a facile way towards complex pixel colour patterns for sensing and displays. *Nanoscale* **7**, 1857–1863 (2015).
- [126] Kim, S.-H., Park, H. S., Choi, J. H., Shim, J. W. & Yang, S.-M. Integration of colloidal photonic crystals toward miniaturized spectrometers. *Advanced Materials* **22**, 946–950 (2010).
- [127] Bhushan, B. *et al.* Encyclopedia of nanotechnology (2012).
- [128] Van Blaaderen, A., Ruel, R., Wiltzius, P. *et al.* Template-directed colloidal crystallization. *Nature* **385**, 321–324 (1997).
- [129] Aizenberg, J., Braun, P. V. & Wiltzius, P. Patterned colloidal deposition controlled by electrostatic and capillary forces. *Physical review Letters* **84**, 2997 (2000).
- [130] Ozin, G. A. & Yang, S. M. The race for the photonic chip: colloidal crystal assembly in silicon wafers. *Advanced Functional Materials* **11**, 95–104 (2001).
- [131] Yang, S., MÃniguez, H. & Ozin, G. Opal circuits of light-Å-planarized microphotonic crystal chips. *Advanced Functional Materials* **12**, 425–431 (2002).
- [132] Fustin, C.-A., Glasser, G., Spiess, H. W. & Jonas, U. Parameters influencing the templated growth of colloidal crystals on chemically patterned surfaces. *Langmuir* **20**, 9114–9123 (2004).
- [133] Ding, T. *et al.* Patterning and pixelation of colloidal photonic crystals for addressable integrated photonics. *Journal of Materials Chemistry* **21**, 11330–11334 (2011).
- [134] Mishchenko, L., Hatton, B., Kolle, M. & Aizenberg, J. Patterning hierarchy in direct and inverse opal crystals. *Small* **8**, 1904–1911 (2012).
- [135] Kumacheva, E., Golding, R. K., Allard, M., Sargent, E. H. *et al.* Colloid crystal growth on mesoscopically patterned surfaces: Effect of confinement. *Advanced Materials* **14**, 221 (2002).

- [136] Jiang, P. & McFarland, M. J. Large-scale fabrication of wafer-size colloidal crystals, macroporous polymers and nanocomposites by spin-coating. *Journal of the American Chemical Society* **126**, 13778–13786 (2004).
- [137] Lee, S.-K., Yi, G.-R., Moon, J. H., Yang, S.-M. & Pine, D. J. Pixellated photonic crystal films by selective photopolymerization. *Advanced Materials* **18**, 2111–2116 (2006).
- [138] Yao, J. *et al.* Patterning colloidal crystals by lift-up soft lithography. *Advanced Materials* **16**, 81–84 (2004).
- [139] Wang, J., Wang, L., Song, Y. & Jiang, L. Patterned photonic crystals fabricated by inkjet printing. *Journal of Materials Chemistry C* **1**, 6048–6058 (2013).
- [140] Hatton, B., Mishchenko, L., Davis, S., Sandhage, K. H. & Aizenberg, J. Assembly of large-area, highly ordered, crack-free inverse opal films. *Proceedings of the National Academy of Sciences* **107**, 10354–10359 (2010).
- [141] Burgess, I. B. *et al.* Encoding complex wettability patterns in chemically functionalized 3d photonic crystals. *Journal of the American Chemical Society* **133**, 12430–12432 (2011).
- [142] Hashimoto, H. & Uyeda, R. Detection of dislocation by the moiré pattern in electron micrographs. *Acta Crystallographica* **10**, 143–143 (1957).
- [143] Yetisen, A. K. *et al.* Nanoart: Art on the nanoscale and beyond. *Advanced Materials* **28**, 1713–1713 (2016).
- [144] Schacher, F. H., Rugar, P. A. & Manners, I. Functional block copolymers: nanostructured materials with emerging applications. *Angewandte Chemie International Edition* **51**, 7898–7921 (2012).
- [145] Vogel, N., Retsch, M., Fustin, C.-A., del Campo, A. & Jonas, U. Advances in colloidal assembly: the design of structure and hierarchy in two and three dimensions. *Chemical Reviews* **115**, 6265–6311 (2015).
- [146] Phillips, K. R. *et al.* A colloidoscope of colloid-based porous materials and their uses. *Chemical Society Reviews* **45**, 281–322 (2016).
- [147] Biro, L. P. & Vigneron, J.-P. Photonic nanoarchitectures in butterflies and beetles: valuable sources for bioinspiration. *Laser & Photonics Reviews* **5**, 27–51 (2011).
- [148] Burresti, M. *et al.* Bright-white beetle scales optimise multiple scattering of light. *Scientific Reports* **4** (2014).

- [149] Magkiriadou, S., Park, J.-G., Kim, Y.-S. & Manoharan, V. N. Absence of red structural color in photonic glasses, bird feathers, and certain beetles. *Physical Review E* **90**, 062302 (2014).
- [150] Vukusic, P., Sambles, J., Lawrence, C. & Wootton, R. Quantified interference and diffraction in single morpho butterfly scales. *Proceedings of the Royal Society of London B: Biological Sciences* **266**, 1403–1411 (1999).
- [151] Wilts, B. D., Giraldo, M. A. & Stavenga, D. G. Unique wing scale photonics of male rajah brooke’s birdwing butterflies. *Frontiers in Zoology* **13**, 36 (2016).
- [152] Chung, K. *et al.* Flexible, angle-independent, structural color reflectors inspired by morpho butterfly wings. *Advanced Materials* **24**, 2375–2379 (2012).
- [153] Umh, H. N., Yu, S., Kim, Y. H., Lee, S. Y. & Yi, J. Tuning the structural color of a 2d photonic crystal using a bowl-like nanostructure. *ACS Applied Materials & Interfaces* (2016).
- [154] England, G. *et al.* Bioinspired micrograting arrays mimicking the reverse color diffraction elements evolved by the butterfly pierella luna. *Proceedings of the National Academy of Sciences* **111**, 15630–15634 (2014).
- [155] Vigneron, J. P. *et al.* Reverse color sequence in the diffraction of white light by the wing of the male butterfly pierella luna (nymphalidae: Satyrinae). *Physical Review E* **82**, 021903 (2010).
- [156] Kolle, M. *et al.* Mimicking the colourful wing scale structure of the papilio blumei butterfly. *Nature Nanotechnology* **5**, 511–515 (2010).
- [157] Ferry, V. E., Munday, J. N. & Atwater, H. A. Design considerations for plasmonic photovoltaics. *Advanced materials* **22**, 4794–4808 (2010).
- [158] Yu, Z., Raman, A. & Fan, S. Fundamental limit of light trapping in grating structures. *Optics Express* **18**, A366–A380 (2010).
- [159] Leung, S.-F. *et al.* Efficient photon capturing with ordered three-dimensional nanowell arrays. *Nano Letters* **12**, 3682–3689 (2012).
- [160] Raman, A., Yu, Z. & Fan, S. Dielectric nanostructures for broadband light trapping in organic solar cells. *Optics Express* **19**, 19015–19026 (2011).
- [161] Chen, J.-Y. *et al.* Enhanced performance of organic thin film solar cells using electrodes with nanoimprinted light-diffraction and light-diffusion structures. *ACS Applied Materials & Interfaces* **6**, 6164–6169 (2014).

- [162] Zhang, R., Shao, B., Dong, J., Zhang, J. & Yang, H. Absorption enhancement analysis of crystalline si thin film solar cells based on broadband antireflection nanocone grating. *Journal of Applied Physics* **110**, 113105 (2011).
- [163] Yao, Y., Liu, H. & Wu, W. Spectrum splitting using multi-layer dielectric metasurfaces for efficient solar energy harvesting. *Applied Physics A* **115**, 713–719 (2014).
- [164] Meng, X. *et al.* Combined front and back diffraction gratings for broad band light trapping in thin film solar cell. *Optics Express* **20**, A560–A571 (2012).
- [165] Hsu, C.-M. *et al.* High-efficiency amorphous silicon solar cell on a periodic nanocone back reflector. *Advanced Energy Materials* **2**, 628–633 (2012).
- [166] Moon, Y.-J. *et al.* Microstructured air cavities as high-index contrast substrates with strong diffraction for light-emitting diodes. *Nano Letters* **16**, 3301–3308 (2016).
- [167] Kim, J.-J. *et al.* Biologically inspired organic light-emitting diodes. *Nano Letters* **16**, 2994–3000 (2016).
- [168] Xiao, M. *et al.* Bio-inspired structural colors produced via self-assembly of synthetic melanin nanoparticles. *ACS Nano* **9**, 5454–5460 (2015).
- [169] Kohri, M., Nannichi, Y., Taniguchi, T. & Kishikawa, K. Biomimetic non-iridescent structural color materials from polydopamine black particles that mimic melanin granules. *Journal of Materials Chemistry C* **3**, 720–724 (2015).
- [170] Zhang, Y. *et al.* Using cuttlefish ink as an additive to produce non-iridescent structural colors of high color visibility. *Advanced Materials* **27**, 4719–4724 (2015).
- [171] Saito, K. & Tatsuma, T. Asymmetric three-way plasmonic color routers. *Advanced Optical Materials* **3**, 883–887 (2015).
- [172] Butun, S. & Aydin, K. Asymmetric light absorption and reflection in freestanding nanostructured metallic membranes. *ACS Photonics* **2**, 1652–1657 (2015).
- [173] Ding, B., Qiu, M. & Blaikie, R. J. Manipulating light absorption in dye-doped dielectric films on reflecting surfaces. *Optics Express* **22**, 25965–25975 (2014).
- [174] Yu, R. *et al.* Structural coloring of glass using dewetted nanoparticles and ultrathin films of metals. *ACS Photonics* (2016).
- [175] Kats, M. A. *et al.* Enhancement of absorption and color contrast in ultra-thin highly absorbing optical coatings. *Applied Physics Letters* **103**, 101104 (2013).

- [176] Kats, M. A., Blanchard, R., Genevet, P. & Capasso, F. Nanometre optical coatings based on strong interference effects in highly absorbing media. *Nature Materials* **12**, 20–24 (2013).
- [177] Kats, M. A. & Capasso, F. Ultra-thin optical interference coatings on rough and flexible substrates. *Applied Physics Letters* **105**, 131108 (2014).
- [178] Kats, M. A., Blanchard, R., Ramanathan, S. & Capasso, F. Thin-film interference in lossy, ultra-thin layers. *Optics and Photonics News* **25**, 40–47 (2014).
- [179] Mirshafieyan, S. S. & Guo, J. Silicon colors: spectral selective perfect light absorption in single layer silicon films on aluminum surface and its thermal tunability. *Optics Express* **22**, 31545–31554 (2014).
- [180] Kats, M. A. *et al.* Ultra-thin perfect absorber employing a tunable phase change material. *Applied Physics Letters* **101**, 221101 (2012).
- [181] Cao, T., Wei, C.-w., Simpson, R. E., Zhang, L. & Cryan, M. J. Broadband polarization-independent perfect absorber using a phase-change metamaterial at visible frequencies. *Scientific Reports* **4**, 3955 (2014).
- [182] Park, J. *et al.* Omnidirectional near-unity absorption in an ultrathin planar semiconductor layer on a metal substrate. *ACS Photonics* **1**, 812–821 (2014).
- [183] Ding, F., Mo, L., Zhu, J. & He, S. Lithography-free, broadband, omnidirectional, and polarization-insensitive thin optical absorber. *Applied Physics Letters* **106**, 061108 (2015).
- [184] Lee, K.-T., Lee, J. Y., Seo, S. & Guo, L. J. Colored ultrathin hybrid photovoltaics with high quantum efficiency. *Light: Science & Applications* **3**, e215 (2014).
- [185] Lee, K.-T., Fukuda, M., Joglekar, S. & Guo, L. J. Colored, see-through perovskite solar cells employing an optical cavity. *Journal of Materials Chemistry C* **3**, 5377–5382 (2015).
- [186] Diest, K., Dionne, J. A., Spain, M. & Atwater, H. A. Tunable color filters based on metal- insulator- metal resonators. *Nano Letters* **9**, 2579–2583 (2009).
- [187] Xu, T., Wu, Y.-K., Luo, X. & Guo, L. J. Plasmonic nanoresonators for high-resolution colour filtering and spectral imaging. *Nature Communications* **1**, 59 (2010).
- [188] Li, Z., Butun, S. & Aydin, K. Large-area, lithography-free super absorbers and color filters at visible frequencies using ultrathin metallic films. *ACS Photonics* **2**, 183–188 (2015).

- [189] Park, C.-S., Shrestha, V. R., Lee, S.-S. & Choi, D.-Y. Trans-reflective color filters based on a phase compensated etalon enabling adjustable color saturation. *Scientific Reports* **6** (2016).
- [190] Kwon, H. & Kim, S. Chemically tunable, biocompatible, and cost-effective metal–insulator–metal resonators using silk protein and ultrathin silver films. *ACS Photonics* **2**, 1675–1680 (2015).
- [191] Yang, Z. *et al.* Reflective color filters and monolithic color printing based on asymmetric fabry–perot cavities using nickel as a broadband absorber. *Advanced Optical Materials* (2016).
- [192] Poddubny, A., Iorsh, I., Belov, P. & Kivshar, Y. Hyperbolic metamaterials. *Nature Photonics* **7**, 948–957 (2013).
- [193] Sreekanth, K. V. *et al.* Extreme sensitivity biosensing platform based on hyperbolic metamaterials. *Nature Materials* (2016).
- [194] Li, Z., Clark, A. W. & Cooper, J. M. Dual color plasmonic pixels create a polarization controlled nano color palette. *ACS Nano* **10**, 492–498 (2016).
- [195] Duempelmann, L., Casari, D., Luu-Dinh, A., Gallinet, B. & Novotny, L. Color rendering plasmonic aluminum substrates with angular symmetry breaking. *ACS Nano* **9**, 12383–12391 (2015).
- [196] Duempelmann, L., Luu-Dinh, A., Gallinet, B. & Novotny, L. Four-fold color filter based on plasmonic phase retarder. *ACS Photonics* **3**, 190–196 (2015).
- [197] Shrestha, V. R., Lee, S.-S., Kim, E.-S. & Choi, D.-Y. Polarization-tuned dynamic color filters incorporating a dielectric-loaded aluminum nanowire array. *Scientific Reports* **5** (2015).
- [198] Honma, H., Takahashi, K., Fukuhara, M., Ishida, M. & Sawada, K. Free-standing aluminium nanowire arrays for high-transmission plasmonic colour filters. *IET Micro & Nano Letters* **9**, 891–895 (2014).
- [199] Zheng, J., Ye, Z.-C. & Sheng, Z.-M. Reflective low-sideband plasmonic structural colors. *Optical Materials Express* **6**, 381–387 (2016).
- [200] Sun, N. *et al.* Tunable spectral filters based on metallic nanowire gratings. *Optical Materials Express* **5**, 912–919 (2015).
- [201] Nawrot, M., Zinkiewicz, Ł., Włodarczyk, B. & Wasylczyk, P. Transmission phase gratings fabricated with direct laser writing as color filters in the visible. *Optics Express* **21**, 31919–31924 (2013).

- [202] Khorasaninejad, M., Abedzadeh, N., Walia, J., Patchett, S. & Saini, S. Color matrix refractive index sensors using coupled vertical silicon nanowire arrays. *Nano Letters* **12**, 4228–4234 (2012).
- [203] Seo, K. *et al.* Multicolored vertical silicon nanowires. *Nano Letters* **11**, 1851–1856 (2011).
- [204] Park, H. & Crozier, K. B. Vertically stacked photodetector devices containing silicon nanowires with engineered absorption spectra. *ACS Photonics* **2**, 544–549 (2015).
- [205] Soukoulis, C. M. & Wegener, M. Past achievements and future challenges in the development of three-dimensional photonic metamaterials. *Nature Photonics* **5**, 523–530 (2011).
- [206] Minovich, A. E. *et al.* Functional and nonlinear optical metasurfaces. *Laser & Photonics Reviews* **9**, 195–213 (2015).
- [207] Gu, Y., Zhang, L., Yang, J. K., Yeo, S. P. & Qiu, C.-W. Color generation via subwavelength plasmonic nanostructures. *Nanoscale* **7**, 6409–6419 (2015).
- [208] Shaltout, A. M., Kildishev, A. V. & Shalaev, V. M. Evolution of photonic metasurfaces: from static to dynamic. *JOSA B* **33**, 501–510 (2016).
- [209] Kumar, K. *et al.* Printing colour at the optical diffraction limit. *Nature Nanotechnology* **7**, 557–561 (2012).
- [210] Xue, J. *et al.* Scalable, full-colour and controllable chromotropic plasmonic printing. *Nature Communications* **6** (2015).
- [211] Wu, Y.-K. R., Hollowell, A. E., Zhang, C. & Guo, L. J. Angle-insensitive structural colours based on metallic nanocavities and coloured pixels beyond the diffraction limit. *Scientific Reports* **3**, 1194 (2013).
- [212] Cheng, F., Gao, J., Luk, T. S. & Yang, X. Structural color printing based on plasmonic metasurfaces of perfect light absorption. *Scientific Reports* **5** (2015).
- [213] Roberts, A. S., Pors, A., Albrektsen, O. & Bozhevolnyi, S. I. Subwavelength plasmonic color printing protected for ambient use. *Nano Letters* **14**, 783–787 (2014).
- [214] Tan, S. J. *et al.* Plasmonic color palettes for photorealistic printing with aluminum nanostructures. *Nano Letters* **14**, 4023–4029 (2014).
- [215] Clausen, J. S. *et al.* Plasmonic metasurfaces for coloration of plastic consumer products. *Nano Letters* **14**, 4499–4504 (2014).

- [216] Yue, W., Gao, S., Lee, S.-S., Kim, E.-S. & Choi, D.-Y. Subtractive color filters based on a silicon-aluminum hybrid-nanodisk metasurface enabling enhanced color purity. *Scientific Reports* **6** (2016).
- [217] Miyata, M., Hatada, H. & Takahara, J. Full-color subwavelength printing with gap-plasmonic optical antennas. *Nano Letters* **16**, 3166–3172 (2016).
- [218] Cheng, F. *et al.* Aluminum plasmonic metamaterials for structural color printing. *Optics Express* **23**, 14552–14560 (2015).
- [219] Ye, X. & Qi, L. Two-dimensionally patterned nanostructures based on monolayer colloidal crystals: controllable fabrication, assembly, and applications. *Nano Today* **6**, 608–631 (2011).
- [220] Wang, L. *et al.* Large area plasmonic color palettes with expanded gamut using colloidal self-assembly. *ACS Photonics* **3**, 627–633 (2016).
- [221] Ohno, T. *et al.* Hole-size tuning and sensing performance of hexagonal plasmonic nanohole arrays. *Optical Materials Express* **6**, 1594–1603 (2016).
- [222] Bradley, L. & Zhao, Y. Uniform plasmonic response of colloidal ag patchy particles prepared by swinging oblique angle deposition. *Langmuir* (2016).
- [223] Honold, T., Volk, K., Rauh, A., Fitzgerald, J. & Karg, M. Tunable plasmonic surfaces via colloid assembly. *Journal of Materials Chemistry C* **3**, 11449–11457 (2015).
- [224] Mendes, M. J., Morawiec, S., Simone, F., Priolo, F. & Crupi, I. Colloidal plasmonic back reflectors for light trapping in solar cells. *Nanoscale* **6**, 4796–4805 (2014).
- [225] Chen, T. & Reinhard, B. M. Assembling color on the nanoscale: Multichromatic switchable pixels from plasmonic atoms and molecules. *Advanced Materials* **28**, 3522–3527 (2016).
- [226] Zhang, C. *et al.* Printed photonic elements: nanoimprinting and beyond. *Journal of Materials Chemistry C* **4**, 5133–5153 (2016).
- [227] Franklin, D. *et al.* Polarization-independent actively tunable colour generation on imprinted plasmonic surfaces. *Nature Communications* **6** (2015).
- [228] Olson, J. *et al.* High chromaticity aluminum plasmonic pixels for active liquid crystal displays. *ACS Nano* **10**, 1108–1117 (2015).
- [229] Parker, A. R., Welch, V. L., Driver, D. & Martini, N. Structural colour: opal analogue discovered in a weevil. *Nature* **426**, 786–787 (2003).



- [230] Galusha, J. W., Richey, L. R., Gardner, J. S., Cha, J. N. & Bartl, M. H. Discovery of a diamond-based photonic crystal structure in beetle scales. *Physical Review E* **77**, 050904 (2008).
- [231] Saranathan, V. *et al.* Structure, function, and self-assembly of single network gyroid (i4132) photonic crystals in butterfly wing scales. *Proceedings of the National Academy of Sciences* **107**, 11676–11681 (2010).
- [232] Simonis, P. & Vigneron, J. P. Structural color produced by a three-dimensional photonic polycrystal in the scales of a longhorn beetle: *Pseudomyagrus waterhousei* (coleoptera: Cerambycidae). *Physical Review E* **83**, 011908 (2011).
- [233] Parker, A. R., McPhedran, R. C., McKenzie, D. R., Botten, L. C. & Nicorovici, N. Photonic engineering. aphrodite’s iridescence. *Nature* **409**, 36–37 (2001).
- [234] Trzeciak, T. M. & Vukusic, P. Photonic crystal fiber in the polychaete worm *pherusa* sp. *Physical Review E* **80**, 061908 (2009).
- [235] Prum, R. O. & Torres, R. Structural colouration of avian skin: convergent evolution of coherently scattering dermal collagen arrays. *Journal of Experimental Biology* **206**, 2409–2429 (2003).
- [236] Welch, V., Vigneron, J. P., Lousse, V. & Parker, A. Optical properties of the iridescent organ of the comb-jellyfish *beroë cucumis* (ctenophora). *Physical Review E* **73**, 041916 (2006).
- [237] Seago, A. E., Brady, P., Vigneron, J.-P. & Schultz, T. D. Gold bugs and beyond: a review of iridescence and structural colour mechanisms in beetles (coleoptera). *Journal of the Royal Society Interface* **6**, S165–S184 (2009).
- [238] Whitney, H. M. *et al.* Floral iridescence, produced by diffractive optics, acts as a cue for animal pollinators. *Science* **323**, 130–133 (2009).
- [239] CIE. Commission internationale de leclairage proceedings (1931).
- [240] Xia, Y. & Whitesides, G. M. Soft lithography. *Annual Review of Materials Science* **28**, 153–184 (1998).
- [241] Laermer, F. & Schilp, A. Plasma polymerizing temporary etch stop. *US Pat* **5501893** (1996).
- [242] Ayon, A., Braff, R., Bayt, R., Sawin, H. & Schmidt, M. Influence of coil power on the etching characteristics in a high density plasma etcher. *Journal of the Electrochemical Society* **146**, 2730–2736 (1999).

- [243] Maluf, N. & Williams, K. *Introduction to Microelectromechanical Systems Engineering* (Artech House, 2004).
- [244] Oskooi, A. F. *et al.* Meep: A flexible free-software package for electromagnetic simulations by the fdtd method. *Computer Physics Communications* **181**, 687–702 (2010).
- [245] Bassil, M., Davenas, J. & Tahchi, M. E. Electrochemical properties and actuation mechanisms of polyacrylamide hydrogel for artificial muscle application. *Sensors and Actuators B: Chemical* **134**, 496–501 (2008).
- [246] Kim, P., Zarzar, L. D., Zhao, X., Sidorenko, A. & Aizenberg, J. Microbristle in gels: Toward all-polymer reconfigurable hybrid surfaces. *Soft Matter* **6**, 750–755 (2010).
- [247] Kim, P., Zarzar, L. D., He, X., Grinthal, A. & Aizenberg, J. Hydrogel-actuated integrated responsive systems (hairs): Moving towards adaptive materials. *Current Opinion in Solid State and Materials Science* **15**, 236–245 (2011).
- [248] Volder, M. D., Johná Hart, A. *et al.* Hydrogel-driven carbon nanotube microtransducers. *Soft Matter* **7**, 9844–9847 (2011).
- [249] Sniadecki, N. J. *et al.* Magnetic microposts as an approach to apply forces to living cells. *Proceedings of the National Academy of Sciences* **104**, 14553–14558 (2007).
- [250] Aschwanden, M. & Stemmer, A. Polymeric, electrically tunable diffraction grating based on artificial muscles. *Optics Letters* **31**, 2610–2612 (2006).
- [251] Schueller, O. J., Duffy, D. C., Rogers, J. A., Brittain, S. T. & Whitesides, G. M. Reconfigurable diffraction gratings based on elastomeric microfluidic devices. *Sensors and Actuators A: Physical* **78**, 149–159 (1999).
- [252] Xia, Y., Kim, E., Zhao, X.-M., Rogers, J. A. *et al.* Complex optical surfaces formed by replica molding against elastomeric masters. *Science* **273**, 347 (1996).
- [253] Butler, M. *et al.* A mems-based programmable diffraction grating for optical holography in the spectral domain. In *Semiconductor Device Research Symposium, 2001 International*, 422 (IEEE, 2001).
- [254] Potyrailo, R. A. *et al.* Morpho butterfly wing scales demonstrate highly selective vapour response. *Nature Photonics* **1**, 123–128 (2007).
- [255] Garrett, N. L. *et al.* Spectroscopy on the wing: Naturally inspired sers substrates for biochemical analysis. *Journal of Biophotonics* **2**, 157 (2009).

- [256] Pris, A. D. *et al.* Towards high-speed imaging of infrared photons with bio-inspired nanoarchitectures. *Nature Photonics* **6**, 195–200 (2012).
- [257] Zang, X., Tan, Y., Lv, Z., Gu, J. & Zhang, D. Moth wing scales as optical ph sensors. *Sensors and Actuators B: Chemical* **166**, 824–828 (2012).
- [258] Potyrailo, R. A. *et al.* Discovery of the surface polarity gradient on iridescent morpho butterfly scales reveals a mechanism of their selective vapor response. *Proceedings of the National Academy of Sciences* **110**, 15567–15572 (2013).
- [259] Kim, S. *et al.* Silk inverse opals. *Nature Photonics* **6**, 818–823 (2012).
- [260] Lawrence, C., Geddes, N., Furlong, D. & Sambles, J. Surface plasmon resonance studies of immunoreactions utilizing disposable diffraction gratings. *Biosensors and Bioelectronics* **11**, 389–400 (1996).
- [261] Dostálek, J., Homola, J. & Miler, M. Rich information format surface plasmon resonance biosensor based on array of diffraction gratings. *Sensors and Actuators B: Chemical* **107**, 154–161 (2005).
- [262] Wark, A. W., Lee, H. J., Qavi, A. J. & Corn, R. M. Nanoparticle-enhanced diffraction gratings for ultrasensitive surface plasmon biosensing. *Analytical Chemistry* **79**, 6697–6701 (2007).
- [263] Heine, C. & Morf, R. H. Submicrometer gratings for solar energy applications. *Applied Optics* **34**, 2476–2482 (1995).
- [264] Feng, N.-N. *et al.* Design of highly efficient light-trapping structures for thin-film crystalline silicon solar cells. *IEEE Transactions on Electron Devices* **54**, 1926–1933 (2007).
- [265] Munday, J. N. & Atwater, H. A. Large integrated absorption enhancement in plasmonic solar cells by combining metallic gratings and antireflection coatings. *Nano Letters* **11**, 2195–2201 (2010).
- [266] Fujita, M. *et al.* Optical and electrical characteristics of organic light-emitting diodes with two-dimensional photonic crystals in organic/electrode layers. *Japanese Journal of Applied Physics* **44**, 3669 (2005).
- [267] Wierer, J. J., David, A. & Megens, M. M. Iii-nitride photonic-crystal light-emitting diodes with high extraction efficiency. *Nature Photonics* **3**, 163–169 (2009).
- [268] Arpin, K. A. *et al.* Multidimensional architectures for functional optical devices. *Advanced Materials* **22**, 1084–1101 (2010).

- [269] van Renesse, R. L. Paper based document security—a review. In *Security and Detection, 1997. ECOS 97., European Conference on*, 75–80 (IET, 1997).
- [270] Staub, R. & Tompkin, W. R. Nonstandard diffraction structures for ovd's. In *Photonics West '98 Electronic Imaging*, 194–202 (International Society for Optics and Photonics, 1998).
- [271] Lee, R. Micro-technology for anti-counterfeiting. *Microelectronic Engineering* **53**, 513–516 (2000).
- [272] Yee, K. S. *et al.* Numerical solution of initial boundary value problems involving maxwell's equations in isotropic media. *IEEE Trans. Antennas Propag* **14**, 302–307 (1966).
- [273] Lumerical solutions, inc. <http://www.lumerical.com/tcad-products/fdtd/>. Accessed: 2014-09-25.
- [274] Berenger, J.-P. A perfectly matched layer for the absorption of electromagnetic waves. *Journal of Computational Physics* **114**, 185–200 (1994).
- [275] Gartia, M. R. *et al.* Colorimetric plasmon resonance imaging using nano lycurgus cup arrays. *Advanced Optical Materials* **1**, 68–76 (2013).
- [276] Duncan, K. A. *et al.* Art as an avenue to science literacy: Teaching nanotechnology through stained glass. *Journal of Chemical Education* **87**, 1031–1038 (2010).
- [277] Maile, F. J., Pfaff, G. & Reynders, P. Effect pigments—past, present and future. *Progress in organic coatings* **54**, 150–163 (2005).
- [278] Ferrara, M. & Bengisu, M. *Materials that change color: smart materials, intelligent design* (Springer, 2014).
- [279] Zhu, L., Kapraun, J., Ferrara, J. & Chang-Hasnain, C. J. Flexible photonic metastructures for tunable coloration. *Optica* **2**, 255–258 (2015).
- [280] Granqvist, C. G. Electrochromics for smart windows: Oxide-based thin films and devices. *Thin Solid Films* **564**, 1–38 (2014).
- [281] Shi, N. N. *et al.* Keeping cool: Enhanced optical reflection and radiative heat dissipation in saharan silver ants. *Science* **349**, 298–301 (2015).
- [282] Hossain, M. M., Jia, B. & Gu, M. A metamaterial emitter for highly efficient radiative cooling. *Advanced Optical Materials* **3**, 1047–1051 (2015).
- [283] Myroshnychenko, V. *et al.* Modelling the optical response of gold nanoparticles. *Chemical Society Reviews* **37**, 1792–1805 (2008).

- [284] Wu, L. *et al.* Optical functional materials inspired by biology. *Advanced Optical Materials* **4**, 195–224 (2016).
- [285] Starkey, T. & Vukusic, P. Light manipulation principles in biological photonic systems. *Nanophotonics* **2**, 289–307 (2013).
- [286] Lin, D., Fan, P., Hasman, E. & Brongersma, M. L. Dielectric gradient metasurface optical elements. *Science* **345**, 298–302 (2014).
- [287] Galisteo-López, J. F., Gil, L. K., Ibisate, M. & López, C. Organic opals: Properties and applications. In *Organic and Hybrid Photonic Crystals*, 31–55 (Springer, 2015).
- [288] Shen, H., Wang, Z., Wu, Y. & Yang, B. One-dimensional photonic crystals: fabrication, responsiveness and emerging applications in 3d construction. *RSC Adv.* **6**, 4505–4520 (2016).
- [289] Tzeng, P., Hewson, D., Vukusic, P., Eichhorn, S. J. & Grunlan, J. Bio-inspired iridescent layer-by-layer assembled cellulose nanocrystal bragg stacks. *Journal of Materials Chemistry C* **3**, 4260–4264 (2015).
- [290] Luo, J., Li, S., Hou, B. & Lai, Y. Loss/gain-induced ultrathin antireflection coatings. *Scientific Reports* **6** (2016).
- [291] Walther, A. & Müller, A. H. Janus particles: synthesis, self-assembly, physical properties, and applications. *Chemical Reviews* **113**, 5194–5261 (2013).
- [292] Yariv, A. & Yeh, P. *Photonics: Optical Electronics in Modern Communications* (Oxford University Press, Inc., 2006).
- [293] Karakouz, T., Tesler, A. B., Bendikov, T. A., Vaskevich, A. & Rubinstein, I. Highly stable localized plasmon transducers obtained by thermal embedding of gold island films on glass. *Advanced Materials* **20**, 3893–3899 (2008).